Ψ_k Scientific Highlight Of The Month

No. 159 **February 2025**

The Wannier Function Software Ecosystem for Materials Simulations

Antimo Marrazzo[1,2*], Sophie Beck[3], Elena R. Margine[4], Nicola Marzari[5,6], Arash A. Mostofi[7], Junfeng Qiao[5], Ivo Souza[8,9], Stepan S. Tsirkin[8,9], Jonathan R. Yates[10], Giovanni Pizzi[6†]

[1] *Scuola Internazionale Superiore di Studi Avanzati (SISSA), I-34136 Trieste, Italy*

[2] *Dipartimento di Fisica, Università di Trieste, I-34151 Trieste, Italy*

[3] *Center for Computational Quantum Physics, Flatiron Institute, 162 5th Avenue, New York, New York 10010, USA*

[4] *Department of Physics, Applied Physics, and Astronomy, Binghamton University-SUNY, Binghamton, New York 13902, USA*

[5] *Theory and Simulation of Materials (THEOS), and National Centre for Computational Design and Discovery of Novel Materials (MARVEL), École Polytechnique Fédérale de Lausanne, CH-1015 Lausanne, Switzerland*

[6] *Laboratory for Materials Simulations (LMS), and National Centre for Computational Design and Discovery of Novel Materials (MARVEL), Paul Scherrer Institut (PSI), CH-5232 Villigen PSI, Switzerland*

[7] *Departments of Materials and Physics, and the Thomas Young Centre for Theory and Simulation of Materials, Imperial College London, London SW7 2AZ, UK*

[8] *Centro de Física de Materiales, Universidad del País Vasco, 20018 San Sebastián, Spain*

[9] *Ikerbasque Foundation, 48013 Bilbao, Spain*

[10] *Department of Materials, University of Oxford, Parks Road, Oxford OX1 3PH, UK*

This Ψ_k Scientific Highlight is a reformatted preprint version based on the arXiv submission Ref. [1]. A revised and peer-reviewed version of this review may be found in Reviews of Modern Physics 96, 045008 (2024) [https://doi.org/10.1103/RevModPhys.96.045008] [2].

Abstract

Over the last two decades, following the early developments on maximally localized Wannier functions, an ecosystem of electronic-structure simulation techniques and software packages leveraging the Wannier representation has flourished. This environment includes codes to obtain Wannier functions and interfaces with first-principles simulation software, as well as an increasing number of related post-processing packages. Wannier functions can be obtained for isolated or extended systems (both crystalline and disordered), and can be used to

*amarrazz@sissa.it

†giovanni.pizzi@psi.ch

understand chemical bonding, to characterize electric polarization, magnetization, and topology, or as an optimal basis set, providing very accurate interpolations in reciprocal space or large-scale Hamiltonians in real space. In this review, we summarize the current landscape of techniques, materials properties and simulation codes based on Wannier functions that have been made accessible to the research community, and that are now well integrated into what we term a *Wannier function software ecosystem*. First, we introduce the theory and practicalities of Wannier functions, starting from their broad domains of applicability to advanced minimization methods using alternative approaches beyond maximal localization. Then we define the concept of a Wannier ecosystem and its interactions and interoperability with many quantum simulations engines and post-processing packages. We focus on some of the key properties and capabilities that are empowered by such ecosystem—from band interpolations and large-scale simulations to electronic transport, Berryology, topology, electron-phonon couplings, dynamical mean-field theory, embedding, and Koopmans functionals—concluding with the current status of interoperability and automation. The review aims at highlighting basic theory and concepts behind codes, providing relevant pointers to more in-depth references. It also elucidates the relationships and connections between codes and, where relevant, the different motivations and objectives behind their development strategies. Finally, we provide an outlook on future developments, and comment on the goals of biodiversity and sustainability for the whole software ecosystem.

1 Introduction

Wannier functions (WFs) [3], and in particular maximally localized Wannier functions (MLWFs) [4], provide an accurate, compact, and localized representation of the electronic-structure problem, and have become widely used in computational condensed-matter physics and materials science [5].

Thanks to developments in theory, algorithms and implementations over the past few decades, summarized in Sec. 2, it has now become possible to apply widely the concept of MLWFs to single-particle theories and in particular to Kohn–Sham (KS) density-functional theory (DFT) simulations, to obtain localized orbitals from Bloch states; the latter can be themselves represented with localized or extended basis sets, such as plane waves. On one hand, these developments have benefited from profound connections between WFs and physical quantities such as electric polarization, orbital magnetization and topological invariants [6–10]. On the other hand, the ability to obtain MLWFs from DFT simulations can enable the calculation of physical quantities with high accuracy, but at a fraction of the computational cost, thanks to their role as very accurate interpolators [11–13]. Finally, although not discussed here, localized representations have long been pioneered by the quantum chemistry community to interpret coordination and bonding [14], and MLWFs extend to periodic systems the concept of Foster-Boys localized orbitals [15], thanks to algorithmic breakthroughs in calculating the position operator in solids [16–20].

Wannier functions are typically localized or even exponentially localized [21–23], and due to the nearsightedness of interacting electrons [24–26], local electronic properties only depend on the nearby environment [27–30]. As a consequence, the resulting Hamiltonian matrix expressed in a localized basis set (such as MLWFs [12, 31]) becomes sparse, i.e., it displays negligible

matrix elements—or hoppings, in the language of a tight-binding (TB) formalism—if the distance between the corresponding localized basis functions exceeds a given threshold. In this sense, MLWFs constitute an optimal choice as they decay exponentially in real space [23] and they minimize a localization functional by design [4, 5]. The resulting MLWFs can be used as a basis set to build, LEGO™-like, the electronic structure of large-scale nanostructures [12] (that, thanks to the sparsity of the resulting Hamiltonian matrix, could be solved with linear-scaling methods [32–34]), or as a remarkably accurate interpolators of electronic properties, operators and quantities defined as integrals over the Brillouin zone (BZ) of periodic systems [11, 13]. Interpolation on dense grids becomes essential when very fine features need to be resolved, as happens when integrals are restricted to lower-dimensional manifolds (such as the Fermi surface, in the case of transport properties of metals).

Nowadays, MLWFs are routinely used in many research areas of condensed-matter physics and materials science. In Sec. 2 we summarize the past and current challenges, discussing how we reached the current state. The flourishing of this field is not only due to theoretical advances, but also strongly driven by the concerted development of accessible and efficient software. Indeed, thanks to the availability of robust software packages (often open-source, encouraging further contributions), and to the user support provided by developers, researchers can now not only easily compute MLWFs, but also use them as core ingredients for advanced simulations. As more codes appear, they adopt the *de facto* standardization of input and output formats, resulting in a set of interacting and interoperating codes that we will call here the "Wannier function software ecosystem."

This review does not aim to provide an extensive discussion of the theory of MLWFs, for which we refer to [5], although we do provide a general introduction to the field in Sec. 1.1. Instead, the goal is to discuss the nature of the ecosystem and the capabilities of existing codes, focusing in Sec. 3 on a selection of physical phenomena or quantities that can be efficiently predicted thanks to WFs, and on how WFs are used as an ingredient to extend the accuracy of beyond-DFT simulations. Nevertheless, we will still mention a few notable developments of the past decade, whenever useful to contextualize the theoretical and software developments. Our aim is to provide a reference that can help newcomers and existing practitioners alike navigate the ecosystem: which properties can be computed by which codes, when and why the use of WFs is beneficial, which quantities are exchanged between codes, and how interoperability is being addressed.

To facilitate the discussion of the codes, in this review we group them into three major categories: *Wannier engines*, i.e., codes to obtain WFs; *interface codes* between the first-principles engines (e.g., DFT or GW codes) and the Wannier engines; and *Wannier-enabled codes*, which range from relatively simple post-processing tools to more advanced codes that use WFs as one of the ingredients to accelerate accurate simulations. A fourth category of codes that we discuss in Sec. 3.10 are *automation workflows*. Indeed, until very recently the generation of WFs typically required human intuition by experienced researchers to provide initial trial orbitals. This barrier has been largely removed by recent algorithmic and automation efforts (see Sec. 2.4), enabling the use of WFs both by new users and for high-throughput materials discovery and characterization. In the latter case, managing thousands (or more) simulations poses new challenges, which require not only the use of robust workflow engines, but also the implementation

of WF-specific workflows to effectively interconnect multiple codes within the ecosystem.

We will conclude in Sec. 4 with some perspectives on the field related to the sustainability of the whole effort, current challenges that still need to be addressed, and possible future developments.

1.1 *Ab initio* electronic structure and Wannier functions

Electronic-structure simulations aim to determine the behavior of electrons in materials and molecules, as governed by the Schrödinger or Dirac equations. Electrons feel Coulomb interactions among themselves and with the nuclei, in addition to couplings with external fields (e.g., electrical, magnetic, or electromagnetic/photons) or perturbations (e.g., strain, phonons). The core electrons of heavy chemical elements can reach relativistic speeds, requiring the Schrödinger equation to be corrected with terms obtained from an expansion of the Dirac equation in powers of $1/c^2$, where c is the speed of light. The most relevant relativistic correction is spin-orbit coupling, which is responsible for several important phenomena related to magnetism and to geometrical and topological properties of the electronic manifold (see Sec. 3.5 and Sec. 3.6).

An exact solution of the Schrödinger equation (either the bare one, or with relativistic corrections) would give access to essentially all property of materials. This problem was already clear in 1929, when Paul Dirac declared: "The underlying physical laws necessary for the mathematical theory of a large part of physics and the whole of chemistry are thus completely known, and the difficulty is only that the exact application of these laws leads to equations much too complicated to be soluble" [35].

For more than fifty years, *ab initio* or first-principles methods have been developed to approximately solve the Schrödinger equation in realistic settings [36, 37], with more accurate strategies and theories being developed. In parallel, the exponential growth of computational power (Moore's law) has allowed to deploy these new theoretical instruments through numerical simulations, constantly seeking not only to improve accuracy but also targeting more complex and realistic systems. Quickly, numerical solutions became sufficiently accurate to be predictive for a number of properties in relevant systems: the era of first-principles materials modeling had begun [38, 39].

An iconic example is given by DFT, which made it possible to determine the electronic structure of complex materials with reasonable accuracy at low cost. In DFT, the total energy of the electrons is expressed as a functional of the electronic charge density [36, 37]. The theory is supported by two pillars, the Hohenberg–Kohn theorems, which state not only a one-to-one correspondence between the ground-state many-body wavefunction and the ground-state charge density, but also formulate a variational total-energy functional: the solution of the Schrödinger equation can be recast as a minimization problem for the charge density, a remarkably simpler object (a real function of $\mathbf{r}$) than the many-body wavefunction we started from (a complex function of $3N_e$ variables, where N_e is the number of electrons in the system).

In KS DFT, the interacting many-body problem is mapped onto a non-interacting problem sharing the same ground-state charge density but in presence of a suitable local external potential; the latter is in general unknown. This *ansatz* enables the kinetic energy contribution to be calculated accurately through the second derivatives of the KS orbitals; this quantity is

hard to calculate directly from the charge density alone. The success of DFT has been possible also thanks to the discovery and development of simple functionals that approximate the exact, but unknown, total-energy functional. Hence, the KS-DFT approach to solving the many-body Schrödinger equation translates into solving a set of non-interacting one-particle Schrödinger equations in presence of an external potential that depends, self-consistently, upon the charge density only. Although the outstanding importance of DFT has been recognized by the 1998 Nobel Prize in chemistry awarded to Walter Kohn (for DFT) and John Pople (for computational methods in quantum chemistry), its impact on the physics community has been, if possible, even greater: the top ten most highly cited articles published by the American Physical Society deal with DFT and related applications [40].

The electronic structure of materials and molecular systems is, at the same time, very similar and yet very different. To some extent, extended bulk materials can be seen as very large molecules and one could focus on the local electronic structure in real space, which is periodically repeated in the case of a crystalline materials (e.g., metals, semiconductors, oxides). This viewpoint is supported by the mathematical structure of the Schrödinger equation and its solutions, as observed by Kohn [26]: the electronic structure is fundamentally a local property, "nearsighted" to what happens at further distance in real space. The effect of chemical bonding and the presence of the lattice can be seen as perturbations to the case of isolated atoms, with their well-defined s, p, d and f orbitals. This perspective is powerful and foundational for linear-scaling methods, which target the simulation of large systems and leverage a description based on localized orbitals. Yet materials are not just very large molecules, and "more is different" [41]. Extended systems are practically infinite and can thus be described using periodic boundary conditions (PBCs). As will be discussed in more formal terms in Sec. 2, the electronic structure of a material under PBCs is more naturally described in terms of Bloch orbitals, which are not localized in real space. Indeed, a different perspective often drives the discussion of the electronic structure of periodic crystals: the behavior in reciprocal (i.e., Fourier-transformed) space. A textbook example is semiconductor physics, that is in general much better understood (and taught) by studying solutions of the Schrödinger equation in such reciprocal space. This approach, somewhat orthogonal to the large-molecule perspective, is indeed also very powerful both at a conceptual and practical level. As a side note, many electronic-structure codes for materials actually adopt a completely delocalized basis (e.g., plane waves) to describe the periodic part of the Bloch orbitals [36, 42, 43].

How can we reconcile these two, almost opposite, perspectives? Remarkably, one can use the fundamental "gauge freedom" of quantum mechanics: First, any quantum state is defined modulo a phase factor. Second, if one considers a set of single-particle states separated in energy from other states, then any trace operation on this manifold is invariant with respect to any unitary transformation among the orbitals; we call this a "generalized" gauge freedom. However, and this is the crucial aspect, the localization properties of that set of states strongly depend on their gauge.

WFs provide a rigorous and insightful way to reconcile the real-space and localized perspective with the reciprocal-space (Fourier) and delocalized one. As it will be clear in the next section, MLWFs in particular exploit the generalized gauge freedom to transform delocalized orbitals into localized ones (and vice versa), by constructing the proper unitary matrices.

2 Wannier functions fundamentals

The electronic structure of periodic crystals is most commonly described in terms of Bloch waves $\psi_{n\mathbf{k}}(\mathbf{r}) = u_{n\mathbf{k}}(\mathbf{r})\, e^{i\mathbf{k}\cdot\mathbf{r}}$, where $\mathbf{k}$ is the crystal momentum, and n is the band index. This is the case in textbooks on solid-state theory, but also for the many software packages that solve the KS equations for crystalline solids. A few years after Felix Bloch developed the theory of electron waves in periodic crystals [44], Gregory Wannier introduced an alternative representation in terms of an orthonormal set of localized functions [3], the Wannier functions. Given an isolated Bloch band n, the WF $w_{n\mathbf{R}}(\mathbf{r}) = \langle \mathbf{r}|\mathbf{R}n\rangle = w_{n\mathbf{0}}(\mathbf{r}-\mathbf{R})$ associated with the unit cell labelled by lattice vector $\mathbf{R}$ is defined as [3]

$$|\mathbf{R}n\rangle \;=\; \frac{V_{\text{cell}}}{(2\pi)^3}\int_{\text{BZ}} d\mathbf{k}\; e^{-i\mathbf{k}\cdot\mathbf{R}}\;|\,\psi_{n\mathbf{k}}\,\rangle\,, \tag{1}$$

where V_{cell} is the unit-cell volume.

Since their inception, WFs have been employed as a conceptual tool to tackle problems in solid-state physics (see, e.g., [45]). However, in the first sixty years following Wannier's paper, there were few actual calculations of WFs for real materials (see, e.g., [46–48]). The main obstacle was the fact that WFs are strongly non-unique, being sensitive to the generalized gauge freedom discussed earlier, e.g., to k-dependent phase changes $|\psi_{n\mathbf{k}}\rangle \to e^{-i\beta_{n\mathbf{k}}}\,|\psi_{n\mathbf{k}}\rangle$ with $\beta_{n\mathbf{k}} \in \mathbb{R}$ (gauge transformations) of the Bloch eigenstates. In addition, the energy bands of real materials typically become degenerate at points, lines, or even entire planes in the BZ. The presence of degeneracies leads to poor localization properties of the WFs obtained from Eq. (1), because no matter how the phase factors $e^{-i\beta_{n\mathbf{k}}}$ are chosen, the Bloch eigenfunctions are non-differentiable functions of $\mathbf{k}$ at the degeneracy points.

2.1 Maximally localized Wannier functions

In the following, we discuss the widely used Wannierization methods introduced in [4, 11], while we refer the reader to Sec. 2.4 for an overview of more recent and advanced minimization methods.

2.1.1 Isolated composite groups of bands

Consider a group of J Bloch bands of orthonormal $|\psi_{n\mathbf{k}}\rangle$ Bloch states that may be connected among themselves by degeneracies, but are isolated from all lower or higher bands, e.g., the six valence bands in Fig. 3. Given such a composite group, the most general expression for the associated WFs is [4]

$$|\mathbf{R}j\rangle = \frac{V_{\text{cell}}}{(2\pi)^3}\int_{\text{BZ}} d\mathbf{k}\, e^{-i\mathbf{k}\cdot\mathbf{R}}\,|\psi^{\text{W}}_{j\mathbf{k}}\rangle\;, \tag{2a}$$

$$|\psi^{\text{W}}_{j\mathbf{k}}\rangle = \sum_{n=1}^{J} |\psi_{n\mathbf{k}}\rangle\, U_{\mathbf{k},nj}\,, \tag{2b}$$

where the $U_{\mathbf{k}}$ are $J\times J$ unitary matrices that describe the generalized (multiband) gauge freedom within the Bloch manifold at each $\mathbf{k}$. The superscript W denotes a Wannier gauge, as opposed

to a Hamiltonian gauge (later denoted by H) where the Hamiltonian matrix is diagonal. Note that at variance with Eq. (1), in Eq. (2) there is not a one-to-one correspondence between the band index n and the intra-cell Wannier index j.

Marzari and Vanderbilt (MV) introduced the concept of MLWFs, in which the $U_{\mathbf{k}}$ matrices are chosen so as to minimize the total quadratic spread of the WFs [4]:

$$\Omega \;=\; \sum_{j=1}^{J} \Big[\langle\, \mathbf{0}j \,|\, r^2 \,|\, \mathbf{0}j \,\rangle \;-\; |\langle\, \mathbf{0}j \,|\, \mathbf{r} \,|\, \mathbf{0}j \,\rangle|^2 \Big] \,. \tag{3}$$

As discussed later (see Sec. 2.3.1) the spread (a.k.a. localization) functional Ω and its gradient with respect to an infinitesimal gauge transformation can be expressed in reciprocal space; furthermore, the BZ integration in Eq. (2a) is replaced by a discrete sum $(1/N)\sum_{\mathbf{k}}$ where N is the number of k points in the finite grid used in the numerical simulations, and the optimal $U_{\mathbf{k}}$ matrices are found by iteratively minimizing the functional Ω (see also [4] for the mathematical details).

From general Fourier-transform considerations [49], the good real-space localization properties of the MLWFs on the left-hand side of Eq. (2a) mean that the Bloch-like states $|\psi^{\mathrm{W}}_{j\mathbf{k}}\rangle$ appearing on the right-hand side are smooth functions of $\mathbf{k}$ for the optimal choice of $U_{\mathbf{k}}$ matrices in Eq. (2b) (or for any other choice leading to well-localized WFs).

The details of the MV methodology can be found in [4, 5]; in the case of single k-point sampling (large unit cells), it is equivalent to the Foster-Boys scheme used in quantum chemistry to construct localized molecular orbitals [15]. It should be noted that other localization criteria can be used for the purpose of obtaining localized orbitals, e.g., the Edmiston–Ruedenberg [14] and Pipek–Mizey [50] approaches, based on maximizing the Coulomb self-repulsion of the orbitals and the sum of the squares of the Mulliken charges [51] associated with the orbitals, respectively. Whilst these are more challenging to adapt to a periodic, multi-k-point formulation, there has been recent work to obtain WFs for periodic systems using the Pipek–Mezey localization criterion [52, 53]. Nevertheless, the MV approach of minimizing the quadratic spread is still the most widely used approach for periodic systems.

To provide an illustrative example of the Wannierization procedure, we briefly discuss here the simple example of a slightly dimerized polyyne-like carbon chain, i.e., a chain of carbon atoms with two atoms per unit cell and alternating distances d_1 and d_2. Fig. 1 displays the results of actual DFT calculations, where carbon–carbon distances are $d_1 = 1.245$Å and $d_2 = 1.345$Å, and the lattice parameter is thus $a = 2.6$Å. We compute the electronic band structure of this linear chain with the `Quantum ESPRESSO` code [54, 55], which uses pseudopotentials with a plane-wave basis set, where the bands originating from the $1s$ orbitals of carbon are not explicitly computed. If these $1s$ core orbitals were computed explicitly, they would be almost-flat bands (since the orbitals are very localized) at lower energy. At the center of panel (c) of Fig. 1 we show the two lowest bands considered in the DFT calculation. A projected density of states calculation (not shown here) shows that these two lowest bands originate from a combination of $2s$ and $2p_x$ orbitals centered on the two atoms in the unit cell. In addition to being separated from all other bands, these two bands are also separated from each other by a small gap at X (the two bands would instead be degenerate at X for a non-dimerized chain, i.e., when $d_1 = d_2$). Therefore, they are isolated, and each of them can be Wannierized separately.

In Figure 1(c), we also plot the wavefunctions $\psi_{n\mathbf{k}}$ as provided by the *ab initio* engine, computed on a regular $4 \times 1 \times 1$ grid in the BZ composed of the four points $\mathbf{k}_1 = \Gamma = (0,0,0)$, $\mathbf{k}_2 = (\pi/2a, 0, 0)$, $\mathbf{k}_3 = \mathrm{X} = (\pi/a, 0, 0)$, $\mathbf{k}_4 = (3\pi/2a, 0, 0)$. The legend to interpret these plots is provided in panel (a) of Fig. 1: in particular, we represent the real (green) and imaginary (red) components of complex wavefunctions (e.g., $\psi_{n\mathbf{k}}$, $\psi^{\mathrm{W}}_{n\mathbf{k}}$, ...) along the x axis passing through the carbon chain, i.e., $\psi_{n\mathbf{k}}(x, 0, 0)$. Given the $4\times1\times1$ sampling of the BZ, both the wavefunctions and the resulting WFs are periodic in a real-space $4 \times 1 \times 1$ supercell, i.e., the same one shown in the panels of Fig. 1. Note that, while in most use cases the $\psi_{n\mathbf{k}}$ are eigenstates of the Hamiltonian, this might not be true for all codes. In general, the phases of each state $\psi_{n\mathbf{k}}$ are random (e.g., they often come from independent diagonalizations at each k point). In addition, if we consider multiple bands with degeneracies, then the degenerate states would also be randomly mixed among each other. (This would happen, for instance, at the k point X for a non-dimerized chain, as discussed earlier.) As a consequence, the simple sum of the $\psi_{n\mathbf{k}}$ according to Eq. (1) does not provide a well-localized function, as shown in panel (d) of Fig. 1.

However, each $\psi_{n\mathbf{k}}$ at every k point can be rotated by the optimized $U_{\mathbf{k}}$ matrices obtained from a Wannierization procedure. In this case, since $J = 1$, the $U_{\mathbf{k}}$ at each k point is a 1×1 matrix, i.e., simply a complex phase $U_{\mathbf{k}} = e^{i\phi_{\mathbf{k}}}$ that can be visualized as a rotation in the plot; this is marked by the blue circular arrow in Fig. 1(a). In this simple one-dimensional case (i.e., for a single band) the Wannierization is essentially trivial, as discussed e.g. in Sec. IV.C.1 of Ref. [4]: one has to just impose that the same-band overlaps between adjacent k points are equal to $e^{i\phi_n/4}$, where ϕ_n is the the Berry phase of the entire band n and the factor $\frac{1}{4}$ accounts for the fact that there are four k points (see later Eq. (69) in Sec. 3.6 for a discussion of Berry phases). This condition is realized by making the appropriate phase rotations $e^{i\phi_{\mathbf{k}}}$ at every k point that counterbalance the random phases coming from the *ab initio* code, thus delivering maximal smoothness in reciprocal space, corresponding to the so-called twisted parallel-transport gauge [10]. The rotated states $\psi^{\mathrm{W}}_{n\mathbf{k}}$ are shown in panel (e) and (g) for the second lowest ($n = 2$) and lowest ($n = 1$) bands, respectively. When these $\psi^{\mathrm{W}}_{n\mathbf{k}}$ are summed as prescribed by Eq. (2a), localization emerges and we obtain the final MLWFs WF_1 and WF_2, shown both in panels (f) and (h), respectively, and in panel (b) as 3D isosurfaces. Note that a final global phase rotation might be required to ensure real-valued MLWFs. Intuitively, WF_1 can be interpreted as (predominantly) originating from a linear combination of s orbitals on the C atoms, while WF_2 as (predominantly) originating from a linear combination of p_x orbitals on the C atoms (with opposite signs, so that the positive part of the p_x orbitals centered on two neighboring C atoms sums constructively in the middle of the C–C bond).

We can also treat the two bottom energy bands as a composite group. In this case the $U_{\mathbf{k}}$ are 2×2 unitary matrices, whose action on the Bloch wavefunctions,

$$\begin{pmatrix} \psi^{\mathrm{W}}_1 & \psi^{\mathrm{W}}_2 \end{pmatrix} = \begin{pmatrix} \psi_1 & \psi_2 \end{pmatrix} \begin{pmatrix} U_{11} & U_{12} \\ U_{21} & U_{22} \end{pmatrix}, \tag{4}$$

is represented schematically in Fig. 2(a). We note that, in such a simple case with only two bands, the action of a unitary matrix could be generally interpreted as a sequence of complex phase rotations of the two initial states, a rotation that mixes the two states, and a final additional complex phase rotation between the two final states. In this case, each pair of $\psi_{n\mathbf{k}}$ at every k

point can be mixed by the optimized $U_{\mathbf{k}}$ matrices obtained from a Wannierization procedure. The rotated states $\psi^{\rm W}_{n\mathbf{k}}$ are shown in panel (e) (for convenience of the reader, we repeat in panels (c) and (d) of Fig. 2 the same band structure and $\psi_{n\mathbf{k}}$ wavefunctions as in panels (c) and (d) of Fig. 1). When these $\psi^{\rm W}_{n\mathbf{k}}$ are summed as prescribed by Eq. (2a), we obtain the final MLWFs $|\mathbf{R}j\rangle$ ($j = 1, 2$) shown in panel (f), and localization is now apparent (the figure shows the MLWFs for $\mathbf{R} = \mathbf{0}$). Also in this case, a final global phase rotation might be required to ensure real-valued MLWFs. We finally note that, since we now give more freedom to the states to mix, the resulting MLWFs are more localized than those of Fig. 1(b). Also, the two WFs of Fig. 1 (separate Wannierization) can be obtained as a linear combination of the eight WFs of Fig. 2 (combined Wannierization), i.e., WF_1 and WF_2 translated by $\mathbf{R}_{-1} = (-a, 0, 0)$, $\mathbf{R}_0 = (0, 0, 0)$, $\mathbf{R}_1 = (a, 0, 0)$ and $\mathbf{R}_2 = (2a, 0, 0)$. The opposite is also true: WF_1 and WF_2 of Fig. 2 are a linear combination of the eight WFs of Fig. 1 translated by $\mathbf{R}_{-1}$, $\mathbf{R}_0$, $\mathbf{R}_1$, $\mathbf{R}_2$.

2.1.2 Entangled bands

The MV approach described above provides a means to construct well-localized WFs from isolated groups of bands, such as the valence bands of insulators. However, it is often useful to obtain WFs from non-isolated (or "entangled") groups of bands. Typical examples include the low-lying conduction bands or the valence plus conduction bands of insulators (see Fig. 3), and the bands crossing the Fermi level in metals.

A possible strategy to deal with such cases is to first identify an appropriate J-dimensional Bloch manifold at each k point from a larger set of $\mathcal{J}_{\mathbf{k}}$ Bloch eigenstates $|\psi_{m\mathbf{k}}\rangle$, e.g., the ones within some energy window. Formally, this band-disentanglement step can be expressed as

$$|\tilde{\psi}_{n\mathbf{k}}\rangle = \sum_{m=1}^{\mathcal{J}_{\mathbf{k}}} |\psi_{m\mathbf{k}}\rangle\, \tilde{V}_{\mathbf{k},mn}\,, \tag{5}$$

where the $\tilde{V}_{\mathbf{k}}$ are $\mathcal{J}_{\mathbf{k}} \times J$ matrices satisfying $\tilde{V}^{\dagger}_{\mathbf{k}}\tilde{V}_{\mathbf{k}} = \mathbb{1}_{J\times J}$. In 2001, Souza, Marzari and Vanderbilt [11] (SMV) introduced a practical scheme to extract an optimally smooth Bloch-like subspace $\hat{P} = \sum_{n=1}^{J} |\tilde{u}_{n\mathbf{k}}\rangle\langle\tilde{u}_{n\mathbf{k}}|$ across the BZ, from which a set of MLWFs could then be obtained using the MV prescription. The resulting "disentangled WFs" are given by Eq. (2) with the *ab initio* Bloch eigenstates $|\psi_{n\mathbf{k}}\rangle$ therein replaced by the disentangled Bloch-like states $|\tilde{\psi}_{n\mathbf{k}}\rangle$, that is,

$$|\mathbf{R}j\rangle = \frac{1}{N}\sum_{\mathbf{k}} e^{-i\mathbf{k}\cdot\mathbf{R}}\, |\psi^{\rm W}_{j\mathbf{k}}\rangle\,, \tag{6a}$$

$$|\psi^{\rm W}_{j\mathbf{k}}\rangle = \sum_{n=1}^{\mathcal{J}_{\mathbf{k}}} |\psi_{n\mathbf{k}}\rangle\, V_{\mathbf{k},nj}\,, \tag{6b}$$

where the $\mathcal{J}_{\mathbf{k}} \times J$ matrices $V_{\mathbf{k}} = \tilde{V}_{\mathbf{k}}U_{\mathbf{k}}$ encode the net result of the disentanglement (subspace-selection) and maximal localization (gauge-selection) steps. As in the case of Eq. (2), the states $|\psi^{\rm W}_{j\mathbf{k}}\rangle$ in Eq. (6) are smooth functions of $\mathbf{k}$ whenever the associated WFs are well localized.

The disentanglement step can be carried out in such a way that the *ab initio* eigenstates are described exactly within a "frozen" or "inner" energy window that is contained by the "outer" energy window mentioned earlier [11]. This is useful, for example, when studying transport

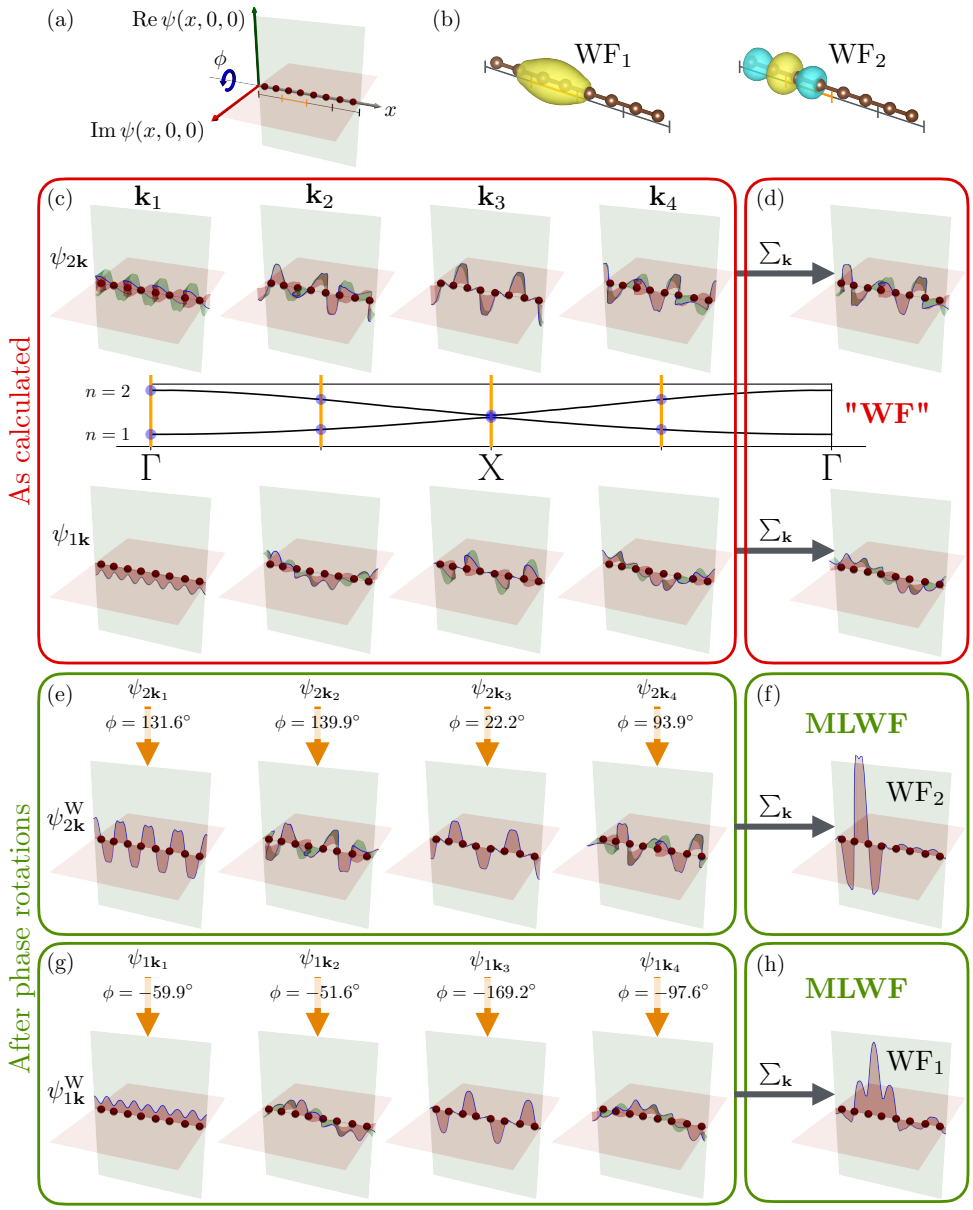

Figure 1: Band-by-band Wannierization of the two lowest bands of a dimerized carbon chain. (a) Graphical representation of the 4-times longer supercell where all quantities will be plotted in panels (c)–(h); given our sampling of the BZ with 4 k points, both the Bloch states and the WFs have the supercell periodicity. The eight carbon atoms are represented as dark red spheres, and the primitive cell of length a is marked by the orange segment. One axis is the real-space x axis of the carbon chain, while the other two are used to plot the real (green) and imaginary (red) components of complex wavefunctions $\psi(x,0,0)$ along x (the profiles are highlighted in blue in subsequent panels). Multiplying ψ by a phase factor $e^{i\phi}$ corresponds to a rotation by an angle ϕ, as indicated by the blue arrow. (b) 3D isosurfaces of the resulting MLWFs for each of the two bands (band $n=1$ leads to WF$_1$, $n=2$ leads to WF$_2$). (c) The Bloch orbitals $\psi_{n\mathbf{k}}$ as calculated by the *ab initio* (DFT) code on the k points $\mathbf{k}_1 = \Gamma = (0,0,0)$, $\mathbf{k}_2 = (\pi/2a,0,0)$, $\mathbf{k}_3 = \mathrm{X} = (\pi/a,0,0)$, $\mathbf{k}_4 = (3\pi/2a,0,0)$ indicated by the blue dots and vertical orange lines in the center of the panel, together with the full DFT band structure. (d) The sum of these Bloch orbitals, as in the original Wannier definition of Eq. (1), delivers Wannier functions "WF" that are not well localized. (e) The construction of a MLWF associated with the second lowest band ($n=2$). For an isolated band in one dimension, the procedure amounts to a complex phase rotation at each k point; the optimal values of these complex phases for this specific example are indicated. (f) The sum of these rotated Bloch states results in the MLWF WF$_2$, also shown in panel (b). (g) and (h) are the same as (e) and (f), but for the lowest band ($n=1$).

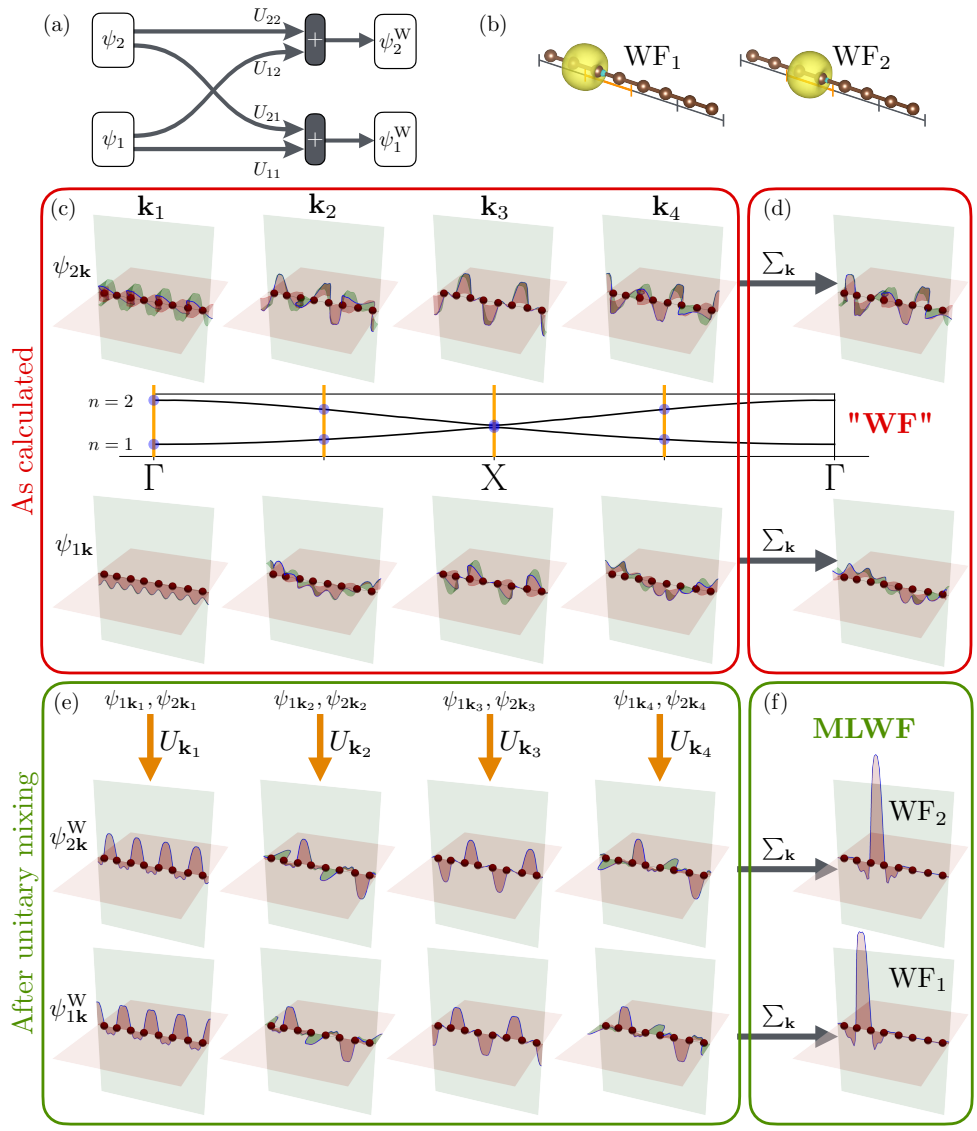

Figure 2: Same as Fig. 1, but now treating the two lowest bands as a composite group. (a) Graphical representation of the generalized gauge transformation $U_{\mathbf{k}}$ in Eq. (4) that mixes the Bloch states from the two bands. As the result of this mixing, it is no longer possible to associate each MLWF obtained from Eq. (1) with a specific band. By taking advantage of the generalized gauge freedom, the two composite MLWFs in the $\mathbf{R} = 0$ cell, shown in panels (b) and (f), are better localized than their single-band counterparts in Fig. 1. Note that WF_1 and WF_2 are not identical, i.e., they are not related by a rigid translation, even though they are both bond centered and look similar. This is because the chain is dimerized, and thus the respective bond lengths are different.

properties, for which one would like to obtain a faithful description of the states within some small energy range around the Fermi level. Note that because of these energy windows, the required input from the first-principles calculation includes the energy eigenvalues $\varepsilon_{n\mathbf{k}}$ in addition to the overlap matrices Eq. (12). For illustrative purposes, in Fig. 4 we display the $\tilde{V}_{\mathbf{k}}$ matrices as calculated for the carbon chain discussed earlier. We also stress that, in this simple illustrative example, we can exactly disentangle all six bands from the rest, but this is not true in general (see, for example, the conduction bands in Fig. 3).

Over the years, many alternative approaches and algorithms have been developed—from partially occupied Wannier functions [56, 57] to quasi-atomic orbitals [58], to the selected columns of the density matrix (SCDM) [59, 60], and to projectability disentanglement and manifold remixing [61, 62]; these and others will be discussed in Sec. 2.4.

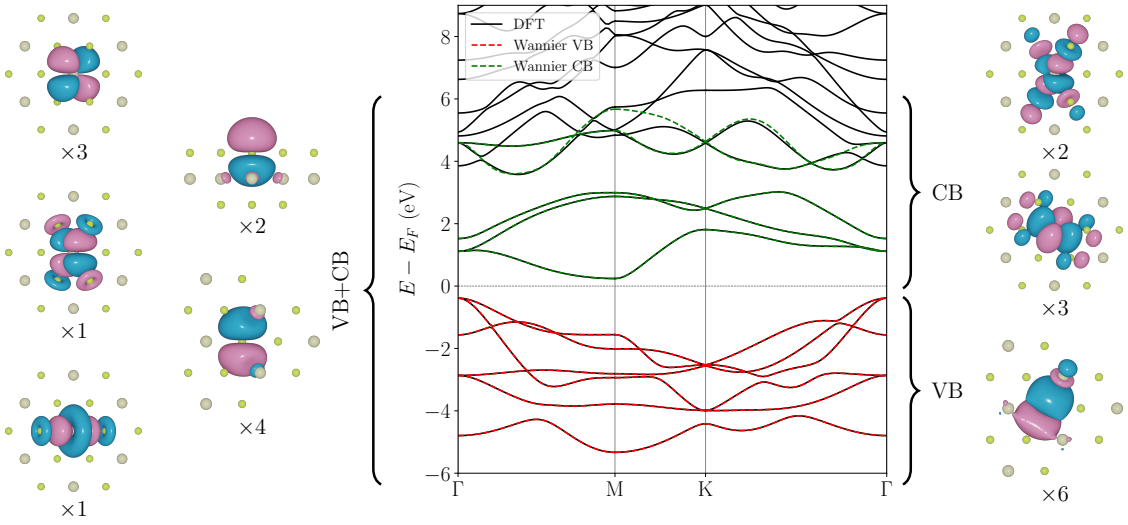

Figure 3: MLWFs and band structure of the 2D material $HfSe_2$. In the center, the comparison between the DFT band structure (black lines) and the Wannier-interpolated band structure from valence MLWFs only (VB, red dashed lines) and from low-lying conduction MLWFs only (CB, green dashed lines) are shown. Note that the Wannier-interpolated bands from both valence + conduction MLWFs together (VB+CB) are not shown since they are visually indistinguishable from the combination of the VB and CB MLWFs. On the left, we show the real-space shapes of (in total 11) valence + conduction MLWFs, obtained starting from Hf d and Se p initial guess orbitals, followed by disentanglement (see Sec. 2.1.2) from high-energy conduction states: specifically, three of them resemble $d_{xy,xz,yz}$ orbitals, one resembles a d_{z^2} orbital, one resembles a $d_{x^2-y^2}$ orbital, and the remaining six resemble p orbitals. Some small hybridization with orbitals from nearby atoms is visible. On the right, we show the real-space shapes of (in total 6) valence MLWFs (lower panel) and (in total 5) conduction MLWFs (upper panel). The valence MLWFs span an isolated group of bands (see Sec. 2.1.1) and are composed by six hybridized bonding orbitals, where the Hf d and Se p orbitals overlap constructively. The conduction MLWFs are instead five hybridized anti-bonding orbitals, where Hf d and Se p orbitals overlap destructively, forming nodal planes close to bond centers. (The notation $\times n$ below each shape denotes the multiplicity of the corresponding MLWF, i.e., n MLWFs having similar shapes but different spatial orientation.)

2.1.3 The projection method

The MV and SMV approaches leverage iterative minimization, hence a good starting guess for the unitary matrices $U_{\mathbf{k}}$ and $\tilde{V}_{\mathbf{k}}$ is crucial to avoid being trapped in local minima of the spread functional. A popular approach is the *projection method*, where a set of J localized "trial functions" $g_n(\mathbf{r})$ are chosen by guessing the orbital character and location of the target WFs. These functions are typically Gaussians, atomic-like orbitals with angular character such

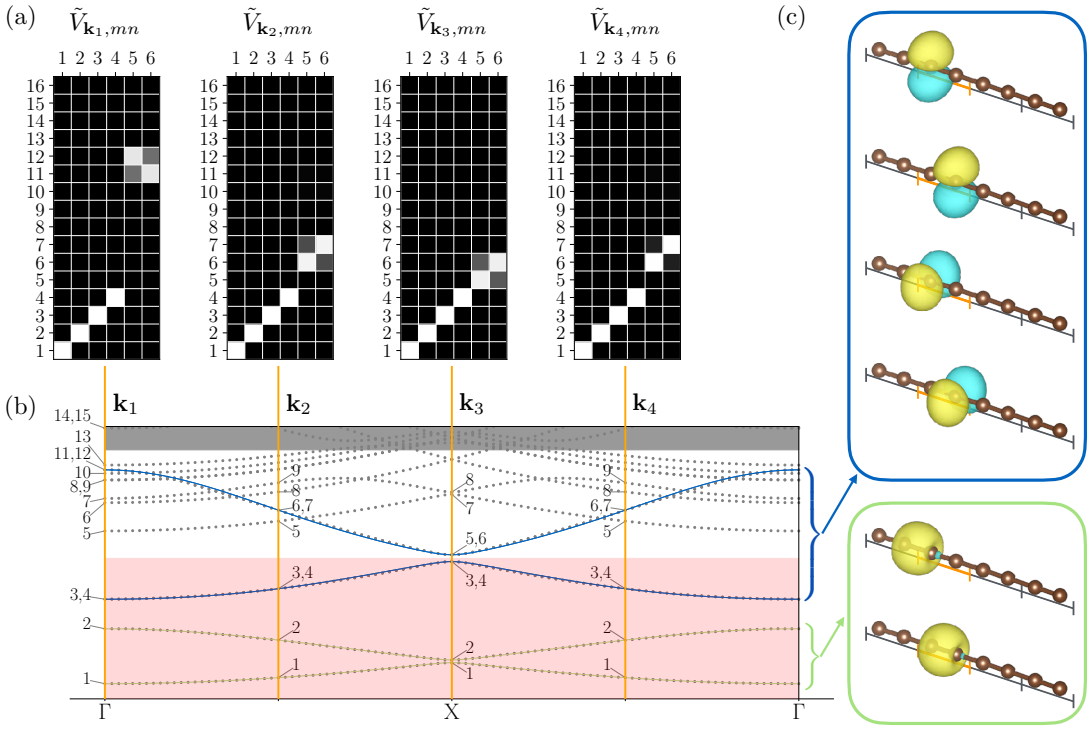

Figure 4: Illustration of the disentanglement procedure for the same linear carbon chain as in Figs. 1 and 2. (a) Graphical representation of the $\tilde{V}_{\mathbf{k},mn}$ matrices in Eq. (5) at k points $\mathbf{k} = \mathbf{k}_1$, $\mathbf{k}_2$, $\mathbf{k}_3$, $\mathbf{k}_4$. The color scale represents the absolute values of the matrix elements from black (zero) to white (maximum absolute value). The index m (from 1 to 16) labels the bands, and the index n (from 1 to 6) labels the disentangled Bloch states $|\tilde{\psi}_{n\mathbf{k}}\rangle$. (b) Band structure of the carbon chain. Dotted gray points denote the DFT bands, solid lines the disentangled (Wannier-interpolated) bands. The frozen energy window is shown with a red background, while the energy range with gray background is outside the disentanglement window. The relevant band indices at $\mathbf{k}_1$, $\mathbf{k}_2$, $\mathbf{k}_3$ and $\mathbf{k}_4$ are indicated. The six disentangled bands are shown in green (bottom two, the same bands as in Figs. 1 and 2) and in blue (top four, doubly degenerate). To construct the topmost blue bands, the disentanglement procedure correctly picks up the optimally connected DFT bands as a function of $\mathbf{k}$: bands 11 and 12 at $\mathbf{k}_1$, bands 6 and 7 at $\mathbf{k}_2$ and $\mathbf{k}_4$, and bands 5 and 6 at $\mathbf{k}_3$. Notably, in this example the topmost blue bands can be exactly disentangled from all other DFT bands, such that the disentangled bands coincide at every $\mathbf{k}$ with the corresponding DFT bands. We note, however, that this is not possible in general for an arbitrary band structure (compare, for instance, with the conduction bands in Fig. 3). (c) Resulting MLWFs on a $4 \times 1 \times 1$ supercell (the primitive unit cell is indicated by the orange segment). Since in this specific example the disentanglement matrices $\tilde{V}$ are block diagonal (as well as the U matrices from the Wannierization procedure, not shown here), the two bonding-like MLWFs originate only from the bottom two (green) bands and do not mix with the four p_y and p_z MLWFs from the other four (blue) bands.

as s, p, d, or hybrid orbitals such as sp^3. The first step is to project the Bloch manifold onto these trial orbitals:

$$|\phi_{n\mathbf{k}}\rangle = \sum_{m=1}^{\mathcal{J}_{\mathbf{k}}} |\psi_{m\mathbf{k}}\rangle \langle\psi_{m\mathbf{k}}|g_n\rangle \,. \tag{7}$$

Then, Löwdin orthonormalization is performed by inverting the overlap matrix $S_{\mathbf{k},mn} = \langle\phi_{m\mathbf{k}}|\phi_{n\mathbf{k}}\rangle = (A^\dagger A)_{\mathbf{k},mn}$

$$|\tilde{\psi}_{n\mathbf{k}}\rangle = \sum_{m=1}^{\mathcal{J}_{\mathbf{k}}} |\psi_{m\mathbf{k}}\rangle \, (A_{\mathbf{k}} S_{\mathbf{k}}^{-\frac{1}{2}})_{mn} \tag{8}$$

where the $A_{\mathbf{k},mn} = \langle\psi_{m\mathbf{k}}|g_n\rangle$ is called the projection matrix. The matrix $A_{\mathbf{k}} S_{\mathbf{k}}^{-\frac{1}{2}}$ is unitary and can be computed through the singular value decomposition of $A = ZDW$:

$$A_{\mathbf{k}} S^{-\frac{1}{2}} = Z\mathbb{1}W, \tag{9}$$

where the diagonal matrix D is replaced with the identity $\mathbb{1}$.

The choice of the trial orbitals for composite bands is less critical with respect to entangled bands and, for simple compounds, even a set of Gaussians randomly centered in the cell might work. We emphasize that if the manifold of composite bands coincide with the valence band of an insulator or semiconductor, then the MLWFs will reflect the local chemistry: for instance, in covalent materials MLWFs are typically bond-centered as in Si or GaAs [4], with some notable exceptions such as MoS_2 [63] where one WF is centered in the middle of the hexagonal cell due to the hybridization of several orbitals. On the contrary, the SMV disentanglement hinges on a careful choice of trial functions, that define the orbital character of the bands to be extracted. Whilst disentangling at once the valence and conduction manifold often yields atom-centered WFs, this is not true in general: MLWFs for the low-lying bands of copper result in five Cu d-like WFs and two additional WFs centered at the tetrahedral-interstitial locations [11].

Different aspects of the projection method are discussed in Sec. 2.3 and 2.4.

2.2 Major applications of Wannier functions

Interpolation The efficient interpolation in reciprocal space of k-dependent quantities is arguably the most common application of WFs, enabling the calculation of simple (e.g., the band structure) or complex (e.g., electron-phonon coupling) electronic-structure properties. A large part of this review is devoted to the fundamentals of WF interpolation (Sec. 3.3) and their applications, including ballistic transport (Sec. 3.4), Berry-phase related properties (Sec. 3.5) and electron-phonon interactions (Sec. 3.7). As discussed in more detail in Sec. 3.3, the reason for such widespread set of applications (not all of them covered in this review) is that WFs can be easily applied to any generic operator that is local in reciprocal space, i.e., any lattice-periodic operator. More generally, we note that even some non-local operators in reciprocal space (e.g. containing the position operator, which is not lattice periodic and transforms into k derivatives) can also be interpolated, see e.g. Sec. 3.5 on Berryology. Equally important is that WFs allow reproducing the correct band connectivity: in particular, avoided crossings are not mistaken for actual crossings. This distinguishes Wannier interpolation from other methods based on direct Fourier interpolation of the energy eigenvalues. In other words, WFs allow to exploit the

fundamental locality ("nearsightedness" according to Kohn [24–26]) of the electronic structure and the related exponential localization of WFs to construct a potentially exact representation of an operator in real space, such that any interpolation back to reciprocal space is exact as well. The procedure is also systematic as WFs are guaranteed to exist and the convergence is exponential with the linear sampling density [21–23]; prefactors and coefficients might depend on electronic-structure properties such as the band gap, and on the specific operator under consideration.

Geometry and Topology WFs have several profound connections with quantum-geometrical and topological aspects of the electronic structure [10]; some of them are discussed in Sec. 3.5 and 3.6. In the following, we refer to topological properties as a subset of geometrical properties that are quantized and hence represented by integer topological invariants robust to certain classes of perturbations. A prime example of geometrical—and in some circumstances also topological—quantity is the electric polarization of periodic solids, which can be calculated in reciprocal space as a Berry phase [10] (see Sec. 3.5). Electric polarization can also be equivalently computed by summing over WFs centers in real space [4, 5, 10], which provides a more intuitive formulation of the modern theory of polarization [10, 19, 20, 64] and restores some justification to the classical Clausius–Mossotti [65, 66] viewpoint. While electronic-structure geometry in reciprocal space speaks the language of differential geometry (e.g., curvatures, parallel transport, smoothness of manifolds), WFs allow to express the same quantities in terms of matrix elements of the Hamiltonian and position operator $\hat{\mathbf{r}}$. The reciprocal-space smoothness, which is measured by the quantum geometric tensor [67], can be equivalently analyzed in real space by measuring the degree of WFs localization.

To some extent, the connection between WFs and topological invariants is even stronger, where the former provide not only powerful approaches to calculate invariants for real materials (see Sec. 3.6 for a discussion) but also fundamental understanding of topological phases. In fact, topological insulators are essentially systems that cannot be connected adiabatically to atomic insulators, hence it is impossible to truly represent their ground state with WFs [10, 68]. In reciprocal space, non-trivial topological invariants translate into unavoidable obstructions to choosing a smooth gauge over the BZ [10, 69]. The fundamental connection between non-trivial topology of electronic bands and the corresponding absence of a Wannier representation has been recently generalized and made systematic in the context of elementary band representation [70, 71], leading to the so-called topological quantum chemistry [72–74] (see also related efforts on symmetry-based indicators by [75–78]), allowing to screen materials databases and identify non-trivial materials of various classes [79–82].

Advanced electronic-structure methods DFT simulations of periodic solids can be conveniently (but definitely not necessarily) performed by adopting a plane-wave basis set, in conjunction with smooth pseudopotentials that reproduce the interaction between valence electrons and nuclei plus core electrons [36]. The resulting KS eigenstates are also not particularly localized functions, and DFT is invariant under unitary rotations of the occupied electronic states. However, several electronic-structure methods, aiming at improving or complementing the capabilities of DFT, fundamentally require to be formulated in terms of localized orbitals (see

Sec. 3.8). In addition, several of these beyond-DFT methods are not deployed directly on the crystal structure, but operate more as corrections to starting DFT calculations. Also, beyond-DFT methods can be computational rather intensive, and it is common practice to apply them only on a subset of bands extracted from the entire manifold. In this context, WFs provide a robust way to bridge DFT with advanced electronic-structure methods by allowing to systematically construct orthogonal localized states that represent the manifold of interest: WFs are first constructed on the KS DFT solution and then fed into beyond-DFT methods; a technical overview of how this is carried out in practice is the subject of Sec. 3.8.

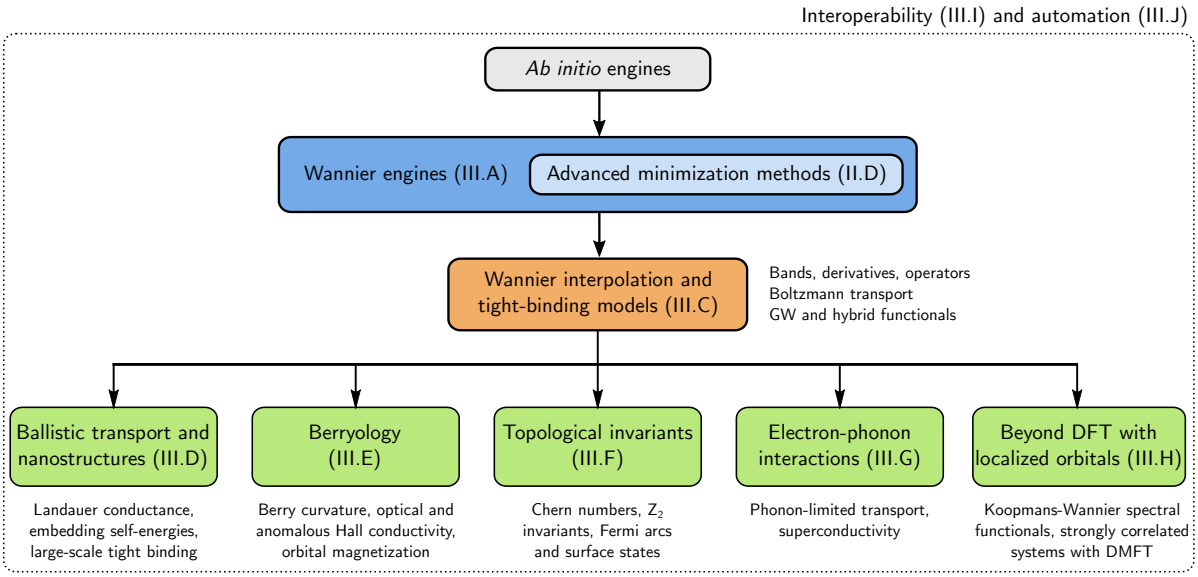

Figure 5: Overall schematics of how different codes in the ecosystem interact. This figure serves also as a "table of contents" to this review, where sections describing the relevant blocks are indicated in the figure. At the top, the *ab initio* engines (grey block) generate the data that is transferred to a Wannier engine (blue block), that might implement also advanced methods discussed in Sec. 2.4. Once WFs are obtained, they are typically used to generate a TB model and perform interpolation of the Hamiltonian and other operators (orange block). Such interpolated quantities are used for a number of different applications; the ones that are discussed in more detail in this review are indicated in the green blocks. As schematically indicated by the outer dotted rectangle, all these codes forming the Wannier ecosystem may be automated with workflow tools, which also coordinate data transfer between them.

2.3 Wannier functions for the practitioner

2.3.1 The spread functional in reciprocal space

The Blount identities [16] provide the matrix elements of the position operator between WFs, and, remarkably, prefigure the link between macroscopic properties and integrals (Berry phases) of Berry connections [20]:

$$\langle \mathbf{R}i|\mathbf{r}|\mathbf{0}j\rangle = i\,\frac{V_{\rm cell}}{(2\pi)^3}\int d\mathbf{k}\, e^{i\mathbf{k}\cdot\mathbf{R}}\langle u_{i\mathbf{k}}|\nabla_{\mathbf{k}}|u_{j\mathbf{k}}\rangle \tag{10}$$

and

$$\langle \mathbf{R}i|r^2|\mathbf{0}j\rangle = -\frac{V_{\rm cell}}{(2\pi)^3}\int d\mathbf{k}\, e^{i\mathbf{k}\cdot\mathbf{R}}\langle u_{i\mathbf{k}}|\nabla^2_{\mathbf{k}}|u_{j\mathbf{k}}\rangle \ . \tag{11}$$

It is through these identities that one can recast the spread functional Ω using reciprocal-space expressions, where the gradients and higher derivatives are obtained from finite differences. The

building blocks for these finite-difference expressions are the overlap matrices

$$M_{ij}^{(\mathbf{k},\mathbf{b})} = \langle u_{i\mathbf{k}} | u_{j\mathbf{k}+\mathbf{b}} \rangle \tag{12}$$

between cell-periodic Bloch eigenstates $|u_{n\mathbf{k}}\rangle$ at neighboring points on a regular grid in the BZ (the $\mathbf{b}$ vectors connect one k point to its neighbors on a regular discrete grid); in the limit of very dense meshes the $\mathbf{b}$ vectors tend to zero and the gradient in $\mathbf{k}$ is recovered. This finite-difference construction remains valid even in the case of Γ-sampling (e.g. for molecular systems treated with PBCs or when considering large supercells), where the neighboring k points are given by the primitive reciprocal lattice vectors $\mathbf{G}$, with the Bloch orbitals differing just by phase factors $\exp(i\mathbf{G}\cdot\mathbf{r})$. Now, we note that the gradient in $\mathbf{k}$ of a function $f(\mathbf{k})$ can be written as

$$\nabla f(\mathbf{k}) = \sum_{\mathbf{b}} w_b \, \mathbf{b} \, [f(\mathbf{k}+\mathbf{b}) - f(\mathbf{k})] + \mathcal{O}(b^2) \tag{13}$$

using stars ("shells") of neighboring k points, where each shell has a weight w_b (see Appendix B in [4] and [83] for a detailed description); for a linear function $f(\mathbf{k}) = f_0 + \mathbf{g}\cdot\mathbf{k}$ it can be easily verified that the exact result $\nabla_\alpha f(\mathbf{k}) = g_\alpha$ is recovered. In the simple case of cubic Bravais lattices, the first shell of reciprocal-space nearest neighbors (6, 8 or 12 for Bravais lattices in direct space that are simple cubic, FCC, or BCC) is sufficient; the general case where several shells need to be chosen automatically is detailed in [83]. While the procedure is automated, for unusual cases (e.g., very elongated cells) it might be convenient to find manually the most symmetric choice of shells [84]. With these definitions, the diagonal matrix elements of the position operator can be evaluated by finite differences as

$$\langle \mathbf{0}i | \mathbf{r} | \mathbf{0}i \rangle = -\frac{1}{N} \sum_{\mathbf{k},\mathbf{b}} w_b \, \mathbf{b} \, \mathrm{Im} \, \ln M_{ii}^{(\mathbf{k},\mathbf{b})}, \tag{14}$$

where N is the number of k points of the reciprocal-space grid. More complex expressions for the second derivatives and for the entire spread functional can be obtained [85], all equal to the leading order in b; the choices made in [4] were driven by the need to provide the same value for the localization functional under a transformation that shifts $|\mathbf{R}i\rangle$ by a lattice vector. We also note that when using such finite-difference formalism, the spread functional converges slowly (polynomially) with reciprocal-space sampling, and hence some care must be paid in comparing its actual values in case of calculations performed with different discrete samplings.

Importantly, the finite-differences construction is particularly convenient for constructing ML-WFs in a code-agnostic form, as the only input needed from the original first-principles calculation is encoded in the overlap matrices $M_{ij}^{(\mathbf{k},\mathbf{b})}$. Thus, once the $M_{ij}^{(\mathbf{k},\mathbf{b})}$ have been calculated, no further interaction is necessary with the electronic-structure code that calculated the ground state wavefunctions, making the entire Wannierization procedure a code-independent post-processing step (see, e.g., [86] for the extension to ultrasoft pseudopotentials and the projector-augmented wave method, and [84, 87, 88] for the full-potential linearized augmented planewave method). As regards the disentanglement procedure, note that because of energy windows the needed input from the first-principles calculation includes the energy eigenvalues $\varepsilon_{n\mathbf{k}}$ in addition to the overlap matrices Eq. (12).

2.3.2 Accuracy and convergence

While the main focus of this review is on the powerful applications of WFs, their successful use relies on the Wannierization process being done correctly: in the following, we briefly comment on fundamental tests and established procedures to assess and improve the quality of WFs.

Two major convergence parameters control the quality (and the cost) of the Wannierization procedure: the spread minimization and the k-point grid used to obtain the initial Hamiltonian eigenstates (e.g., the cell-periodic part of Bloch states, if working with PBCs).

The spread minimization is generally performed with an iterative steepest-descent or conjugate gradients algorithm until results do not change within a certain tolerance. While the iterative algorithm is in general robust, the minimization can become trapped in local minima. As introduced in Sec. 2.1.3, the strategy to avoid that is to select a very good starting point: if the initial spread is sufficiently close to the absolute minimum, it is more likely to reach it by following the local gradient. Hence, particular care needs to be paid to select good projection functions to obtain the initial unitary matrix of Eq. (6b), to be then iteratively optimized. In absence of chemical intuition, a common strategy is to calculate a projected density of states on the pseudoatomic orbitals and identify the orbital character in the energy region of interest: the atomic orbitals which project more on the relevant bands can be used as initial projection. Note that MLWFs are often not atom-centered, and atomic orbitals are not always good starting projections, as it the case of the valence bands of monolayer MoS_2 [63]. In Sections 2.4 and 3.10 we cover advanced methods to automate the selection of the starting point for the minimization procedure.

The spread functional measures the degree of localization in real space and, to some extent, the efficiency of the interpolation: more localized WFs decay faster in real space, hence they require a smaller Born–von Kármán (BvK) supercell to include all non-vanishing matrix elements of the Hamiltonian and the other operators, which in turn allows adopting coarser k-point grids in the starting electronic-structure simulation that is performed in reciprocal space. Indeed, the accuracy of band interpolation can be considered a proxy for the quality of the underlying WFs not only as regards k-point convergence: especially in the case of entangled bands (see Sec. 2.1.2), poor interpolation might signal problems in the disentanglement procedure. In addition, it is worth to emphasize that in general the Wannierization procedure is not forced to preserve symmetries (unless dedicated methods designed to do so are employed, see Sec. 2.4). Hence, the spurious splitting of symmetry-protected degeneracies in the interpolated band structure might signal convergence problems related to the minimization, to the k-point convergence or to the choice of projection functions. This holds true not only for crystalline symmetries, but also for time-reversal symmetry, which is particularly relevant in noncollinear simulations of non-magnetic materials in presence of spin-orbit coupling (e.g., topological insulators).

Among other indicators of the quality of WFs we mention the ratio between their imaginary (Im) and real (Re) part: for isolated bands (and not considering spin-orbit coupling), MLWFs at the global minimum should be real functions [4]. Note that the calculation of the Im/Re part, and anything related to WFs themselves and their visualization, requires to have access to the full Bloch orbitals, not just the overlap matrices. It is also important to emphasize that different quantities derived from WFs—such as the WF spread and centers, as well as unitary matrices

$\tilde{V}_{\mathbf{k}}$, $U_{\mathbf{k}}$—converge in general with different speeds, also depending on the specific formulation adopted [89].

Finally, we remark that many of the complications related to producing WFs for periodic solids are related to construction of a smooth gauge across the BZ. Hence, supercell Wannierizations with Γ-only sampling are typically more straightforward and less prone to be trapped in local minima. The challenge there is more on algorithmic efficiency due the large size of the systems involved; a number of Γ-only dedicated methods have been developed [90–92].

2.4 Advanced minimization methods, and beyond maximally localized Wannier functions

As discussed in section 2, there is in principle large freedom in choosing the recipe to obtain well-localized WFs. Not only one can replace the MV spread functional with other cost functions, but also different minimization procedures and their starting points can be chosen, hence affecting the resulting WFs and their localization properties. Over the years, a number of methods have been developed to address all these different aspects of the Wannierization procedure. It is worth emphasizing that for many of these methods, the initial guess already provides well-localized WFs, so that an iterative minimization can in principle be avoided. The unitary matrices $U_{\mathbf{k}}$ of these "projection-only" WFs are set directly by the initial projection functions (see Sec. 2.1.3). While this choice cannot guarantee optimal localization properties, it has the advantage of enforcing some degree of symmetry induced by the choice of atomic orbitals used as projection functions. However, in all these cases it is possible—and in some cases even recommended—to minimize the MV spread or some other functional as a final step.

The prime decision deals with the functional that is to be minimized in order to determine the unitary matrices of Eq. (6). The most popular choice is the MV MLWF procedure [4] for composite bands (see Sec. 2.1.1) and the SMV disentanglement scheme for entangled bands [11] (see Sec. 2.1.2). The minimization of the spread functional leads to very well localized WFs, hence reducing the size of the BvK supercell needed to represent operators (e.g., the Hamiltonian) in a WF basis. While MLWFs and disentanglement represent the most convenient choice in the vast majority of applications, substantial work has been done to augment the MLWF scheme or develop alternatives which satisfy the needs of specific applications.

The MLWF iterative algorithm leads to localized WFs in real space, but is not guaranteed to yield orbitals that preserve desirable crystal symmetries. This is only partially relieved using symmetric initial projections, as typically obtained by a proper selection of atomic-like orbitals. Symmetry-preserving WFs are appealing in providing the correct orbital or site symmetries for many-body approaches like dynamical mean-field theory (DMFT). Hence, it is not surprising that several non-MLWF procedures directly or indirectly include crystal symmetries in the functional to minimize. In the symmetry-adapted Wannier function (SAWF) method [93], symmetric WFs are obtained through additional constraints on the unitary matrices $U_{\mathbf{k}}$ which are based on symmetry operations of the site-symmetry group. The SAWF method is fully compatible with the maximal-localization procedure and the SMV disentanglement (and has also been recently extended to the case where a frozen window is used [94]), although the additional constraints imply a possibly larger total spread, even if some individual WFs can actually be more localized

than in the MLWF procedure. Currently, the implementation of the SAWF method in the code `Wannier90` (more about software in Sec. 3.1) is interfaced with the `Quantum ESPRESSO` distribution and, once the site positions and the orbital symmetries of the SAWFs are chosen (through the initial projection functions), the site-symmetry group can be automatically computed by the interface code. If needed, the site-symmetry group can also be manually specified by the user, to construct SAWFs with target symmetries.

While the SAWF method provides a rigorous way to include symmetries in the maximal-localization procedure, it requires quite some prior knowledge of the electronic structure of the material under study. An alternative and simpler approach is to construct selectively localized Wannier functions (SLWFs), where the MLWF procedure is applied only to a subset of the entire WFs considered [95]. In addition, some WF centers can be constrained (SLWF+C) to specific positions by adding a quadratic penalty term to the spread functional. While the SLWF+C approach does not enforce symmetries, it has been observed that the resulting WFs typically exhibit the site symmetries corresponding to the constrained centers [95]. The SLWF+C can be used in the case of entangled bands, where the SMV disentanglement step is performed as usual, while the selective localization and constrained centers are applied only to the final Wannierization step. A more in-depth review of the SAWF and SLWF+C methods, including their implementation and usage in `Wannier90`, can be found in [96]. Dedicated tools for symmetry analysis and symmetrization of the real-space WF Hamiltonian are available [97].

The localization and possibly the symmetry can crucially depend on the number of WFs considered in a given energy range. The so-called partly occupied Wannier functions (POWFs) [56] formalize this observation by including the relevant unoccupied states which lead to the minimal spread functional, essentially implementing a bonding–antibonding closing procedure. POWFs can have a high degree of symmetry, while the bonding-antibonding criterion has been shown to correspond to the condition of maximal average localization [56]. Notably, in the POWF scheme the total spread functional $\Omega = \Omega_I + \tilde{\Omega}$ is minimized at once, at variance with the SMV scheme where first the gauge-invariant part Ω_I is minimized through the disentanglement step, and only after the gauge-dependent part $\tilde{\Omega}$ is minimized through the usual MV scheme. The iterative minimization of the total spread Ω has been further developed by Damle, Levitt and Lin in [98]. They reformulated the Wannierization, which is a constrained non-linear optimization problem, as unconstrained optimization on matrix manifolds, where the SMV disentanglement procedure can be interpreted as a splitting method which represents an approximate solution.

We stress that even if minimization of the full spread functional Ω guarantees the highest degree of overall localization, several of the methods discussed here can actually produce WFs such that a subset of them might individually be more localized than their maximally localized counterparts. Along those lines, Fontana et al. developed the spread-balanced WFs [57], where they added a penalty term to the spread functional, proportional to the variance of the spread distribution among all WFs of the system. This scheme could be less prone to produce solutions with one or several poorly localized WFs, at the price of an increased total spread for the whole set. The addition of terms to the spread functional can also be used to preserve some degree of locality in energy, such as in the case of mixed Wannier-Bloch functions [99] and dually localized Wannier functions [100]. These approaches are based on a generalized spread functional [91] designed to carry both spatial localization (Wannier character) and limited spectral broadening

(Bloch character), by minimizing a functional that contains not only a spatial variance (as for MLWF) but also an energy variance.

Once a choice for the functional to be minimized is made (the total spread as in the MLWF scheme, or any other choice), there is still a lot of flexibility on the choice of algorithm to perform the minimization. First, one needs to define a starting guess for the unitary matrices $U_{\mathbf{k}}$, which is customarily obtained by specifying a set of localized projection functions through the projection method introduced in Sec. 2.1.3. While for composite bands a set of randomly centered spherically symmetric Gaussian orbitals might work, in general more sophisticated choices are required. Typically, atomic orbitals are used as projection functions, such as s, p, d-orbitals as well as hybrid orbitals (e.g., sp^3), which are often centered either on atoms or along bond directions. As discussed in Sec. 2.3.2, the choice of the right atomic orbitals is typically based on chemical intuition and can be partly informed by inspecting the projected density of states in the energy region of interest. Still, the choice of the right projection orbitals—i.e., those providing a good starting point for a successful minimization of the target functional—can often be a non-trivial task, especially in the context of automated high-throughput materials screening and, more generally, when one wants to study a novel material never investigated before (especially in case of unfamiliar orbital composition). Hence, in the last decade substantial efforts have been targeted at developing automated algorithms removing the need for users to define appropriate initial projections. A first approach in this direction is the optimized projection functions (OPFs) method [101] for composite bands. In OPF, a larger set of functions that overspan the space of MLWFs is built and used as a starting point. While in plane-wave codes the OPF approach [101] still needs the user to provide a list of initial projections, for instance atomic-like local orbitals (LOs), *ab initio* codes operating with localized (or mixed plane-wave/localized) basis sets can leverage the built-in localized orbitals. For instance, the full-potential linearized augmented-plane wave (LAPW) method can be extended by adding the so-called LOs, which are atomic-like, very localized, and can be employed in the construction of WFs. [102] combined the SMV disentanglement with the OPF method [101] to construct initial guesses for MLWFs from a set of LOs in an automated way. Finally, another set of parameters that require tuning in the standard SMV disentanglement scheme are the inner and outer energy windows. [103] targeted the removal of the need for manual input by focusing on the automated optimization of both windows.

On the algorithmic side, in the quest for fully automating the generation of localized WFs, various general and practical approaches have been recently proposed, targeting the construction of well-localized WFs using algorithms that are often non-iterative; this not only makes them more automatable, but also provides an excellent starting point for a final Wannierization, if required: the SCDM approach [59, 60, 104], the continuous Bloch gauges [105, 106], and the projectability disentanglement and manifold remixing approaches [61, 62].

SCDM is based on QR factorization with column pivoting (QRCP) of the reduced single-particle density matrix. The approach can be used either to produce well-localized WFs without performing an iterative minimization, or it can be considered a linear-algebra method to identify a good starting point for a MLWF procedure. The SCDM method is implemented [107] in the interface code to `Quantum ESPRESSO`, with an algorithm for the QRCP factorization that works on a smaller matrix instead of the full density matrix [59, 60, 104]. For a set of composite

bands, SCDM is parameter-free. A comprehensive study on 81 insulators [107] has shown how the MLWF procedure applied to SCDM initial projections (SCDM+MLWF) improves the interpolation accuracy and localization of the resulting WFs, although SCDM-only WFs perform already remarkably well, both in terms of accuracy of band structure interpolation and in terms of localization. In the case of entangled bands, SCDM requires to specify an energy-window function, its center and width, as well as the number of WFs to consider. [107] introduced a recipe to automatically select those parameters (more details in Sec. 3.10), which was tested on 200 bulk materials. Unlike in the case of isolated groups of bands, for entangled bands the SCDM+MLWF method greatly improved the localization of the WFs with respect to SCDM-only. Notably, however, the reduced spread induced by the MV procedure might result in lower band-interpolation accuracy. Although the SCDM projections could be used together with the SMV disentanglement scheme, this more complex procedure does not provide systematic gain in accuracy, such that a SCDM-only or SCDM+MLWF (with MV minimization for $\tilde{\Omega}$) is recommended [107]. In addition, we note that SCDM requires real-space wavefunctions as input, and therefore has a higher computational and memory cost with respect to other methods discussed later in this section, which are implemented in reciprocal space.

Another non-iterative approach for composite bands is based on ensuring a continuous Bloch gauge over the entire BZ [105, 106], resulting in good localization properties of the WFs and not requiring any chemical intuition for their construction. The main idea is that one can construct a sequence of gauge matrices that are not only continuous across the BZ but also satisfy its periodicity at the BZ edges. This is achieved by first adopting parallel transport for the gauge matrix, starting from a chosen k point (usually the Γ point) and propagating along a line (e.g. the k_x line). This enables the periodicity to be fixed at the two end points of the line, while preserving the continuity. Then, for each k point on the line, parallel transport is applied to each of the gauge matrices along an orthogonal direction (e.g. in the k_y direction), and all gauge matrices are fixed again at the endpoints, to ensure periodicity of the 2D plane. Finally, for each k point on the 2D plane, one can apply a similar procedure to construct gauge matrices along the third direction, therefore obtaining a global continuous gauge across the full BZ. Often, the resulting gauge is continuous but not smooth enough: a subsequent conventional MV iterative minimization can improve the localization and reach the MLWF gauge. Such algorithm is able to construct MLWFs for difficult cases such as $\mathbb{Z}_2$ topological insulators [106].

Lastly, a very robust approach has emerged in the form of projectability disentanglement [61], where the inner and outer energy windows are replaced by projectability thresholds. For each state $|u_{n\mathbf{k}}\rangle$, a projectability [107, 108] onto localized atomic orbitals (typically, those coming from the pseudopotentials) is calculated. Then, states that have very high projectability are retained identically (exactly as done for states inside the inner frozen window in the SMV method); states that have low projectability are discarded altogether (since they do not provide useful contributions to MLWFs); and states that span the intermediate projectability values are treated with the standard SMV disentanglement. This approach leads naturally and robustly to atomic-like projectability-disentangled Wannier functions (PDWFs), spanning both occupied and unoccupied states corresponding to Bloch sums of bonding/anti-bonding combinations of atomic orbitals.

These PDWFs can in turn be remixed into linear combinations that aim to describe target

submanifolds; e.g., the valence states only, the conduction states only, or certain groups of bands that are separated in energy from the rest. This may be beneficial for finding optimal target states for beyond-DFT methods (see Sec. 3.8).

This remixing is particularly valuable for Koopmans functionals (see Sec. 3.8.2), which require separate sets of MLWFs for the valence and conduction manifolds, or for transport calculations. For this purpose, the manifold-remixed Wannier functions (MRWFs) [62] are obtained by starting from the PDWFs spanning the whole manifold (valence plus conduction), which is then split by rotating the gauge matrices into a block-diagonal structure across all the k points, while simultaneously maintaining the gauge smoothness for each block. This is achieved by a combination of automated Wannierization of the whole manifold, diagonalization of the Wannier Hamiltonian, parallel transport, and maximal localization. The automated Wannierization of the whole manifold can be obtained using the PDWF method; the Hamiltonian diagonalization splits the manifold into desired submanifolds (e.g., two for valence and conduction, respectively); the parallel transport fixes the gauge randomness to construct two sets of localized WFs; the final maximal localization smoothens the gauge, leading to subsets of MLWFs for the respective submanifolds. [62] demonstrates that, when combined with PDWFs, the MRWF method can be fully automated, and can also be extended to other types of band manifolds gapped in energy, such as the single top valence band of MoS_2, or the $3d$ and t_{2g}/e_g submanifolds of $SrVO_3$. For high-throughput results of PDWF and MRWF, see Sec. 3.10.

3 The Wannier ecosystem: theory and software packages

3.1 Development of widely available Wannier engines

The MV and SMV methods described in [4, 11] were originally implemented in Fortran 77. The code would compute the overlaps in Eq. (12) and the projection of the periodic part of the Bloch orbitals onto trial localized states, by reading the former evaluated on a regular k-point grid by a DFT code—originally by an early version of `CASTEP` [109, 110]. To provide a more general model, driven by the need to interface with a DFT code based on the LAPW method [84], the choice was made to keep the calculation of all the scalar products involving Bloch orbitals needed by the Wannier code within the electronic-structure code of choice, typically as a postprocessing step. Well-defined protocols were established to exchange this information writing/reading files to/from disk and the format of those files fully documented. The resulting `Wannier77` code was released under a GPL v2 license in March 2004.

In 2005, two of the current authors (AAM and JRY), then working in the groups of NM and IS respectively, rewrote the routines using modern modular Fortran, relying on their experience of software development gained from working on the `ONETEP` [111] and `CASTEP` [110] DFT programs. The resulting program, `Wannier90` [83], was released under a GPL license in April 2006. Following the early layout in the `Wannier77` code, `Wannier90` was designed to be easily interfaced to any electronic-structure code, irrespective of its underlying basis set. The first release of `Wannier90` came with extensive documentation, tutorials, and two validation tests. Development used CVS as a version control system. GP joined the development effort in 2012,

and a new parallel post-processing code (`postw90`) was developed and released in `Wannier90` version 2 [112] in October 2013.

While the development of `Wannier90` as an open-source interoperable code was innovative in 2006, by 2016 it was clear that the development tools being used did not make use of what was then considered best practice. For example, having only a few developers with access to the main repository presented a barrier to adding new functionality to the program. A decision was made to move to a community development model, and the `Wannier90` repository was migrated to GitHub with the adoption of a "fork and pull request" approach. This new model was launched with a community developer workshop held in San Sebastián in September of 2016. This event is clearly recognizable in Fig. 6, which shows the number of commits to the code repository over time, with a large number of commits contributed during (or immediately after) the 2016 event. Moreover, once the code made its transition to a community development model, the rate of commits significantly increased, as well as the number of individual contributors (over 35 different people had contributed code, tests or documentation via commits by the end of 2022). Essential to this change was the development of an extensive suite of tests, which run automatically to validate each pull request. In 2019, `Wannier90` version 3 was released, including all community contributions to the code [96].

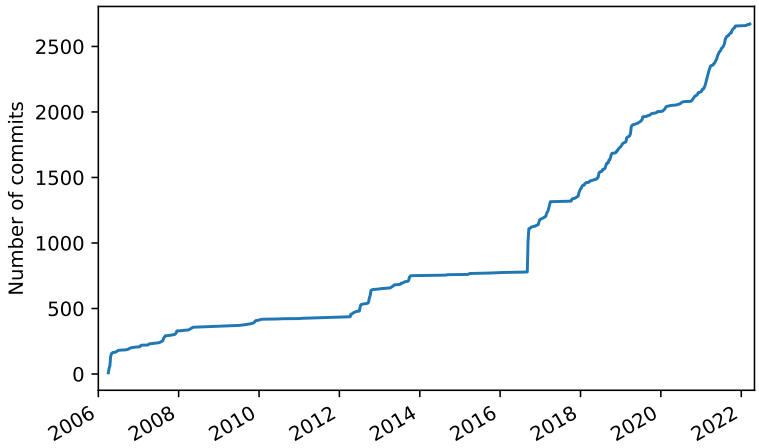

Figure 6: Total number of commits over time for the `Wannier90` repository (CVS until August 2016, then transferred to Git and hosted on GitHub). Note the significant increase during and immediately after the community developer workshop in September 2016.

In addition to `Wannier90`, there are a few electronic-structure software packages that nowadays implement internal functionality for computing WFs in periodic systems. These include `GPAW` [113], `QBOX` [114], `CP2K` [115], `exciting` [102], `OpenMX` [116], `RESPACK` [117] and `CRYSTAL` [118]. However, in this review we want to use the term "Wannier engines" to describe software packages that generate WFs *and* are designed to be used interoperably with other software packages: e.g., with the electronic-structure codes for solving the electronic ground state, used as input to a Wannier engine, and with post-processing codes that use the WFs from a Wannier engine to calculate advanced electronic properties. `Wannier90` is clearly an example of a Wannier engine, but it is not the only readily available one—another notable example is the `Atomic Simulation`

`Environment (ASE)` [119], which also implements routines based on the minimization of the quadratic spread of the WFs, but uses a different approach [56, 57] to that described above (see also Sec. 2.4). In addition, the recent `Wannier.jl` package [120] implements several Wannierization algorithms using manifold optimization techniques, and brings the methodology of WFs to the Julia [121] community. In this review, we focus on those codes that interface to the `Wannier90` code; nevertheless, we note that often the other Wannier engines have adopted the same file formats first defined by `Wannier77`/`Wannier90` (see discussion in Sec. 3.2), thus being fully compatible with the ecosystem.

3.2 The concept of a Wannier function software ecosystem

To discuss the modular approach that has catalyzed the formation of a Wannier function software ecosystem, we start with a brief and general overview of modularization strategies in software programs. We also mention some related efforts on code modularization, discussing the aspects that apply to the Wannier ecosystem. Complex software can adopt a variety of architecture design approaches, often differing substantially in the level of modularity (or lack thereof) of their components. Historically, most computer programs started as monolithic applications: self-contained and independent codes made of tightly coupled functions. This is a natural choice when writing new software from scratch, and it reduces the installation burden for users, who do not need to deal with the management of many dependencies. Over time, however, features and post-processing tools tend to get added, making the codebase very large and complex. This results in serious challenges for development and maintenance, which become critical when the code needs to be adapted and optimized for newer hardware architectures. Furthermore, this leads to reimplementation of common routines in each code, which could instead be written and optimized only once, and then used as a library. The library approach is already common in the electronic-structure community for linear-algebra and diagonalization routines, where the code calls functions via standard interfaces defined by the BLAS [122] and LAPACK [123] libraries, and the executables are linked to performance-optimized versions on high-performance computing (HPC) clusters. While a similar approach is often used for other low-level routines, such as fast-Fourier-transform (FFT) computation [124] or to support file formats such as netCDF [125] or HDF5 [126], it was until recently far less common for higher-level materials-science-oriented routines.

To address the challenges of monolithic codes, many electronic-structure codes are being redesigned or rewritten using a more modular approach, where core modules are—when possible—generalized and separated into a library of reusable routines, then called by higher-level functions to execute complex tasks. Some of these codes have evolved into distributions, i.e., a set of relatively independent but interoperable executables reusing common core routines. However, even with this approach, the different modules can often operate only within the distribution, and the development of all modules needs to be constantly in sync.

Ultimate interoperability is obtained when code (such as core routines or full functionality) is reused by different independent software distributions, maintained by non-overlapping developer groups. A crucial challenge to enable such a level of interoperability is to design a clear application programming interface (API) defining which data needs to be transferred between

codes, and in which format. This requires discussions and coordination, which can be catalyzed via targeted coordination efforts.

We stress that most of these challenges related to code modularization and interoperability are not specific to materials simulations and have been discussed since the early days of scientific computing [127]. In the field of electronic structure, an example worth mentioning is the CE-CAM Electronic Structure Library project [128]. At an even higher level, one can address code interoperability by defining common interfaces (e.g., input/output schemes) for workflows computing a quantity of interest, independent of the underlying simulation code, such as the common workflow interface of [129] to perform crystal-structure relaxation and to compute equations of state. The workflow only requires as input, in a common format, the crystal structure and a few basic input parameters, and is then interfaced with 11 different DFT codes to run the actual simulations. Such universal interfaces make workflows accessible to a broader audience and codes fully interoperable, allowing researchers to switch between them without the need to learn from scratch the details of each one. In addition, they can be seamlessly applied to perform cross-code verification studies [130].

When codes have to exchange data, the interfaces between them can be actual code APIs (e.g., in C or Fortran), where the library is directly compiled and linked with the main code, but also simply files in a well-documented format, written by the first application and read by the second one (see also later discussion of this approach in Sec. 3.9). The actual choice depends on the interdependency between the algorithmic steps and on performance considerations. The use of files is typically favored when the corresponding simulation workflows imply a sequential execution of codes rather than interconnected loops between them, when the exchanged data is small (up to few GB), and when the individual steps are computationally demanding, so that I/O overhead is only a small fraction of the total execution time. (In a few advanced cases, other interfaces such as network sockets have been used to keep the applications decoupled while still reducing the I/O overhead for simulations that are not very computationally demanding [131].) In addition, by writing intermediate results to files, the steps do not need to be combined in the same run, but can be executed at differed points in time (e.g., days later) or by different researchers.

In this context, WFs happen to represent a remarkable and elegant method to decouple the *ab initio* simulation of the electronic structure from the calculation of the physical properties. This is possible thanks to two core aspects of WFs. First, WFs are independent of the basis set used in the first-principles electronic-structure code: the MLWF algorithm requires the sole knowledge of a handful of vectors and matrices, such as the overlap matrices on a coarse grid of k points. Wavefunctions, typically stored in very large files, are not required during Wannierization, but only used optionally in few post-processing steps, e.g., when representing the WFs on a real-space grid. Second, many physical quantities can be obtained efficiently once a WF basis is constructed, only with the knowledge of relevant operators represented as small matrices directly in the Wannier basis, such as the Hamiltonian or the position operator. Indeed, while extended basis sets such as plane waves are particularly convenient to obtain charge densities and wavefunctions of periodic systems, reciprocal space integrals can be more efficiently calculated using a Fourier-interpolated basis set, originating from a compact maximally localized representation in real space. From a computer-science perspective, we can say that these two

aspects of the Wannierization process make it an effective data-compression encoding, avoiding the need to transfer large wavefunctions between the *ab initio* codes and the property calculators, while retaining an equivalent level of accuracy.

Thanks to the first aspect, i.e., basis-set independence, the Wannier code [4] evolved from being a standalone code focused on the minimization procedure to one with a well-defined format for the input data (overlap and projection matrices), which also defined and documented the corresponding files (e.g., for the overlap matrices in `.mmn` format and the projection matrices in `.amn` format). The calculation of the latter was delegated to specific interfaces implemented within the corresponding first-principles packages [84]. This design persisted in the `Wannier90` code [83, 96] and as a result the `Wannier90` engine can now be interfaced with virtually any electronic-structure code as already discussed in Sec. 3.1, with interfaces currently available for many widespread codes, including `ABINIT` [132], `BigDFT` [133], `Elk` [134], `FLEUR` [135], `GPAW` [113], `Octopus` [136], `OpenMX` [137], `pySCF` [138, 139], `Quantum ESPRESSO` [54, 55], `SIESTA` [140], `VASP` [141] and `WIEN2k` [142].

Because of the second aspect, i.e., the possibility of efficiently obtaining many physical quantities in the Wannier basis, `Wannier90` started to include a large number of efficient post-processing utilities for materials properties, ranging from simple band-structure interpolation to more complex properties such as the ordinary and anomalous Hall conductivities, Seebeck coefficients, orbital magnetization, and many more [96]. However, in the last decade the community has spontaneously moved towards a decentralized software ecosystem (as opposed to a centralized, albeit modular, Wannier distribution), where different packages interact through APIs and a common data format. The decentralized model was again facilitated by a clear and documented interface to generate data as input to the next steps (e.g., the `_tb.dat` file containing the full TB model: WF centers, on-site energies, and hopping energies). The community has been rapidly growing, and several independent packages exploiting MLWFs exist nowadays, targeting diverse properties such as TB models (Sec. 3.3), ballistic transport (Sec. 3.4), Berry-phase related properties (Sec. 3.5), topological invariants (Sec. 3.6), electron-phonon coupling (Sec. 3.7), beyond-DFT methods (Sec. 3.8), high-throughput calculations (Sec. 3.10), and more.

This review article describes such a community of symbiotic packages, forming a research and software ecosystem built upon the concept of MLWFs. We illustrate this schematically in Fig. 5. To make the codes of the ecosystem as easy to find as possible, we also started in 2024 an online Wannier Software Ecosystem Registry [143]. Such a registry lists software packages that form the ecosystem, and as of May 2024 it already includes 53 entries. The repository provides key information including a short description, a domain tag (e.g., "Ab initio engines", "Tight-binding", "Berryology and topology") and links to the code homepage, documentation and source code (if available). The registry is dynamic: developers and users can add new entries or modify existing ones by submitting a pull request through the corresponding GitHub repository [144], which also includes detailed instructions for contribution.

3.3 Wannier interpolation and tight-binding models

A very common application of WFs is to evaluate various k-space quantities and BZ integrals by "Wannier interpolation". This name has come to refer to a type of Slater–Koster interpolation

where the required on-site and hopping integrals are calculated explicitly in the WF basis [11–13, 31], as opposed to being treated as fitting parameters as done in empirical TB theory. Here we review the basic procedure as it applies to energy bands and other simple quantities, leaving more sophisticated applications to later sections. Before proceeding, let us mention that the Wannier interpolation scheme has been adapted to work with non-orthogonal localized orbitals instead of (orthogonal) WFs [145–148].

3.3.1 Band interpolation

To interpolate the band structure, one needs the matrix elements of the KS Hamiltonian in the WF basis,

$$H_{ij}^{\mathrm{W}}(\mathbf{R}) = \langle \mathbf{0}i|\hat{H}|\mathbf{R}j\rangle; \tag{15}$$

here $H_{ii}(\mathbf{0})$ are on-site energies, and the remaining matrix elements are hoppings. One way to evaluate these matrix elements is to start from Eq. (6a) for the WFs in terms of the KS Bloch eigenstates on the *ab initio* k-grid. Inserting that expression in Eq. (15) gives

$$H_{ij}^{\mathrm{W}}(\mathbf{R}) = \frac{1}{N}\sum_{\mathbf{k}} e^{-i\mathbf{k}\cdot\mathbf{R}} \sum_{n=1}^{\mathcal{J}_{\mathbf{k}}} V_{\mathbf{k},ni}^{*}\varepsilon_{n\mathbf{k}}V_{\mathbf{k},nj}. \tag{16}$$

This procedure is particularly convenient in the framework of the MV and SMV Wannierization schemes, which are formulated as post-processing steps after a conventional *ab initio* calculation is carried out on a uniform $\{\mathbf{k}\}$ grid; Eq. (16) only involves the $V_{\mathbf{k}}$ matrices generated by the Wannier engine starting from the *ab initio* overlap matrices and the energy eigenvalues themselves (see Sec. 2.1). An alternative to Eq. (16) would be to express the WFs in a real-space basis, e.g., localized orbitals or a grid, and then evaluate Eq. (15) directly on that basis.

In view of the localized character of the WFs, $|H_{ij}^{\mathrm{W}}(\mathbf{R})|$ is expected to become negligibly small when the distance $|\mathbf{R}+\boldsymbol{\tau}_j-\boldsymbol{\tau}_i|$ between the centers of the two WFs becomes sufficiently large (here, $\boldsymbol{\tau}_j = \langle \mathbf{0}j|\hat{\mathbf{r}}|\mathbf{0}j\rangle$). However, due to the finite size N of the *ab initio* grid, the WFs obtained from Eq. (6a) are actually periodic over a real-space supercell of volume NV_{cell}; accordingly, the matrix elements given by Eq. (16) are also supercell-periodic: $H_{ij}^{\mathrm{W}}(\mathbf{R}+\mathbf{T}) = H_{ij}^{\mathrm{W}}(\mathbf{R})$, for any supercell lattice vector $\mathbf{T}$. To minimize spurious effects associated with this artificial periodicity, the hopping matrix should be truncated by setting $H_{ij}^{\mathrm{W}}(\mathbf{R}) = 0$ whenever the vector $\mathbf{R}+\mathbf{T}+\boldsymbol{\tau}_j$ lies outside the Wigner–Seitz (WS) supercell centered at the origin. Provided that this supercell is sufficiently large to ensure negligible overlap between a WF and its periodic images, the truncation error will be insignificant. This means that in practice one can achieve well-converged numerical results with a relatively coarse *ab initio* grid. Note, however, that the matrix elements do not decay exactly to zero for finite-size WS supercells. Therefore, when multiple $\mathbf{R}$ vectors lie on the boundary of the WS supercell and are connected by a supercell vector $\mathbf{T}$, it is better to consider all these equivalent vectors with appropriate weights, rather than picking only one of them, which would introduce spurious symmetry breaking in the Hamiltonian. The details of this approach and its implementation in `Wannier90` are discussed in Sec. 4.2 of [96].

Once the on-site energies and hoppings have been tabulated, the Hamiltonian matrix is inter-

polated onto an arbitrary BZ point $\mathbf{k}'$ by performing an inverse Fourier transform,

$$H^{\mathrm{W}}_{\mathbf{k}',ij} = \sum_{\mathbf{R}}^{\mathrm{WS}} \frac{1}{\mathcal{N}_{\mathbf{R},ij}} \sum_{l=1}^{\mathcal{N}_{\mathbf{R},ij}} e^{i\mathbf{k}'\cdot(\mathbf{R}+\mathbf{T}^l_{\mathbf{R},ij})} H^{\mathrm{W}}_{ij}(\mathbf{R})\,. \tag{17}$$

The summation runs over the lattice vectors $\mathbf{R}$ (which lie in the WS supercell centered at the origin. as discussed above) with $\mathcal{N}_{\mathbf{R}} > 1$ whenever $\mathbf{R} + \mathbf{T}^l_{\mathbf{R},ij} + \boldsymbol{\tau}_j$ falls on the boundary of the WS supercell centered at $\boldsymbol{\tau}_i$. To improve the quality of the interpolation, for each combination of i, j, and $\mathbf{R}$ the supercell lattice vector $\mathbf{T}$ appearing in Eq. (17) is chosen as the one that minimizes $|\mathbf{R} + \mathbf{T} + \boldsymbol{\tau}_j - \boldsymbol{\tau}_i|$ [96]. Finally, the interpolated energy eigenvalues are obtained by diagonalizing the above matrix,

$$\left[\mathcal{U}^{\dagger}_{\mathbf{k}'} H^{\mathrm{W}}_{\mathbf{k}'} \mathcal{U}_{\mathbf{k}'}\right]_{mn} = \delta_{mn} \varepsilon^{\mathrm{H}}_{n\mathbf{k}'}\,, \tag{18}$$

so that the column vectors of the unitary matrix $\mathcal{U}_{\mathbf{k}'}$ are eigenvectors of $H^{\mathrm{W}}_{\mathbf{k}'}$.

Since the interpolation steps (17) and (18) only involve Fourier transforming and diagonalizing $J \times J$ matrices that are typically small, the overall procedure tends to be much less expensive than a direct DFT calculation at every interpolation point, especially when a dense interpolation grid $\{\mathbf{k}'\}$ is needed. The efficient evaluation of the Hamiltonian matrix and band derivatives (see below) enables BZ integration methods beyond the standard equispaced scheme to be explored. These are of particular use when fine features in k space need to be resolved using adaptive integration methods [149–151].

The above interpolation scheme has been shown to accurately reproduce—within the frozen energy window—the energy eigenvalues obtained by a direct DFT calculation. As an example, we show in Fig. 7 a detail of the interpolated band structure of ferromagnetic body-centred cubic (BCC) Fe along the H–Γ line [13]. The vertical gray lines indicate points on the $\{\mathbf{k}\}$ mesh

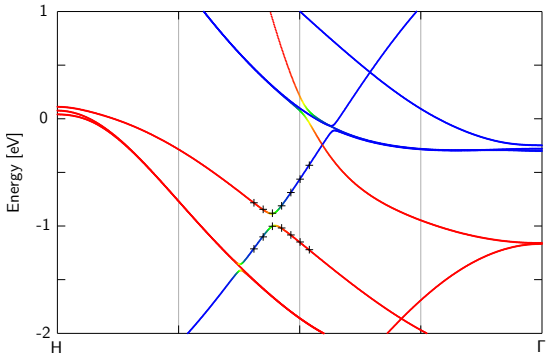

Figure 7: Wannier-interpolated bands of BCC Fe along the H–Γ line. The bands are color-coded according to the value of the spin expectation value $\langle\psi_{n\mathbf{k}}|\hat{S}_z|\psi_{n\mathbf{k}}\rangle$: red for spin up, and blue for spin down. The energies are given in eV, and the Fermi level is at 0 eV. The vertical gray lines indicate k points on the *ab initio* mesh used for constructing the WFs.

used for constructing the WFs. For comparison, we plot as plus symbols the *ab initio* dispersion around a weak spin-orbit-induced avoided crossing between two bands of opposite spin. It is apparent that the Wannier interpolation procedure succeeds in resolving details on a scale much smaller than the spacing between those points. In particular, the correct band connectivity is obtained, so that avoided crossings, no matter how weak, are not mistaken for actual crossings. This characteristic, which distinguishes Wannier interpolation from methods based on direct

Fourier interpolation of the energy eigenvalues [152, 153], makes it a powerful tool for studying topological properties (Sec. 3.6), and for evaluating BZ integrals involving quantities that change rapidly over small regions of k space, such as the Berry curvature (Sec. 3.5) and electron-phonon matrix elements (Sec. 3.7).

Wannier interpolation works for the same reason that empirical TB does: the short range of the real-space Hamiltonian matrix (16) ensures that its Fourier transform (17) is a smooth function in reciprocal space. This can also be seen by writing the left-hand side of Eq. (17) as

$$H^{\mathrm{W}}_{\mathbf{k}',ij} = \langle \psi^{\mathrm{W}}_{i\mathbf{k}'} | \hat{H} | \psi^{\mathrm{W}}_{j\mathbf{k}'} \rangle \,, \tag{19}$$

where

$$|\psi^{\mathrm{W}}_{j\mathbf{k}'}\rangle = \sum_{\mathbf{R}} e^{i\mathbf{k}'\cdot\mathbf{R}} \, |\mathbf{R}j\rangle \tag{20}$$

interpolates the smooth Bloch functions defined on the *ab initio* grid by Eq. (6b). We may also write the left-hand side of Eq. (18) as

$$H^{\mathrm{H}}_{\mathbf{k}',mn} = \langle \psi^{\mathrm{H}}_{m\mathbf{k}'} | \hat{H} | \psi^{\mathrm{H}}_{n\mathbf{k}'} \rangle \,, \tag{21}$$

where

$$|\psi^{\mathrm{H}}_{n\mathbf{k}'}\rangle = \sum_{j=1}^{J} |\psi^{\mathrm{W}}_{j\mathbf{k}'}\rangle \, \mathcal{U}_{\mathbf{k}',jn} \tag{22}$$

describes a unitary transformation from the Wannier gauge W to the Hamiltonian gauge H. Inside the frozen energy window, the states $|\psi^{\mathrm{H}}_{n\mathbf{k}'}\rangle$ interpolate—up to arbitrary phase factors—the *ab initio* eigenstates $|\psi_{n\mathbf{k}}\rangle$.

In summary, performing Fourier interpolation in the W gauge followed by a unitary transformation to the H gauge allows interpolating quantities—band energies, Bloch eigenstates, and matrix elements thereof (see below)—that can vary rapidly in k space, and even become non-analytic at degeneracies. This strategy retains the accuracy of a full-blown *ab initio* calculation, while benefiting from the efficiency of Slater–Koster interpolation.

3.3.2 Band derivatives and Boltzmann transport

The interpolation procedure outlined above can be adapted to evaluate band velocities, inverse effective-mass tensors, and higher k-derivatives of the energy eigenvalues [13]; as in the empirical TB method [154], this is achieved without relying on finite-difference methods, which become problematic in the vicinity of band crossings and weak avoided crossings, where the band ordering can change from one grid point to the next.

Band derivatives are needed, for instance, to evaluate transport coefficients such as the electrical conductivity σ, the Seebeck coefficient S, or the electronic contribution to the thermal conductivity K. Within the semiclassical Boltzmann transport equation (BTE) framework, one defines a scattering time $\tau_{n\mathbf{k}}$ for an electron on band n at wavevector $\mathbf{k}$ (incidentally, the contributions from electron–phonon scattering to $\tau_{n\mathbf{k}}$ can be efficiently computed exploiting Wannier

functions, see Sec. 3.7). Then, the expressions for the transport tensors are given by [155]:

$$\sigma_{ab}(\mu,T) = e^2 \int_{-\infty}^{+\infty} dE \left(-\frac{\partial f(E,\mu,T)}{\partial E}\right) \Sigma_{ab}(E), \tag{23}$$

$$[\sigma S]_{ab}(\mu,T) = \frac{e}{T} \int_{-\infty}^{+\infty} dE \left(-\frac{\partial f(E,\mu,T)}{\partial E}\right) (E-\mu)\Sigma_{ab}(E), \tag{24}$$

$$K_{ab}(\mu,T) = \frac{1}{T} \int_{-\infty}^{+\infty} dE \left(-\frac{\partial f(E,\mu,T)}{\partial E}\right) (E-\mu)^2\Sigma_{ab}(E), \tag{25}$$

where μ is the chemical potential, T is the temperature, a and b are Cartesian indices, σS denotes the matrix product of the two tensors, $\partial f/\partial E$ is the derivative of the Fermi–Dirac distribution function with respect to the energy, and $\Sigma_{ab}(E)$ is the transport distribution function. The latter is defined by

$$\Sigma_{ab}(E) = \frac{1}{V_{\text{cell}}} \sum_{n\mathbf{k}} v^a_{n\mathbf{k}} v^b_{n\mathbf{k}} \tau_{n\mathbf{k}} \delta(E - E_{n\mathbf{k}}), \tag{26}$$

where the summation is over all bands n and over all the BZ, $\varepsilon_{n\mathbf{k}}$ is the energy for band n at $\mathbf{k}$ and $v^a_{n\mathbf{k}}$ is the a component of the band velocity at $(n,\mathbf{k})$.

Obtaining converged quantities for Eqs.(23)–(25), therefore, requires to compute the band derivatives $\mathbf{v}_{n\mathbf{k}}$ while sampling the BZ over dense k-point grids [152, 156, 157], since the term $\partial f/\partial E$ is non-zero only in a narrow energy region (of typical size k_BT, where k_B is the Boltzmann constant) around the chemical potential μ. Wannier interpolation allows carrying out this task efficiently and accurately even when (avoided) crossings occur close to the Fermi level: band derivatives at a given k point are obtained with an analytical expression, without resorting to finite-difference methods [13]. Moreover, computation on dense k-point grids is very efficient, as already discussed earlier for band interpolation. This WF-based Boltzmann-transport methodology is implemented in `Wannier90` and used to compute transport tensors in its `BoltzWann` module [158], as well as in other codes (see, e.g., the electron-phonon section, Sec. 3.7), and is also used for post-processing calculations in many-body theory (see Sec. 3.8.1).

Furthermore, many transport coefficients (e.g., linear and non-linear (AHCs) [159, 160], anomalous Nernst thermoelectric conductivity [161], magnetoresistance [162], and magnetochiral anisotropy [163]) depend on the Berry curvature and other quantum-geometric quantities [10, 164, 165]. As they involve k-derivatives of the Bloch states themselves, such quantities cannot be obtained from the energy dispersions. Moreover, those quantities tend to become strongly enhanced when weak avoided crossings occur near the Fermi level; when that happens, very dense k-point grids must be employed to converge the calculation [159]. Compared to band interpolation, the interpolation of Berry-type quantities is more involved because it requires setting up matrix elements of the position operator $\hat{\mathbf{r}}$, which is non-local in reciprocal space, i.e., not lattice periodic [16]. We defer a discussion of that case to Sec. 3.5, and below we describe how to interpolate the matrix elements of a generic lattice-periodic operator $\hat{X}$.

3.3.3 Interpolation of a generic lattice-periodic operator

Replacing $\hat{H} \to \hat{X}$ in Eq. (15) and using Eq. (6) yield

$$X^{\text{W}}_{ij}(\mathbf{R}) = \frac{1}{N} \sum_{\mathbf{k}} e^{-i\mathbf{k}\cdot\mathbf{R}} \sum_{m,n=1}^{\mathcal{J}_{\mathbf{k}}} V^*_{\mathbf{k},mi} \langle \psi_{m\mathbf{k}} | \hat{X} | \psi_{n\mathbf{k}} \rangle V_{\mathbf{k},nj}\,, \tag{27}$$

which reduces to Eq. (16) for $\hat{X} = \hat{H}$. The considerations made earlier regarding the spatial decay and truncation of the $H^{\mathrm{W}}(\mathbf{R})$ matrix apply equally well to $X^{\mathrm{W}}(\mathbf{R})$. The Fourier-transform step is also analogous to Eq. (17),

$$X^{\mathrm{W}}_{\mathbf{k}',ij} = \sum_{\mathbf{R}} e^{i\mathbf{k}'\cdot\mathbf{R}} X^{\mathrm{W}}_{ij}(\mathbf{R}) = \langle \psi^{\mathrm{W}}_{i\mathbf{k}'} | \hat{X} | \psi^{\mathrm{W}}_{j\mathbf{k}'} \rangle \,, \tag{28}$$

and the final step is to apply to $X^{\mathrm{W}}_{\mathbf{k}'}$ the same unitary transformation that was used in Eq. (18) to diagonalize $H^{\mathrm{W}}_{\mathbf{k}'}$. Using Eq. (22), we find

$$X^{\mathrm{H}}_{\mathbf{k}',mn} = \left(\mathcal{U}^{\dagger}_{\mathbf{k}'} X^{\mathrm{W}}_{\mathbf{k}'} \mathcal{U}_{\mathbf{k}'} \right)_{mn} = \langle \psi^{\mathrm{H}}_{m\mathbf{k}'} | \hat{X} | \psi^{\mathrm{H}}_{n\mathbf{k}'} \rangle \,. \tag{29}$$

In particular, diagonal elements of $X^{\mathrm{H}}_{\mathbf{k}'}$ give the expectation values of $\hat{X}$ in the interpolated states. With $\hat{X} = \hat{\mathbf{S}}$, for example, one obtains their spin polarization, which is how the color-coding in Fig. 7 was generated.

Note that in addition to the overlap matrices and energy eigenvalues, interpolating a generic operator $\hat{X} \neq \hat{H}$ requires setting up its matrix elements $\langle \psi_{m\mathbf{k}} | \hat{X} | \psi_{n\mathbf{k}} \rangle$ on the *ab initio* grid; this should be done by the same interface code that computes the overlap matrices.

3.3.4 Wannier function perturbation theory

Several important materials properties can be calculated as the linear response of the system to an external perturbation $\hat{V}$. A common example is the calculation of phonon dispersions and electron-phonon coupling through density-functional perturbation theory (DFPT) [166], the latter case is discussed in Sec. 3.7.

We follow [167], and write the Hamiltonian eigenstates of the perturbed system in terms of the ones of the unperturbed system plus the wavefunction perturbation,

$$|\psi_{n\mathbf{k}}\rangle = |\psi_{n\mathbf{k}}\rangle^{(0)} + \lambda \, |\psi_{n\mathbf{k}}\rangle^{(1)} + \mathcal{O}(\lambda^2) \,, \tag{30}$$

where the wavefunction perturbation can be calculated with a sum over empty states,

$$|\psi_{n\mathbf{k}}\rangle^{(1)} = \sum_{n'\mathbf{k}'}{}' \, |\psi_{n'\mathbf{k}'}\rangle^{(0)} \, \frac{\langle \psi_{n'\mathbf{k}'} | \hat{V} | \psi_{n\mathbf{k}} \rangle^{(0)}}{\epsilon_{n\mathbf{k}} - \epsilon_{n'\mathbf{k}'}}. \tag{31}$$

The primed sum means that terms for which the denominator vanishes are excluded.

Alternatively, the wavefunction perturbation can be calculated without summing over high-energy states by solving the Sternheimer equation [166]. Lihm and Park [167] have shown that such perturbation theory can be formulated in the Wannier representation, where the WFs of the perturbed system can be written as

$$|\mathbf{R}j\rangle = |\mathbf{R}j\rangle^{(0)} + \lambda \, |\mathbf{R}j\rangle^{(1)} + \mathcal{O}(\lambda^2). \tag{32}$$

The expression for $|\mathbf{R}j\rangle^{(1)}$, reported in Eqs. (8) and (9) of [167], consists of two terms: the first can be calculated with the Sternheimer equation to obtain the states $|\psi_{n\mathbf{k}}\rangle^{(1)}$, while the second contains matrix elements of $\hat{V}$ and the projector over the WFs of the unperturbed system. Crucially, both terms only require energies and matrix elements within the Wannier outer window

introduced in Sec. 2.1.2. Thus, the Wannier function perturbation can be calculated without making explicit use of the states outside that energy window.

For a monochromatic static perturbation with wavevector $\mathbf{q}$, the first-order wavefunction perturbation can be interpolated as [167]

$$\begin{aligned} |\psi^{\mathrm{H}}_{n\mathbf{k}',\mathbf{q}}\rangle^{(1)} &= \frac{1}{\sqrt{N}} \sum_{j,\mathbf{R}} e^{i\mathbf{k}'\cdot\mathbf{R}} \, |\mathbf{R}_{\mathbf{q}} j\rangle^{(1)} \, \mathcal{U}_{\mathbf{k}',jn} \\ &+ \sum_{m=1}^{N_W}{}' \, |\psi^{\mathrm{H}}_{m\mathbf{k}'+\mathbf{q}}\rangle^{(0)} \, \frac{\tilde{g}^{\mathrm{H}}_{mn\mathbf{k}',\mathbf{q}}}{\epsilon^{(0)}_{n\mathbf{k}'} - \epsilon^{(0)}_{m\mathbf{k}'+\mathbf{q}}}, \end{aligned} \tag{33}$$

where the WF perturbations are expanded as a sum of monochromatic perturbations

$$|\mathbf{R}j\rangle^{(1)} = \sum_{\mathbf{q}} |\mathbf{R}_{\mathbf{q}} j\rangle^{(1)} \tag{34}$$

while the superscript H marks the Hamiltonian gauge of the unperturbed (0) and perturbed (1) system, $\mathcal{U}_{\mathbf{k}'}$ is the unitary matrix that diagonalizes the unperturbed Hamiltonian according to Eq. (18), and $\tilde{g}^{\mathrm{H}}_{mn\mathbf{k},\mathbf{q}}$ is obtained by performing the Fourier transform of $\tilde{g}_{ij\mathbf{R},\mathbf{q}}$ and then rotating to the Hamiltonian gauge using $\mathcal{U}_{\mathbf{k}'}$. The quantity $\tilde{g}_{ij\mathbf{R},\mathbf{q}}$ is related to the perturbation and is made of two terms ($\tilde{g}_{ij\mathbf{R},\mathbf{q}} = g_{ij\mathbf{R},\mathbf{q}} + \delta g_{ij\mathbf{R},\mathbf{q}}$), the first accounts for the matrix elements of $\hat{V}$ between WFs of the unperturbed states

$$g_{ij\mathbf{R},\mathbf{q}} = \langle \mathbf{0} i^{(0)} | \hat{V}_{\mathbf{q}} | \mathbf{R} j^{(0)} \rangle \, , \tag{35}$$

while the second is a correction stemming from the change of the WFs

$$\delta g_{ij\mathbf{R},\mathbf{q}} = \langle \mathbf{0} i^{(0)} | \hat{H}^{(0)} | \mathbf{R}_{\mathbf{q}} j^{(1)} \rangle + \langle \mathbf{0}_{-\mathbf{q}} i^{(1)} | \hat{H}^{(0)} | \mathbf{R} j^{(0)} \rangle \, . \tag{36}$$

The correction term $\delta g_{ij\mathbf{R},\mathbf{q}}$ is not required for the scattering matrix elements, but it is relevant for the perturbed wave functions. A key aspect is that Wannier function perturbations are localized in real space, so the perturbed Hamiltonian and its eigenstates can be efficiently interpolated by considering coarse k-point grids. This permits the efficient interpolation of various matrix elements involving the wavefunction perturbation, such as in the case of electron-phonon self-energies and Kubo formulas. Wannier function perturbation theory (WFPT) has been applied to describe temperature-dependent electronic band structures and indirect optical absorption, shift spin currents and spin Hall conductivities [167]. WFPT has recently been made available in the EPW code version 5.8 [168].

3.3.5 Porting Wannier Hamiltonians to TB codes

In TB theory, two phase conventions are commonly used to perform the Fourier transforms from real to reciprocal space [10]: the one adopted in Eqs. (17), (20) and (28) ("original convention"), and the alternative one ("modified convention") where the phase factors in those equations are modified as

$$e^{i\mathbf{k}'\cdot\mathbf{R}} \rightarrow e^{i\mathbf{k}'\cdot(\mathbf{R}+\boldsymbol{\tau}_j-\boldsymbol{\tau}_i)} \, . \tag{37}$$

Although the interpolated eigenvalues $\varepsilon^{\mathrm{H}}_{n\mathbf{k}'}$ and matrix elements $X^{\mathrm{H}}_{\mathbf{k}',mn}$ come out the same with both conventions (as they should), the modified convention is more natural for the purpose of

evaluating quantities, such as Berry connections and curvatures, that are sensitive to the real-space embedding of the TB model via the position matrix elements $\langle \mathbf{0}i|\hat{\mathbf{r}}|\mathbf{R}j\rangle$ (see Sec. 3.5). This has to do with the fact that with the original convention, TB eigenvectors (the column vectors of $\mathcal{U}_{\mathbf{k}'}$) behave like full Bloch eigenstates $|\psi_{n\mathbf{k}'}\rangle$, whereas with the modified convention they behave like their cell-periodic parts $|u_{n\mathbf{k}'}\rangle$ [10]; and it is in terms of the latter that Berry-type quantities are most naturally expressed.

The modified phase convention is the one adopted in the TB codes `PythTB` [169] and `TBmodels` [170]; both are able to import the Wannier Hamiltonian $H^{\mathrm{W}}_{ij}(\mathbf{R})$, along with the Wannier centers $\{\boldsymbol{\tau}_j\}$, from the `seedname_tb.dat` file written by `Wannier90`. `PythTB` was originally written for pedagogical purposes, as part of a course on Berry phases in electronic-structure theory that was later turned into a textbook [10]. It is feature-rich but is not optimized for speed, as it was designed with TB toy models in mind (however, a high-performance implementation is available [171]). Instead, `TBmodels` has fewer post-processing functionalities, but it delivers critical speed-up and improved scaling. Among other Wannier-TB codes, it is worth mentioning `Wannier Tools` [172], which implements sparse Hamiltonians for large systems, band unfolding, and several other features related to Berry-type quantities (see Sec. 3.5).

3.3.6 Wannier interpolation beyond density-functional theory

As discussed above, one of the most powerful and effective applications of WFs is the interpolation of band structures and other electronic-structure properties. While this is already very useful in the context of DFT calculations, it becomes even more compelling for beyond-DFT methods, such as hybrid functionals [36, 173–178], many-body perturbation theory (MBPT) such as G_0W_0 [179], and non-diagrammatic approaches such as the Koopmans-compliant functionals [180–189]. In fact, in DFT the potential can always be recalculated from the sole knowledge of the ground-state electronic charge density; therefore, the corresponding KS Hamiltonian can be directly calculated at any arbitrary $\mathbf{k}$-point. Instead, for most beyond-DFT methods this is no longer the case, and band structure calculations on a high-symmetry path cannot be performed as a series of independent diagonalizations. For hybrid functionals and GW, the eigenvalues at a given $\mathbf{k}$-point requires the knowledge of the wavefunctions and eigenenergies on all $(\mathbf{k}+\mathbf{q})$-points, where the $\mathbf{q}$-points are defined on a uniform grid which has to be converged. In other words, reasonably dense sampling on high-symmetry paths can only be obtained with some form of interpolation.

While electronic-structure codes typically offer general-purpose interpolation methods, often based on Fourier series [190, 191], WFs provide two concrete advantages. First, they are a physically motivated basis set, which exhibits exponential convergence and is guaranteed to deliver the exact result for a sufficiently dense $\mathbf{k}$-point grid, so the accuracy can be systematically increased simply by considering denser grids. If MLWFs are chosen, the efficiency is maximal and rather coarse grids are often sufficient to faithfully reproduce the entire band structure. Second, once a WF basis is constructed, it not only yields interpolated eigenvalues (e.g., the band structure) but it also enables the Hamiltonian and many other operators to be described in a compact real-space representation. Once the relevant operators in a WF basis are available, one gets access to the full spectrum of theories and software packages that are part of the Wannier

ecosystem, capable of much more complex tasks than just band interpolation. Notably, once a Wannierization is performed with hybrid functionals or at the G_0W_0 level, all other Wannier-interpolated quantities can be obtained at the same level of theory with no extra effort or cost. Finally, thanks to recent work in advanced minimization techniques (Sec. 2.4) and automation (Sec. 3.10), the Wannier interpolation does not require much more human intervention than other standard methods such as smooth Fourier interpolation. In the following, we briefly outline the motivation and the corresponding procedure to deploy Wannier interpolation for two of the most popular excited-state approaches: hybrid functionals, and many-body perturbation theory at the G_0W_0 level.

Hybrid functionals. A very popular approach to improve the accuracy of *ab initio* band structures is to combine explicit density-dependent functionals with Hartree–Fock terms, which leads to orbital-dependent functionals called "hybrids" [36, 173–178]. The procedure to obtain WFs is similar to that in vanilla DFT, except that non-self-consistent field (NSCF) calculations cannot be performed, as the potential is not a functional of the total density only but requires the knowledge of single-particle orbitals. Hence, only self-consistent field (SCF) calculations are performed with hybrid functionals, including some higher-energy empty states (if any) that might be needed to obtain Wannier functions through disentanglement [11]. This is different with respect to DFT, where typically a SCF calculation is performed on the occupied states only (plus some lower-lying conduction bands in the case of metals) and a NSCF calculation is performed including higher-energy empty states, possibly on a different k-point grid. In addition, ground-state calculations are typically performed on the irreducible Brillouin zone (IBZ) by exploiting crystalline symmetries, while `Wannier90` requires a uniform grid on the full Brillouin zone (FBZ). As performing the self-consistent calculation on the FBZ is certainly possible but rather inefficient, the typical procedure involves unfolding the ground-state orbitals and band structure from the IBZ to the FBZ. This is done as a post-processing step performed after the self-consistent calculation and before producing the overlap matrices and the other input required to obtain WFs. For example, in the `Quantum ESPRESSO` distribution [54, 55] this is done through the `open_grid.x` code. Notably, WFs can be used to speed up the core hybrid-functionals calculations, as they allow reducing the number of exchange integrals to be computed [192–197].

G_0W_0. Most of what has been discussed for hybrid functionals also holds for MBPT calculations in the G_0W_0 approximation, with two important remarks. First, G_0W_0 is a one-shot approach in the quasiparticle (QP) approximation which is typically performed on top of a DFT calculation: so the orbitals remain at the KS level and only the energy eigenvalues are corrected, hence neglecting off-diagonal elements of the self-energy in the KS basis. Second, as only the energies are changed at the G_0W_0 level, the KS states might swap their band indices and not be ordered in energy anymore. A typical case where this might manifest clearly are topological insulator candidates (and systems with band inversions in general) such as monolayer TiNI [198], which is topological in DFT and trivial at the G_0W_0 level. The practicalities of obtaining G_0W_0 WFs and related quantities depend on whether the DFT and MBPT calculations are performed with the same distribution (e.g., `VASP` [199]) or with two separate codes (as for example with `Quantum`

`ESPRESSO` [54, 55] and `Yambo` [200]). In general, G_0W_0 QP corrections $\Delta\epsilon_i^{\rm QP} = \epsilon_i^{G_0W_0} - \epsilon_i^{\rm DFT}$ need to be computed on a uniform grid in the FBZ, which can be made efficient by unfolding from the IBZ to the FBZ (in `Yambo`, this operation is carried out by the post-processing utility `ypp`). While orbitals remain at the DFT-KS level, `Wannier90` requires the states to be ordered with ascending energy and, in addition, some input matrices (e.g., the `uHu`) need to be updated with QP corrections. If this is not performed by the *ab initio* engine, it can be taken care by the `Wannier90` utility `gw2wannier90.py` if the DFT eigenvalues and QP corrections are provided in the standard format `seedname.eig`. After this step, the Wannierization can proceed as usual, and it is available in both `Wannier90` [96] and `WanT` [201]. Note that in G_0W_0, QP corrections need to be computed on a subset of the k-point grid required to calculate the self-energy: this can be exploited to speedup the calculation, especially for 2D materials as discussed in [200], because Wannierization typically requires relatively coarse k-point grids. Finally, we briefly touch on beyond-G_0W_0 development of interest from a WF perspective. While Aguilera et al. have shown that off-diagonal components of the self-energy—which are not included in standard perturbative approaches—are very relevant in case of band inversions [202] (such as for topological insulators), Hamann and Vanderbilt have found [203] that, in general, differences between MLWFs obtained with local-density approximation (LDA) and self-consistent GW (QSGW) are minimal.

Bethe–Salpeter equation In order to address neutral excitations, as opposed to the charged excitations of GW, one needs to describe the bound state of an excited electron with the hole that has been created. This is accomplished either using time-dependent density-functional theory or Green's function methods [204]; in the latter case, the Bethe–Salpeter equation (BSE) is solved on top of the GW solutions. Within the Tamm–Dancoff approximation [204–206], the BSE can be recast into an effective two-particle eigenvalue problem [204, 207], which in the electron-hole (e-h) basis reads

$$\sum_{v'c'} \left[D_{vc,v'c'} + 2K^{\rm x}_{vc,v'c'} - K^{\rm d}_{vc,v'c'} \right] A^{\lambda}_{v'c'} = E_\lambda A^{\lambda}_{vc}, \tag{38}$$

where the v, v' and c, c' indices run over valence and conduction states, E_λ are the neutral excitation energies (the poles of the density-density response function), and A^λ_{vc} are the coefficients of the excitonic wavefunctions (that are related to oscillator strengths) in the e-h basis. The effective 2-particle Hamiltonian is made by i) a diagonal term $D_{vc,v'c'} = (\varepsilon_c^{\rm QP} - \varepsilon_v^{\rm QP})\delta_{vv'}\delta_{cc'}$ representing the "bare" e-h transitions (i.e., without accounting for the electron-hole interaction) from the QP theory, ii) an exchange-like term

$$K^{\rm x}_{vc,v'c'} = \int d\mathbf{r}d\mathbf{r}'\, \phi^*_c(\mathbf{r})\phi_v(\mathbf{r})|\mathbf{r}-\mathbf{r}'|^{-1}\phi^*_{v'}(\mathbf{r}')\phi_{c'}(\mathbf{r}'), \tag{39}$$

and iii) a direct screened Coulomb term

$$K^{\rm d}_{vc,v'c'} = \int d\mathbf{r}d\mathbf{r}'\, \phi^*_c(\mathbf{r})\phi_{c'}(\mathbf{r})W(\mathbf{r},\mathbf{r}')\phi^*_{v'}(\mathbf{r}')\phi_v(\mathbf{r}') \tag{40}$$

responsible for an effective attractive interaction between the electron and the hole. Here $\{\phi_i\}$ and $\{\varepsilon_i^{\rm QP}\}$ are the QP wavefunctions and QP energies, respectively. The solution of Eq. (38) in the e-h basis would require the explicit computation of a significant number of empty states,

which becomes in turn a critical convergence parameter. This can be conveniently avoided [208–211] resorting to well established techniques from DFPT [166] by introducing i) the projector over the conduction manifold $\hat{Q} = \mathbb{1} - \hat{P} = \mathbb{1} - \sum_v |\phi_v\rangle\langle\phi_v|$, and ii) a set of auxiliary functions $\xi_v(\mathbf{r}) = \sum_c A_{cv}\phi_c(\mathbf{r})$, usually called a *batch* representation [212, 213]. These are N_v (where N_v is the number of occupied states) auxiliary functions that live in the unperturbed empty-states manifold and provide an equivalent but more compact representation of the excitonic wavefunction $\Theta(\mathbf{r},\mathbf{r}') = \sum_{vc} A_{cv}\phi_v^*(\mathbf{r})\phi_c(\mathbf{r}') = \sum_v \phi_v(\mathbf{r})\xi_v(\mathbf{r}')$. In this representation, the effective 2-particle Hamiltonian is completely specified by its action on the components of the batch [210]:

$$\sum_{v'} D_{vv'}|\xi_{v'}\rangle = \sum_{v'} (\hat{H}^{\mathrm{QP}} - \varepsilon_{v'}\mathbb{1})\delta_{vv'}|\xi_{v'}\rangle \tag{41}$$

$$\sum_{v'} K^{\mathrm{x}}_{vv'}|\xi_{v'}\rangle = \sum_{v'} \hat{Q}\left(\int \frac{1}{|\mathbf{r}-\mathbf{r}'|}\phi^*_{v'}(\mathbf{r}')\xi_{v'}(\mathbf{r}')\,d\mathbf{r}'\right)|\phi_v\rangle \tag{42}$$

$$\sum_{v'} K^{\mathrm{d}}_{vv'}|\xi_{v'}\rangle = \sum_{v'} \hat{Q}\left(\int W(\mathbf{r},\mathbf{r}')\phi^*_{v'}(\mathbf{r}')\phi_{v'}(\mathbf{r}')\,d\mathbf{r}'\right)|\xi_{v'}\rangle. \tag{43}$$

The advantage of this formulation is that there is no explicit reference to the empty states (hidden inside the projector $\hat{Q}$ and the batch representation), and only the N_v auxiliary functions $\{|\xi_v\rangle\}$ need to be determined solving the BSE in the batch representation.

A further computational speed-up (and an improvement on the overall scaling [211]) can be achieved by moving from the KS orbitals to MLWFs and by exploiting their localization to greatly reduce the number of operations needed to evaluate the action of the BSE Hamiltonian on a trial state $|\xi_v\rangle$. This is particularly relevant for the direct term (Eq. (43)), which represents the real bottleneck of the calculations. In the Wannier representation, this becomes

$$\sum_{v'} K^{\mathrm{d}}_{vv'}|\tilde{\xi}_{v'}\rangle = \hat{Q}\left(\sum_{v'}\int W(\mathbf{r},\mathbf{r}')\omega^*_{v'}(\mathbf{r}')\omega_{v'}(\mathbf{r}')\,d\mathbf{r}'\right)|\tilde{\xi}_{v'}\rangle, \tag{44}$$

where $\{\omega_v(\mathbf{r})\}$ are the MLWFs and $\tilde{\xi}_v(\mathbf{r})$ is the batch component in the Wannier representation (simply obtained by rotating the original $\xi_v(\mathbf{r})$ with the unitary matrix rotation that transforms the manifold from the canonical to the MLWF representation). Exploiting locality, one can define a threshold for which a given pair of MLWFs overlap. By excluding non-overlapping pairs of MLWFs from the summation in Eq. (44), it becomes possible to lower the scaling of the evaluation of the action of the direct term on trial states from $\mathcal{O}(N^4)$ to $\mathcal{O}(N^3)$ [211], an approach that has been established and applied in the community [185, 208, 211]. Tight-binding and phenomenological models based on localized representation have also recently appeared [214, 215].

The concept of MLWF can be actually extended to multiparticle Bloch states and has been recently applied to excitons, which are two-particle correlated e-h excitations and where maximal localization can be defined with respect to an average e-h coordinate in real space [216]. The benefits of these maximally localized exciton Wannier functions (MLXWFs) for excitons are essentially the same as those of MLWFs for electrons, including providing a compact basis for *ab initio* exciton TB models and interpolating key quantities such as the excitonic bands, the exciton-phonon matrix elements and Berry curvatures for the exciton wavefunction, while also providing physical insights on the nature of excitons [216].

3.4 Ballistic transport and nanostructures

MLWFs can be used to build the electronic structure of large nanostructures [12, 217] and to determine their ballistic transport when connected to semi-infinite leads [12, 31]. In this latter case, the formalism of Green's functions is used to embed a conductor into the surrounding environment. In all cases, the building blocks are Hamiltonian matrix elements between the localized MLWFs that are used to construct, LEGO™-like, either the desired non-self-consistent Hamiltonian of a much larger nanostructure, or the self-energies embedding the conductor of interest into semi-infinite leads. Importantly, any solid (or surface) can be viewed as an infinite (or semi-infinite, in the case of surfaces) stack of "principal layers" interacting only with neighboring layers [218, 219]. In this way, the infinite-dimensional real-space Hamiltonian can be divided into finite-sized Hamiltonian matrices; for a bulk system (i.e., infinite and periodic) the only independent components are H_{00} and H_{01}, where the former represents the interaction between MLWFs located in the same principal layer, and the latter the interaction between orbitals in one principal layer and the next.

As discussed by Nardelli [220], one can consider a system composed of a conductor C connected to two semi-infinite leads, R and L (C, R, and L are in themselves composed by a finite or infinite number of principal layers). The conductance through C is related to the scattering properties of C itself via the Landauer formula [221]:

$$\mathcal{G}(E) = \frac{2e^2}{h}\mathcal{T}(E), \tag{45}$$

where $\mathcal{T}$ is the transmission function, $\mathcal{G}$ is the conductance, and $\mathcal{T}$ is the probability that an electron injected at one end of the conductor will transmit to the other end. This transmission function can be expressed in terms of the Green's functions of the conductors and of its coupling to the leads [218, 219] as

$$\mathcal{T} = \mathrm{Tr}(\Gamma_L G_C^r \Gamma_R G_C^a), \tag{46}$$

where $G_C^{\{r,a\}}$ are the retarded and advanced Green's functions of the conductor, respectively, and $\Gamma_{\{L,R\}}$ are functions that describe the coupling of the conductor to the two leads. To compute the Green's function of the conductor, one starts from the equation for the Green's function of the whole system:

$$(\epsilon - H)G = \mathbb{1} \tag{47}$$

where $\epsilon = E + \mathrm{i}\eta$ with η arbitrarily small, and $\mathbb{1}$ is the identity matrix. The matrix representation of G in a WFs basis can be partitioned as

$$\begin{pmatrix} G_L & G_{LC} & G_{LCR} \\ G_{CL} & G_C & G_{CR} \\ G_{LRC} & G_{RC} & G_R \end{pmatrix} = \tag{48}$$

$$\begin{pmatrix} (\epsilon - H_L) & H_{LC} & 0 \\ H_{LC}^\dagger & (\epsilon - H_C) & H_{CR} \\ 0 & H_{CR}^\dagger & (\epsilon - H_R) \end{pmatrix}^{-1}.$$

We can then write the conductor Green's function as

$$G_C(E) = (\epsilon - H_C - \Sigma_L - \Sigma_R)^{-1}, \tag{49}$$

where the effect of the semi-infinite leads on the conductor is described by the self-energies $\Sigma_{L,R}$, and the coupling functions $\Gamma_{\{L,R\}}$ are obtained from the self-energies as

$$\Gamma_{\{L,R\}} = \mathrm{i}[\Sigma^r_{\{L,R\}} - \Sigma^a_{\{L,R\}}]\,; \tag{50}$$

here, the advanced self-energy is the Hermitian conjugate of the retarded one, and we solve for the latter. Given that the semi-infinite leads are also made of principal layers, one can construct the self-energies as [220]

$$\begin{aligned} \Sigma_L &= H^\dagger_{LC}(\epsilon - H^L_{00} - (H^L_{01})^\dagger \overline{T}_L)^{-1} H_{LC}, \\ \Sigma_R &= H_{CR}(\epsilon - H^R_{00} - H^R_{01} T_R)^{-1} H^\dagger_{CR}, \end{aligned} \tag{51}$$

where, e.g., H_{00} describes the intralayer interactions and H_{01} the interlayer couplings. The transfer matrices $\overline{T}_{L,R}$ and $T_{L,R}$, defined such that $G_{10} = TG_{00}$ and $G_{00} = \overline{T}G_{10}$, are calculated following the iterative procedure by Lopez-Sancho et al. [222]. The only inputs are the matrix elements of the Hamiltonian H_{mn} in a localized representation; the accuracy of the results depends on having principal layers that do not couple beyond next neighbors, i.e., on having a well-localized basis. The knowledge of the conductor Green's function G_C also gives direct information on the electronic spectrum via the spectral density of the electronic states: $N_C(E) = -(1/\pi)\mathrm{Im}(\mathrm{Tr}G_C(E))$.

As an example, we take a (5,5) single-wall carbon nanotube, described with a supercell containing 100 carbon atoms (five times the primitive cell); the disentanglement and Wannierization procedure results in 150 sp^2 orbitals and 100 p_z orbitals. Such supercell size is large enough to allow for Γ-sampling only in the BZ, and to have negligible overlap with the MLWFs belonging to the second next supercell. We show in Fig. 8 the results for the band structure, quantum conductance, and density of states, adapted from [12]. The metallic nanotube, notwithstanding its $\sim$2 eV pseudo-gap at Γ, shows a band structure in perfect agreement with that obtained from a very fine sampling of the BZ, and perfect agreement between the steps in conductance and the peaks in the van Hove singularities, with the maxima and the minima of the band dispersions at arbitrary points in the BZ. While these methodologies based on WFs have been implemented either as an extension of `Wannier90` [223] or standalone in the WF-based `WanT` code [201], analogous techniques have been developed for other types of localized orbitals and implemented in simulation codes such as `TranSiesta/Atomistix Toolkit` [224], `SMEAGOL` [225], `OpenMX` [226], `NEMO5` [227–230], `nextnano` [231], `NanoTCAD Vides` [232, 233], `KWANT` [234], some of which also provide an interface with the Wannier ecosystem. In addition, we emphasize that different kinds of WFs can be adopted as basis for *ab initio* quantum transport calculations, such as the POWFs [56, 57] discussed in Sec. 2.4, which have been used both at the DFT [235] and GW [236] level.

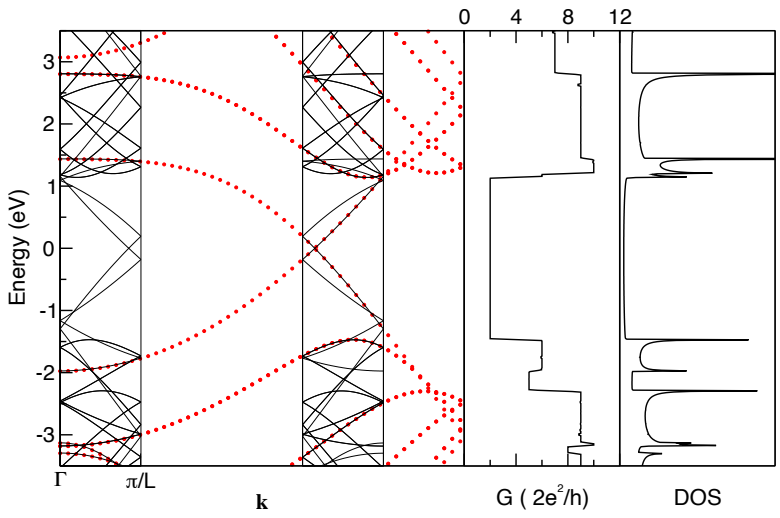

Figure 8: Left panel: Comparison of the band structure for a (5,5) single-walled carbon nanotube, calculated in the 20-atom primitive cell with a self-consistent Hamiltonian using 5 k points along the 1-dimensional Brillouin zone ($k = n\pi/L, n = 0, 1, ..., 4$) and then diagonalized non-self-consistently everywhere (red dots), or calculated in a supercell 5 times longer. In this latter case, the Brillouin zone is 5 times shorter, it displays 5 times more bands, and the Hamiltonian is consistently obtained using Γ sampling only. While a pseudogap of more than 2 eV is present at Γ, non-self-consistent diagonalization everywhere (solid thin lines) captures very faithfully the metallic character of the nanotube. Folding the original bands (red dots) into the smaller Brillouin zone of the supercell also shows perfect agreement between the calculations. These results highlight how disentanglement in the supercell recovers from the empty states at Γ what is needed to capture the character of filled and empty states away from Γ. The center and right panels reinforce this point, showing the ballistic conductance and density of states obtained from the Green's functions calculated using the supercell Wannier functions. Notably, the van Hove singularities and conductance steps are captured with great accuracy even when the bands edges are at arbitrary points, highlighting the role of MLWFs as excellent interpolators and building blocks for the non-self-consistent electronic structure of large-scale nanostructures (see also [12]).

3.5 Berryology

3.5.1 Motivation

Berry phases and related quantities are central to the description of the electronic properties of crystals [10, 164]. Here are some representative examples *.

1. The electronic contribution to the electric polarization of an insulator is given by

$$\mathbf{P}_{\rm el} = -e \sum_{n}^{\rm occ} \int_{\rm BZ} \frac{d^3k}{(2\pi)^3} \, \mathbf{A}_{\mathbf{k},nn} \, , \tag{52}$$

   where $-e$ is the electron charge and $\mathbf{A}_{\mathbf{k},nn}$ are diagonal elements of the Berry connection matrix,

$$\mathbf{A}_{\mathbf{k},mn} = i \langle u_{m\mathbf{k}} | \boldsymbol{\nabla}_{\mathbf{k}} u_{n\mathbf{k}} \rangle \, . \tag{53}$$

2. Off-diagonal elements of $\mathbf{A}_{\mathbf{k}}$ describe electric-dipole transition moments, allowing the in-

*All the formulas are given for single band occupancy.

terband optical conductivity to be expressed as

$$\sigma_{ab}(\omega) = \frac{ie^2}{\hbar}\sum_{m,n}\int_{\mathrm{BZ}}\frac{d^3k}{(2\pi)^3}\,(f_{m\mathbf{k}}-f_{n\mathbf{k}})\times \\ \times\frac{\varepsilon_{m\mathbf{k}}-\varepsilon_{n\mathbf{k}}}{\varepsilon_{m\mathbf{k}}-\varepsilon_{n\mathbf{k}}-\hbar(\omega+i0^+)}A^a_{\mathbf{k},nm}A^b_{\mathbf{k},mn}\,, \tag{54}$$

where $f_{n\mathbf{k}}$ is the Fermi-Dirac occupation factor.

3. The Berry curvature is defined as the curl of the Berry connection,

$$\boldsymbol{\Omega}_{n\mathbf{k}} = \boldsymbol{\nabla}_{\mathbf{k}}\times\mathbf{A}_{\mathbf{k},nn} = -\mathrm{Im}\,\langle\boldsymbol{\nabla}_{\mathbf{k}}u_{n\mathbf{k}}|\times|\boldsymbol{\nabla}_{\mathbf{k}}u_{n\mathbf{k}}\rangle\,, \tag{55}$$

and its integral over the occupied states gives the intrinsic AHC,

$$\sigma_{yx} = \frac{e^2}{\hbar}\int_{\mathrm{BZ}}\frac{d^3k}{(2\pi)^3}\sum_n f_{n\mathbf{k}}\Omega^z_{n\mathbf{k}}\,. \tag{56}$$

4. The ground-state orbital magnetization reads

$$\mathbf{M}_{\mathrm{orb}} = \int_{\mathrm{BZ}}\frac{d\mathbf{k}}{(2\pi)^3}\sum_n f_{n\mathbf{k}}\left[\mathbf{m}^{\mathrm{orb}}_{n\mathbf{k}}+\frac{e}{\hbar}\left(\varepsilon_{\mathrm{F}}-\varepsilon_{n\mathbf{k}}\right)\boldsymbol{\Omega}_{n\mathbf{k}}\right]\,, \tag{57}$$

with ε_{F} the Fermi energy and

$$\mathbf{m}^{\mathrm{orb}}_{n\mathbf{k}} = \frac{e}{2\hbar}\mathrm{Im}\,\langle\boldsymbol{\nabla}_{\mathbf{k}}u_{n\mathbf{k}}|\times\left(\hat{H}_{\mathbf{k}}-\varepsilon_{n\mathbf{k}}\right)|\boldsymbol{\nabla}_{\mathbf{k}}u_{n\mathbf{k}}\rangle \tag{58}$$

the intrinsic orbital moment of a Bloch state.

5. To first order in applied fields $\mathbf{E}$ and $\mathbf{B}$, the semiclassical equations of motion for a wavepacket in a Bloch band read

$$\dot{\mathbf{r}} = \frac{1}{\hbar}\boldsymbol{\nabla}_{\mathbf{k}}\tilde{\varepsilon}_{n\mathbf{k}} - \dot{\mathbf{k}}\times\boldsymbol{\Omega}_{n\mathbf{k}}\,, \tag{59a}$$

$$\dot{\mathbf{k}} = -\frac{e}{\hbar}\mathbf{E} - \frac{e}{\hbar}\dot{\mathbf{r}}\times\mathbf{B}\,, \tag{59b}$$

where

$$\tilde{\varepsilon}_{n\mathbf{k}} = \varepsilon_{n\mathbf{k}} - \left(\mathbf{m}^{\mathrm{spin}}_{n\mathbf{k}}+\mathbf{m}^{\mathrm{orb}}_{n\mathbf{k}}\right)\cdot\mathbf{B} \tag{60}$$

is the Zeeman-shifted band energy.

The motivation to apply Wannier interpolation to Berry-type quantities came from pioneering *ab initio* calculations of the AHC in the ferromagnets $SrRuO_3$ [237] and BCC Fe [159], which revealed the integrand of Eq. (56) to be strongly peaked in the vicinity of avoided crossings between occupied and empty bands; resulting in the need to sample the BZ over millions of k points to reach convergence. An efficient Wannier-interpolation scheme for evaluating the AHC was developed in [238], and since then the methodology has been applied to many other properties.

Wannier interpolation of Berry-type quantities was introduced in version 2 of `Wannier90` as part of its post-processing code `postw90` [112], with the ability to compute AHC [238], interband optical conductivity [13], and orbital magnetization [239]. The list of available properties

has grown considerably since then, and more recently the `WannierBerri` code package [240] introduced several methodological improvements including "pruned FFT" [241, 242] (a combination of fast and slow Fourier transforms), and the use of symmetries and of the tetrahedron method for BZ integrals. Other codes also compute Berry-type quantities in different contexts, such as `dynamics-w90` [243] for time-dependent dynamics. We note that some codes, including `WannierTools` [172] and `linres` [244], implement some functionalities but with additional approximations (see discussion of Eq. (66) below). The reader should consult the documentation of the codes for an up-to-date description of their capabilities.

In the following, we outline the basic interpolation strategy for Berry-type quantities, using the off-diagonal Berry connection as an example (the diagonal Berry connection that enters the Berry phase requires a separate treatment, see Sec. 3.6). For discussion purposes, we adopt the modified phase convention for Bloch sums indicated in Eq. (37).

3.5.2 Wannier interpolation of the interband Berry connection

We wish to evaluate off-diagonal elements of the Berry connection matrix in the Hamiltonian gauge. Inserting in Eq. (53) the relation (22) between interpolated Bloch states in the Hamiltonian and Wannier gauges, we obtain

$$\mathbf{A}^{\mathrm{H}}_{\mathbf{k}'} = i\mathcal{U}^{\dagger}_{\mathbf{k}'}\boldsymbol{\nabla}_{\mathbf{k}'}\mathcal{U}_{\mathbf{k}'} + \mathcal{U}^{\dagger}_{\mathbf{k}'}\mathbf{A}^{\mathrm{W}}_{\mathbf{k}'}\mathcal{U}_{\mathbf{k}'}\,. \tag{61}$$

Note the extra (first) term compared to the gauge-transformation rule (29) for a lattice-periodic matrix object. Recalling from Eq. (18) that the columns of $\mathcal{U}_{\mathbf{k}'}$ are eigenvectors of $H^{\mathrm{W}}_{\mathbf{k}'}$, the off-diagonal matrix elements of that term can be evaluated from non-degenerate perturbation theory as

$$\left(\mathcal{U}^{\dagger}_{\mathbf{k}'}\boldsymbol{\nabla}_{\mathbf{k}'}\mathcal{U}_{\mathbf{k}'}\right)_{mn} = \frac{\left[\mathcal{U}^{\dagger}_{\mathbf{k}'}\left(\boldsymbol{\nabla}_{\mathbf{k}'}H^{\mathrm{W}}_{\mathbf{k}'}\right)\mathcal{U}_{\mathbf{k}'}\right]_{mn}}{\varepsilon^{\mathrm{H}}_{n\mathbf{k}'} - \varepsilon^{\mathrm{H}}_{m\mathbf{k}'}}\,. \tag{62}$$

All quantities on the right-hand side can be obtained from Eqs. (17) and (18) starting from $\langle \mathbf{0}i|\hat{H}|\mathbf{R}j\rangle$ and $\boldsymbol{\tau}_j = \langle \mathbf{0}j|\hat{\mathbf{r}}|\mathbf{0}j\rangle$ (the latter appears in the modified phase factors in Eq. (37)). For the second term in Eq. (61), we also need

$$\mathbf{A}^{\mathrm{W}}_{\mathbf{k}',ij} = \sum_{\mathbf{R}} e^{i\mathbf{k}'\cdot(\mathbf{R}+\boldsymbol{\tau}_j-\boldsymbol{\tau}_i)}\mathbf{d}_{ij}(\mathbf{R})\,, \tag{63}$$

which follows from inserting in Eq. (53) the Bloch sum (20) with the modified phase factors. Here $\mathbf{d}_{ij}(\mathbf{R})$ are the off-diagonal matrix elements of $\hat{\mathbf{r}}$ in the Wannier basis, that is,

$$\langle \mathbf{0}i|\hat{\mathbf{r}}|\mathbf{R}j\rangle = \delta_{\mathbf{R},\mathbf{0}}\delta_{ij}\boldsymbol{\tau}_j + \mathbf{d}_{ij}(\mathbf{R})\,. \tag{64}$$

The matrix elements $\langle \mathbf{0}i|\hat{H}|\mathbf{R}j\rangle$ are evaluated using Eq. (16), and the corresponding procedure for $\langle \mathbf{0}i|\hat{\mathbf{r}}|\mathbf{R}j\rangle$ is as follows. First, we can use Eq. (6a) to write $\langle \mathbf{0}i|\hat{\mathbf{r}}|\mathbf{R}j\rangle$ as $(1/N)\sum_{\mathbf{k}} e^{-i\mathbf{k}\cdot\mathbf{R}}A^{\mathrm{W}}_{\mathbf{k},ij}$. Since the Bloch functions are smooth in the Wannier gauge, $\mathbf{A}^{\mathrm{W}}_{\mathbf{k},ij}$ can be evaluated on the *ab initio* grid by discretizing the $\mathbf{k}$ derivative appearing in Eq. (53). Adopting the finite-differences

scheme described in [4] and [83] we obtain

$$\langle \mathbf{0}i|\hat{\mathbf{r}}|\mathbf{R}j\rangle = \frac{i}{N}\sum_{\mathbf{k}} e^{-i\mathbf{k}\cdot\mathbf{R}} \sum_{\mathbf{b}} w_b \mathbf{b} \times \\ \times \sum_{m,n} V^*_{\mathbf{k},mi} M^{(\mathbf{k},\mathbf{b})}_{mn} V_{\mathbf{k}+\mathbf{b},nj}\,, \tag{65}$$

where $\mathbf{b}$ are vectors connecting neighboring grid points, w_b are appropriately chosen weights, $M^{(\mathbf{k},\mathbf{b})}$ are the overlap matrices defined by Eq. (12), and $V_{\mathbf{k}}$ are the Wannierization matrices in Eq. (6b); since the overlap matrices were computed in preparation for the WF construction procedure, and the Wannierization matrices were obtained at the end of that procedure, both are readily available.

Once $\langle \mathbf{0}i|\hat{H}|\mathbf{R}j\rangle$ and $\langle \mathbf{0}i|\hat{\mathbf{r}}|\mathbf{R}j\rangle$ have been tabulated, the interband Berry connection can be evaluated from Eqs. (61)–(63), with the matrices $\mathcal{U}_{\mathbf{k}'}$ therein (along with the interpolated energy eigenvalues) given by Eq. (18). Finally, the Berry connection and energy eigenvalues are inserted in Eq. (54) to obtain the interband optical conductivity [13].

Equation (65) entails a numerical error of order $(\Delta k)^2$, where Δk is the *ab initio* mesh spacing [4, 83]. The direct real-space mesh integration method mentioned below Eq. (16) should be free of such errors, but it is not as practical in the context of k-space Wannierization schemes. It is therefore desirable to develop improved discretized k-space formulas for $\langle \mathbf{0}i|\hat{\mathbf{r}}|\mathbf{R}j\rangle$ and related matrix elements. A higher-order generalization of the discretization scheme of [4] and [83] was recently introduced [245], and further improvements are currently under way [246, 247].

In empirical tight-binding, it is customary to approximate the position matrix elements by dropping the second term in Eq. (64) [10, 248],

$$\langle \mathbf{0}i|\hat{\mathbf{r}}|\mathbf{R}j\rangle \approx \delta_{\mathbf{R},\mathbf{0}}\delta_{ij}\boldsymbol{\tau}_j\,. \tag{66}$$

In this approximation, and when the modified phase convention (37) is used, the matrix $\mathbf{A}^{\mathrm{W}}_{\mathbf{k}'}$ in Eq. (63) vanishes; Eq. (61) for $\mathbf{A}^{\mathrm{H}}_{\mathbf{k}'}$ then reduces to its first term, which can be interpreted as the "internal" Berry connection of the tight-binding eigenvectors; this is how tight-binding codes such as `PythTB` evaluate Berry phases and curvatures [249], which is quite natural in the context of toy-model calculations.

The above approximation is harder to justify when using *ab initio* WFs, given that the discarded $\mathbf{d}_{ij}(\mathbf{R})$ matrix elements are readily available, as mentioned above; even so, that approximation is made by some codes, including `WannierTools` [172] and `linres` [244]. The role of intra-atomic $\mathbf{d}_{ij}(\mathbf{R})$ matrix elements in tight-binding calculations of the linear dielectric function was studied in [250]; in [251], that analysis was extended to inter-atomic matrix elements and to non-linear optical responses, using Wannier interpolation. The importance of the $\mathbf{d}_{ij}(\mathbf{R})$ off-diagonal elements for gauge invariance has been discussed also in the context of time-dependent dynamics [252].

3.5.3 Other Berry-type quantities

The interpolation of the Berry curvature $\boldsymbol{\Omega}_{\mathbf{k}}$ proceeds along similar lines, allowing the computation of AHC from Eq. (56) [238], and the procedure can be extended to spin Hall conductivity

(SHC) [253, 254] or non-linear responses. For example, non-linear optical and AHCs involve k-derivatives of $\mathbf{A}_\mathbf{k}$ and $\mathbf{\Omega}_\mathbf{k}$, respectively [160, 255]; in the same way as band derivatives (see Sec. 3.3.2), both are conveniently evaluated by Wannier interpolation [256–258]. To interpolate $\mathbf{A}_\mathbf{k}$, $\mathbf{\Omega}_\mathbf{k}$, and their k-derivatives, only $\langle \mathbf{0}i|\hat{H}|\mathbf{R}j\rangle$ and $\langle \mathbf{0}i|\hat{\mathbf{r}}|\mathbf{R}j\rangle$ are needed, but other quantities require additional matrix elements [†]. For example, the orbital moment in Eq. (58) requires $\langle \mathbf{0}i|\hat{H}(\hat{\mathbf{r}}-\mathbf{R})|\mathbf{R}j\rangle$ and $\langle \mathbf{0}i|\hat{r}_a\hat{H}(\hat{r}-R)_b|\mathbf{R}j\rangle$ [239]; and while the former can be evaluated on the *ab initio* grid using the same ingredients entering Eqs. (16) and (65) for $\langle \mathbf{0}i|\hat{H}|\mathbf{R}j\rangle$ and $\langle \mathbf{0}i|\hat{\mathbf{r}}|\mathbf{R}j\rangle$, the latter also requires $\langle u_{m\mathbf{k}+\mathbf{b}_1}|\hat{H}_\mathbf{k}|u_{n\mathbf{k}+\mathbf{b}_2}\rangle$, which must be calculated separately [239]. As in the case of Eq. (61) for $\mathbf{A}_{\mathbf{k}'}$, the resulting interpolation formula contains an "internal" term analogous to Eq. (58) itself, but expressed in terms of the TB eigenvectors and Hamiltonian. That term can be evaluated from $\langle \mathbf{0}i|\hat{H}|\mathbf{R}j\rangle$ and $\boldsymbol{\tau}_j$ alone, but it leaves out important atomic-like contributions that are encoded in the other matrix elements needed for a full calculation [239, 260].

Matrix element	Wannier90 file	Needed for	Implemented in	Computed by `mmn2uHu` from
$\langle u_{m\mathbf{k}}\|\hat{H}_\mathbf{k}\|u_{n\mathbf{k}}\rangle = \varepsilon_{n\mathbf{k}}\delta_{mn}$	`*.eig`	Transport, optics, $\mathbf{m}^{\rm orb}_\mathbf{k}$	All	
$\langle u_{m\mathbf{k}}\|\hat{\boldsymbol{\sigma}}\|u_{n\mathbf{k}}\rangle$	`*.spn`	$\mathbf{m}^{\rm spin}_\mathbf{k}$	QE,VASP	
$\langle u_{m\mathbf{k}}\|u_{n\mathbf{k}+\mathbf{b}}\rangle$	`*.mmn`	$\mathbf{A}_\mathbf{k}$, $\mathbf{\Omega}_\mathbf{k}$, $\mathbf{m}^{\rm orb}_\mathbf{k}$, all below	All	
$\langle u_{m\mathbf{k}+\mathbf{b}_1}\|\hat{H}_\mathbf{k}\|u_{n\mathbf{k}+\mathbf{b}_2}\rangle$	`*.uHu`	$\mathbf{m}^{\rm orb}_\mathbf{k}$	QE	`*.eig`, `*.mmn`
$\langle u_{m\mathbf{k}+\mathbf{b}_1}\|u_{n\mathbf{k}+\mathbf{b}_2}\rangle$	`*.uIu`	$q^{ab}_\mathbf{k}$	QE	`*.mmn`
$\langle u_{m\mathbf{k}}\|\hat{\boldsymbol{\sigma}}\hat{H}_\mathbf{k}\|u_{n\mathbf{k}+\mathbf{b}}\rangle$	`*.sHu`	SHC in [254]	QE	`*.eig`, `*.mmn`, `*.spn`
$\langle u_{m\mathbf{k}}\|\boldsymbol{\sigma}\|u_{n\mathbf{k}+\mathbf{b}}\rangle$	`*.sIu`	SHC in [254]	QE	`*.mmn`, `*.spn`

Table 1: *Ab initio* matrix elements that are used *explicitly* in setting up the WF matrix elements needed to perform common interpolation tasks, SHC stands for spin Hall conductivity. * denotes the seedname specified in the input file of `Wannier90`. QE = `Quantum ESPRESSO`, $\mathbf{A}_\mathbf{k}$ is the Berry connection or electric dipole matrix (53), $\mathbf{\Omega}_\mathbf{k}$ is the Berry curvature (55), $\mathbf{m}^{\rm orb}_\mathbf{k}$ is the intrinsic orbital magnetic dipole (58), and $q^{ab}_\mathbf{k}$ is the intrinsic electric quadrupole (for the matrix definitions of $\mathbf{m}^{\rm orb}_\mathbf{k}$ and $q^{ab}_\mathbf{k}$, see [261]). The optical conductivity (54) in the electric-dipole approximation involves $\varepsilon_{n\mathbf{k}}$ and $\mathbf{A}_\mathbf{k}$, the AHC (56) involves $\varepsilon_{n\mathbf{k}}$ and $\mathbf{\Omega}_\mathbf{k}$, and the orbital magnetization (57) involves $\varepsilon_{n\mathbf{k}}$, $\mathbf{\Omega}_\mathbf{k}$ and $\mathbf{m}^{\rm orb}_\mathbf{k}$. Spatially dispersive responses such as natural optical activity depend on $\varepsilon_{n\mathbf{k}}$, $\mathbf{A}_\mathbf{k}$, $\mathbf{m}^{\rm orb}_\mathbf{k}$, $\mathbf{m}^{\rm spin}_\mathbf{k}$, and $q^{ab}_\mathbf{k}$ [261]. The `mmn` (and `eig`) matrix elements are needed for constructing the (disentangled) WFs, and hence they are used *implicitly* when interpolating any physical quantity.

The *ab initio* matrix elements needed for various interpolation tasks are listed in Table 1. The files `*.eig` and `*.mmn` are required already for constructing the WFs, and therefore they are provided by the interface code of every *ab initio* code that is compatible with `Wannier90`. The file `*.spn` is provided by the interface of both `Quantum ESPRESSO` and `VASP`. As for the other matrix elements listed in Table 1, at present they are only implemented in `pw2wannier90.x`, the interface of `Quantum ESPRESSO`.

As a workaround for obtaining these quantities from the output of other *ab initio* engines,

[†]By explicitly plugging the Bloch sum of Eq. (20) into the RHS of Eq. (55), one may think that a matrix element $\langle \mathbf{0}i|\hat{r}_a\hat{r}_b|\mathbf{R}j\rangle$ might be needed. However, this term is symmetric under the exchange of a and b, therefore it does not contribute to the cross-product, as shown in Eq. (40) of Ref. [259].

one can resort to a sum-over-states procedure. For example, the `uHu` matrix elements may be expressed as

$$\langle u_{m\mathbf{k}+\mathbf{b}_1}|\hat{H}_{\mathbf{k}}|u_{n\mathbf{k}+\mathbf{b}_2}\rangle \approx \sum_{l}^{l_{\max}} \langle u_{m\mathbf{k}+\mathbf{b_1}}|u_{l\mathbf{k}}\rangle \varepsilon_{l\mathbf{k}} \langle u_{l\mathbf{k}}|u_{n\mathbf{k}+\mathbf{b_2}}\rangle \tag{67}$$

in terms of the energy eigenvalues and overlap matrices, and the relevant matrices for spin Hall conductivity can be obtained similarly [253]. Since the summation is done before Wannierization, the number $l_{\max}$ of states included in the non-self-consistent *ab initio* calculation can be systematically increased until the desired level of convergence is reached.

The above procedure is implemented for `uHu`, `uIu`, `sHu` and `sIu` in the utility `mmn2uHu` [262] provided with the `WannierBerri` code package [240]. Besides its use as a workaround, it can serve as a benchmark for testing future implementations of those matrix elements in various interface codes between *ab initio* and Wannier engines.

3.6 Topological invariants and related properties

The topological aspects of band theory have been studied intensively over the past two decades [10, 263], and *ab initio* calculations have been central to that effort [264]: they are used for identifying candidate topological materials, to determine topological invariants, and to calculate surface bands that can be compared with angle-resolved photoemission measurements.

WFs feature prominently in topological band theory. For example, quantum anomalous Hall insulators [265] (a.k.a. Chern insulators) can be defined as 2D systems where it is not possible [‡] to construct a set of exponentially localized WFs [10, 22, 68]: this is known as a "topological obstruction". More generally, symmetry-protected topological insulators can typically be defined as insulators for which it is not possible to construct a set of WFs spanning the valence bands without breaking the protecting symmetry in the choice of gauge [72, 267]. Prominent examples include 2D quantum spin Hall insulators [268–270] and 3D $\mathbb{Z}_2$ topological insulators [271], where the protecting symmetry is time reversal, and topological crystalline insulators, which are instead protected by crystalline symmetries [272].

A second example is the "Wannier spectrum" defined by the centers of hybrid (a.k.a. hermaphrodite) orbitals [273] that are Wannier-like along $\hat{\mathbf{z}}$ and Bloch-like along $\hat{\mathbf{x}}$ and $\hat{\mathbf{y}}$. The surface energy spectrum $\varepsilon_n(k_x, k_y)$ can be continuously deformed into the bulk Wannier spectrum $z_n(k_x, k_y)$ obtained by Wannierizing along the surface normal [274, 275], allowing to infer the topological flow of the surface energy bands from that of the bulk Wannier bands [276]. In some cases, the topological indices can be deduced from the Wannier band structure [277, 278].

WFs also play a more practical role in the study of topological materials, as several of the electronic-structure packages that are commonly used to characterize them rely on a Wannier/TB representation (despite the obstruction mentioned above [72, 267], topological insulators still afford a Wannier representation, provided that the WFs span a few low-lying conduction states along with the valence bands).

In particular, both `PythTB` [169] and `WannierTools` [172] work with orthogonal TB models,

[‡]Very recent work [266] suggests that it might be possible to construct optimally localized WFs even in presence of non-vanishing Chern numbers, at least for the simple case of one isolated band.

and have the option to import TB Hamiltonians generated by a Wannier engine using either the `*_hr.dat` or the `*_tb.dat` file format (as mentioned above, the latter also includes the matrix elements of the position operator in the Wannier basis, and the coordinates of the lattice vectors). The key point is that the Wannierized Hamiltonian preserves the topological features of the original first-principles electronic structure; the identification and characterization of those features can therefore be carried out entirely in the Wannier representation, which is often more convenient and/or efficient than proceeding directly from the *ab initio* Bloch states.

The simplest example of a topological band-structure feature is an isolated touching between a pair of bands, known as a "Weyl point" [10, 279]. Weyl points are fundamentally different from weak avoided crossings, but most band interpolation schemes are unable to tell them apart; instead, Wannier interpolation correctly distinguishes between the two. The distinction is rooted in the fact that a Weyl node acts as a monopole source or sink of Berry curvature in $\mathbf{k}$ space, allowing to associate with it a topological invariant known as the "chiral charge."

The chiral charge χ (typically ±1, but sometimes ±2 or ±3 [280, 281]) can be determined in two different ways: (i) from the quantized Berry-curvature flux through a small surface $\mathcal{S}$ enclosing the Weyl point [10, 282],

$$\int_{\mathcal{S}} \mathbf{\Omega}_{n\mathbf{k}} \cdot \hat{\mathbf{n}} = -2\pi\chi \,, \tag{68}$$

where $\hat{\mathbf{n}}$ is a unit vector in the direction of $\boldsymbol{\nabla}_{\mathbf{k}}\varepsilon_{n\mathbf{k}}$; (ii) by evaluating the Berry phase

$$\phi_n(\mathcal{C}) = \oint_{\mathcal{C}} \mathbf{A}_{nn\mathbf{k}} \cdot d\mathbf{k} \tag{69}$$

around contours $\mathcal{C}$ at fixed latitude on an enclosing spherical surface, and then tracking its evolution from zero at the south pole to $2\pi\chi$ at the north pole [277].

The latter procedure is implemented in both `Z2Pack` [283] and `WannierTools`. All that is required is the TB Hamiltonian $\langle \mathbf{0}i|\hat{H}|\mathbf{R}j\rangle$, from which one obtains the eigenvectors on a discrete mesh $\{\mathbf{k}_j\}$ of points along each contour; the Berry phase is then evaluated by finite differences from the overlaps between TB eigenvectors on consecutive points along $\mathcal{C}$ as follows [10],

$$\phi_n^{(\mathrm{int})}(\mathcal{C}) = -\mathrm{Im}\,\ln \Pi_j \langle\!\langle u_{n\mathbf{k}_j} \| u_{n\mathbf{k}_{j+1}} \rangle\!\rangle \,, \tag{70}$$

where $\| u_{n\mathbf{k}_j} \rangle\!\rangle$ denotes a column vector of the matrix $\mathcal{U}_{\mathbf{k}_j}$ defined by Eq. (18). The above expression corresponds, in the language of Sec. 3.5, to the internal part of the Berry phase (69), which also contains an external part

$$\phi_n^{(\mathrm{ext})}(\mathcal{C}) = \sum_j \langle\!\langle u_{n\mathbf{k}_j} \| \mathbf{A}^{\mathrm{W}}_{\mathbf{k}} \| u_{n\mathbf{k}_j} \rangle\!\rangle \cdot \Delta\mathbf{k} \,, \tag{71}$$

where $\Delta\mathbf{k} = (\mathbf{k}_{j+1} - \mathbf{k}_{j-1})/2$ [259]. The two parts arise from discretizing the integral along $\mathcal{C}$ of the two terms in Eq. (61) for the interpolated Berry connection; the internal term only depends on $\langle \mathbf{0}i|\hat{H}|\mathbf{R}j\rangle$, while the external one also requires $\langle \mathbf{0}i|\hat{\mathbf{r}}|\mathbf{R}j\rangle$. The 2π indeterminacy in the Berry phase comes from the former, while the latter is single-valued and hence it does not contribute to the quantized change in Berry phase from the south to the north pole of a spherical surface; this is why χ can be determined from the TB Hamiltonian alone.

Weyl crossings can occur at arbitrary points in the BZ, which makes it difficult to spot them in the band structure. By allowing to quickly evaluate energy eigenvalues and band velocities

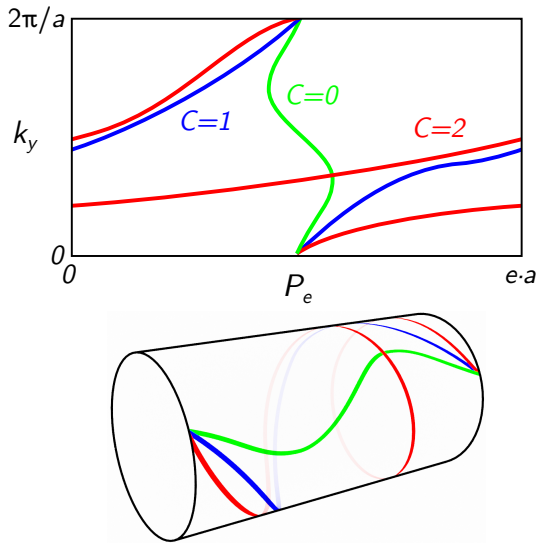

Figure 9: Sketch of some possible evolutions of hybrid polarization $P_e(k_y)$, i.e. the sum of hybrid Wannier charge centers, across the BZ. Chern numbers C correspond to different winding numbers. See [277] for an in-depth discussion.

at arbitrary k points, Wannier interpolation provides a practical solution to this problem [282]: to locate the degeneracies between bands n and $n+1$, define a gap function $\varepsilon_{n+1\mathbf{k}} - \varepsilon_{n\mathbf{k}}$, and search for its minima using a minimization method such as conjugate-gradient, starting from a sufficiently dense grid of k points. After discarding local minima where the gap function is above some numerical threshold, one is left with candidate degeneracies that can be further characterized; they include not only point nodes such as Weyl and Dirac nodes [279], but also nodal lines [284, 285]. This procedure is implemented in `WannierTools`.

Topological materials feature characteristic boundary modes that reflect the bulk topology [10, 263]. In the case of Weyl semimetals, those modes take the form of "Fermi arcs" connecting the projections of bulk Weyl nodes of opposite chirality onto the surface BZ [10, 279]. `PythTB` and `WannierTools` allow to terminate a bulk TB model along specified directions, creating ribbons or slabs whose boundary modes can then be inspected by plotting the energy bands. `WannierTools` also has the option to obtain a surface spectral function from the Green's function calculated for a semi-infinite system. We remark that, in general, these methods yield boundaries that are the result of a truncation of the Wannier Hamiltonian, where the on-site energies and hoppings between surface (edge) atoms are left unchanged to their bulk value. More broadly, these methods completely neglect any relaxation, charge redistribution and reconstruction of the surface (edge). Hence, these are very crude and unrealistic approximations, and the corresponding calculations do not provide a first-principles description of the boundary electronic structure, even if they derive from a bulk Wannier Hamiltonian that was calculated with first-principles methods. Still, they provide valuable insights for the prediction of purely topological properties, in particular the existence of topologically protected surface (edge) states such as chiral or helical edge states, surface Dirac cones, or Fermi arcs. While these calculations can support the *existence* of these boundary states, their precise *band dispersion* requires to treat more explicitly the boundary electronic structure, typically through supercell slab (ribbon) simulations with structural optimization.

As already mentioned, another very useful tool for diagnosing topological behaviors is a hybrid

representation of the electronic structure in terms of orbitals that are localized in one spatial direction only, remaining extended in the others [273]. To define these hybrid Wannier functions (HWFs) for lattices of arbitrary symmetry, it is convenient to work in reduced coordinates. Consider a 2D crystal, and let $\mathbf{k} = k_1\mathbf{b}_1 + k_2\mathbf{b}_2$ and $\hat{\mathbf{r}} = \hat{x}_1\mathbf{a}_1 + \hat{x}_2\mathbf{a}_2$. Choosing $\mathbf{b}_2$ as the localization direction, the HWFs are defined as

$$|h_{k_1ln}\rangle = \frac{1}{N_2}\sum_{k_2} e^{-i2\pi k_2 l}\,|\psi_{n\mathbf{k}}\rangle\ , \tag{72}$$

where N_2 is the number of distinct values of k_2 in the BZ, and l labels cells along $\mathbf{a}_2$. The topological indices can be determined from the winding of the HWF centers

$$x_{2,k_1ln} = \langle h_{k_1ln}|\hat{x}_2|h_{k_1ln}\rangle\,; \tag{73}$$

for bulk materials, the analysis is carried out on high-symmetry BZ planes.

A different physical perspective on the HWF centers is provided by the Wilson loop, which is calculated over a closed curve $\mathcal{C}$ in k space and discretized in L points as

$$\mathcal{W}(\mathcal{C}) = \prod_{i=0}^{L-1} P^{\mathrm{occ}}_{\mathbf{k}_i} \tag{74}$$

and is a $J \times J$ matrix [286] obtained from the product of ground-state projectors $P^{\mathrm{occ}}_{\mathbf{k}_i}$. The Wilson-loop approach was first developed for TR-symmetric systems and later generalized to other topological phases [287–290].

The two approaches are essentially equivalent [277]: the logarithm of the eigenvalues of the Wilson loop at a given k point correspond to a gauge-invariant set of HWFs centers, which coincide with those obtained from maximal localization [9]. Indeed, while the original implementation based on HWFs enforced parallel transport by performing singular value decomposition on each overlap matrix along the line in k space, in the Wilson loop formalism the full gauge-invariant loop $\mathcal{W}$ is diagonalized; the second approach has been found to converge a bit faster and allows studying the expectation value of the Wilson-loop eigenstates over symmetry operators [277, 283].

This hybrid-Wannier (or "Wilson-loop") scheme is implemented in `Z2Pack`, and a detailed description of the methodology can be found in [277]. In `Z2Pack`, the hybrid Wannier centers (73) are obtained from a parallel-transport construction, starting from the overlap matrices (12) [276]. The same procedure is implemented in `PythTB` and `WannierTools` for Wannier/TB Hamiltonians; the required overlaps are then taken between TB eigenstates, as in Eq. (70) above (`Z2Pack` can also operate in this mode). We remark that `Z2Pack` [277] works with both Wannier/TB Hamiltonians, and directly with first-principles engines such as `Quantum ESPRESSO` and `VASP`.

In closing, it is worth bearing in mind the different design philosophies of the three packages surveyed in this section. As already mentioned in Sec. 3.3, `PythTB` [169] was designed with TB "toy models" in mind, and to be used as a pedagogical tool; it enables the computation of several geometric and topological quantities (Berry phases and curvatures, Chern numbers, hybrid Wannier centers) as well as to generate ribbons and slabs to expose their boundary modes. Although `PythTB` can also import large Wannier models (which can be truncated internally),

the code is not optimized for speed; however, a high-performance Numba [291] implementation of `PythTB` better suited for that purpose is available [171]. `WannierTools` [172], on the other hand, is primarily designed to work with large Wannier models, and is parallelized using MPI. Its distinctive features include searching for band degeneracies, and plotting surface spectral functions. Finally, `Z2Pack` is focused on the HWF scheme; it is not primarily a "post-Wannier" code, since it can circumvent the need to use a Wannier engine by directly reading the *ab initio* overlap matrices, which can help streamline high-throughput calculations [198, 292].

While topological invariants are generally introduced for crystalline periodic systems in PBCs, there are a few scenarios that require either the use of open boundary conditions (OBCs) or the adoption of large supercells with Γ-only sampling; in both cases, standard approaches are of no avail. Relevant examples include the study of Anderson [293–295] and amorphous topological insulators [296], heterogeneous systems such as trivial/topological junctions [27], molecular dynamics simulations, and any other use case that does not fit a small primitive cell with BZ sampling. Among many other approaches (see [296] for a dedicated overview), single-point sampling [297, 298] and local markers [27, 299, 300] have been introduced to study topology for non-crystalline systems.

Thanks to the use of WFs as a basis set, these techniques can be implemented seamlessly in the same framework both for model TB (like the Haldane [265] or the Kane–Mele models [268, 269]) and *ab initio* TB, where the latter is obtained by constructing WFs on top of any electronic structure calculations including DFT, GW or DMFT (as discussed in Sec. 3.3). This strategy has been adopted by the `StraWBerryPy` code [298–301], where model or *ab initio* TB Hamiltonians are read and manipulated either through `PythTB` or `TBmodels`. This code can then calculate a few single-point and local topological invariants such as the Chern number and the $\mathbb{Z}_2$ invariant, as well as other quantum-geometrical quantities of the electronic structure that are relevant for topological materials.

3.7 Electron-phonon interactions

3.7.1 Methodology

In the past decade, we have witnessed a community-wide effort to develop advanced computational approaches and simulation tools for atomistic modeling of function-defining properties of materials. A primary focus of this ongoing research has been the accurate description of electron-phonon (e-ph) interactions from first-principles [302], as they determine many materials properties of technological interest such as electrical and thermal transport [303–320], phonon-assisted light absorption [321–323], phonon-mediated superconductivity [324–331], polaron formation [332–337], and excitonic effects [216, 338–342]. This list of references is by no means exhaustive, and it is only intended to serve as a starting point for the respective topics.

A comprehensive review of the theory of e-ph interactions in solids from the point of view of *ab initio* calculations is given by [302]. An important contribution to the e-ph problem has been recently made by [343] who have developed an *ab initio* many-body quantum theory of electrons and phonons in and out-of-equilibrium.

There is a well established formalism for computing the e-ph matrix elements from first-principles

using DFPT [166, 344–346]. Furthermore, a linear-response approach employing the GW method, named GW perturbation theory (GWPT), has recently been proposed to improve the accuracy of the DFPT e-ph matrix elements [347, 348]. However, all aforementioned materials properties are notoriously difficult to evaluate with desired accuracy using DFPT or GWPT calculations directly due to the prohibitive computational cost. To achieve numerical convergence, the e-ph matrix elements need to be computed on ultra-dense electron ($\mathbf{k}$) and phonon ($\mathbf{q}$) BZ grids with $10^6 - 10^7$ points.

Specialized numerical techniques based on Fourier interpolation of the perturbed potential [132, 349], linear interpolation [303], Wannier interpolation [324, 350–352] or atomic orbital interpolation [304, 352] of the e-ph matrix elements, and Fermi-surface harmonics representation of the e-ph matrix elements [353–355] have been developed to address this convergence problem. In particular, the interpolation of the e-ph matrix elements using MLWFs [5] introduced by [351] has proven very successful for enabling highly accurate and efficient calculations of e-ph interactions, and the approach has been implemented in a number of codes [168, 356–360]. WFs have also been used in the context of downfolding methods to calculate the Coulomb interaction via the constrained random phase approximation (cRPA) [361] and the e-ph interaction via constrained density-functional perturbation theory (cDFPT) [362–364], respectively.

We note that an alternative to the computation of the e-ph interaction with DFPT is offered by the finite displacement scheme in real space [304, 365–367]. While this approach requires large supercells to reach convergence and is adiabatic in nature [365–368], it has the advantage of being universally applicable to any functional, including hybrid or meta-GGA functionals, as well as more complicated exchange-correlation potentials, where higher-order derivatives of the functional are not readily available.

Below, we focus on the DFPT approach and outline the interpolation procedure to compute the e-ph matrix elements on ultra-dense meshes using WFs. One first determines the e-ph matrix elements in the Bloch representation using the electronic states computed with DFT on a coarse k-point grid, and the deformation potentials computed with DFPT on a coarse q-point grid. The e-ph matrix element is defined as:

$$g_{mn\nu}(\mathbf{k},\mathbf{q}) = \langle \psi_{m\mathbf{k}+\mathbf{q}} | \Delta_{\mathbf{q}\nu} V^{\mathrm{KS}} | \psi_{n\mathbf{k}} \rangle \,, \tag{75}$$

where $\psi_{n\mathbf{k}}$ and $\psi_{m\mathbf{k}+\mathbf{q}}$ are the KS wavefunctions of the initial and final Bloch states (with $\mathbf{k}$ being the electron wavevector, and n being the band index), and $\Delta_{\mathbf{q}\nu} V^{\mathrm{KS}}$ is the derivative of the self-consistent potential associated with a phonon with momentum $\mathbf{q}$ and branch index ν. The latter quantity can be obtained as:

$$\Delta_{\mathbf{q}\nu} V^{\mathrm{KS}} = \sum_{\kappa\alpha p} \left(\frac{\hbar}{2 M_\kappa \omega_{\mathbf{q}\nu}} \right)^{1/2} e^{i\mathbf{q}\cdot\mathbf{R}_p} \frac{\partial V^{\mathrm{KS}}}{\partial \tau_{\kappa\alpha p}} e_{\kappa\alpha,\mathbf{q}\nu}, \tag{76}$$

where $\mathbf{R}_p$ is the lattice vector identifying the unit cell p, $\tau_{\kappa\alpha p}$ is the position of atom κ in unit cell p in the Cartesian direction α, M_κ is the mass of atom κ, $\omega_{\mathbf{q}\nu}$ is the phonon frequency, and $e_{\kappa\alpha,\mathbf{q}\nu}$ is the eigendisplacement vector corresponding to atom κ in the Cartesian direction α for a collective phonon mode $\mathbf{q}\nu$. When choosing the electron and phonon grids in Eq. (75), it is necessary that the q-point grid for phonons is commensurate with and smaller than (or equal

to) the k-point grid for electrons in order to map the wavefunctions $\psi_{m\mathbf{k}+\mathbf{q}}$ onto $\psi_{m\mathbf{k}''+\mathbf{G}}$, where $\mathbf{k}''$ is on the coarse $\mathbf{k}$-grid and $\mathbf{G}$ is a reciprocal lattice vector.

Next, one finds the e-ph matrix elements in the Wannier representation:

$$g_{ij\kappa\alpha}(\mathbf{R}_e, \mathbf{R}_p) = \left\langle \mathbf{0}_e i \left| \frac{\partial V^{\mathrm{KS}}}{\partial \tau_{\kappa\alpha p}} \right| \mathbf{R}_e j \right\rangle, \tag{77}$$

where $\mathbf{R}_e$ and $\mathbf{R}_p$ are the Bravais lattice vectors associated to the electron and phonon WS supercells, and $|\mathbf{R}_e j\rangle$ are the MLWFs with index j and centered in the cell at $\mathbf{R}_e$. This is done by transforming the e-ph matrix elements from the coarse BZ $(\mathbf{k}, \mathbf{q})$ grids into the corresponding real-space supercells $(\mathbf{R}_e, \mathbf{R}_p)$ as:

$$\begin{aligned} g_{ij\kappa\alpha}(\mathbf{R}_e, \mathbf{R}_p) = \frac{1}{N_e N_p} \sum_{\mathbf{k},\mathbf{q}} e^{-i(\mathbf{k}\cdot\mathbf{R}_e + \mathbf{q}\cdot\mathbf{R}_p)} \\ \times \sum_{mn\nu} \left(\frac{\hbar}{2M_\kappa \omega_{\mathbf{q}\nu}} \right)^{1/2} V^{\dagger}_{\mathbf{k}+\mathbf{q},im} g_{mn\nu}(\mathbf{k}, \mathbf{q}) V_{\mathbf{k},nj} e^{*}_{\kappa\alpha,\mathbf{q}\nu}. \end{aligned} \tag{78}$$

In Eq. (78), N_e and N_p are the number of unit cells in the periodic BvK supercells corresponding to the number of k and q points on the coarse electron and phonon grids, respectively, and $V_{\mathbf{k}}$ is the Wannierization matrix introduced in Eq. (6). That matrix is provided by the Wannier engine, while $e_{\kappa\alpha,\mathbf{q}\nu}$ is obtained by diagonalizing the dynamical matrix at wavevector $\mathbf{q}$. In the same spirit as the interpolation of the Hamiltonian discussed in Sec. 3.3.1, a WS construction can be used for the interpolation of the electron–phonon matrix elements [307]. In this case, the construction is based on three quantities (two Wannier centers and one atomic position).

Finally, performing the inverse Fourier transform of Eq. (78), the e-ph matrix elements on very fine $(\mathbf{k}', \mathbf{q}')$ BZ grids are given by:

$$\begin{aligned} g_{mn\nu}(\mathbf{k}', \mathbf{q}') &= \sum_{ep} e^{i(\mathbf{k}'\cdot\mathbf{R}_e + \mathbf{q}'\cdot\mathbf{R}_p)} \sum_{ij\kappa\alpha} \left(\frac{\hbar}{2M_\kappa \omega_{\mathbf{q}'\nu}} \right) \\ &\times \mathcal{U}_{\mathbf{k}'+\mathbf{q}',mi} g_{ij\kappa\alpha}(\mathbf{R}_e, \mathbf{R}_p) \mathcal{U}^{\dagger}_{\mathbf{k}',jn} e_{\kappa\alpha,\mathbf{q}'\nu}. \end{aligned} \tag{79}$$

In this step, it is assumed that the e-ph matrix elements outside of the WS supercells defined by the initial coarse grids can be neglected. Prior to computing Eq. (79), the transformation matrices $\mathcal{U}_{\mathbf{k}',nj}$ given by Eq. (18) and the phonon eigenvectors $e_{\kappa\alpha,\mathbf{q}'\nu}$ for the new set of points $(\mathbf{k}', \mathbf{q}')$ must be found as described in [351].

The accuracy of the Wannier–Fourier interpolation approach depends on the spatial localization of the $g_{ij\kappa\alpha}(\mathbf{R}_e, \mathbf{R}_p)$ matrix elements. Eq. (77) can be seen as a hopping integral between two localized WFs, one at $\mathbf{0}_e$ and one at $\mathbf{R}_e$, due to a perturbation caused by the displacement of the atom at $\boldsymbol{\tau}_{\kappa p}$. If the e-ph interactions are short-ranged in real space, the quantity $g_{ij\kappa\alpha}(\mathbf{R}_e, \mathbf{R}_p)$ decays rapidly with $|\mathbf{R}_e|$ and $|\mathbf{R}_p|$, and it is sufficient to only compute the matrix elements on a small set of $(\mathbf{R}_e, \mathbf{R}_p)$ lattice vectors to fully capture the coupling between electrons and phonons. As discussed in [302, 351], the spatial decay is bound by the limiting cases $g_{ij\kappa\alpha}(\mathbf{R}_e, \mathbf{0}_p)$ and $g_{ij\kappa\alpha}(\mathbf{0}_e, \mathbf{R}_p)$. In the first case, the matrix element decays in the variable $\mathbf{R}_e$ at least as fast

as the MLWFs. In the second case, the matrix element decays with the variable $\mathbf{R}_p$ at the same rate as the screened Coulomb potential generated by the atomic displacements. Thus, the localization of $g_{ij\kappa\alpha}(\mathbf{R}_e, \mathbf{R}_p)$ depends strongly on the dielectric properties of the system. In metals and nonpolar semiconductors and semiconductors, the screening properties are dictated by Friedel oscillations [369] $|\mathbf{R}_p|^{-4}$ and quadrupole behavior [370] $|\mathbf{R}_p|^{-3}$, respectively. In polar materials (i.e., materials exhibiting nonzero Born effective charges), the dominant contribution to the potential is the dipole Fröhlich term [371], which is long-ranged and decays as $|\mathbf{R}_p|^{-2}$. Therefore, in the case of semiconductors and insulators, the long-range electrostatic fields arising from the nonanalytic behavior of the Coulomb potential in the long-wavelength limit ($\mathbf{q} \to 0$), and the e-ph matrix elements cannot be directly interpolated from a coarse to a fine grid using the Wannier-based interpolation approach.

To address this problem, the e-ph matrix elements are separated into short- ($\mathcal{S}$) and long- ($\mathcal{L}$) range contributions, as follows:

$$g_{mn\nu}(\mathbf{k}, \mathbf{q}) = g^{\mathcal{S}}_{mn\nu}(\mathbf{k}, \mathbf{q}) + g^{\mathcal{L},D}_{mn\nu}(\mathbf{k}, \mathbf{q}) + g^{\mathcal{L},Q}_{mn\nu}(\mathbf{k}, \mathbf{q}), \tag{80}$$

where the terms on the right-hand side are the short-range, the dipole, and the quadrupole components. This strategy allows the short-range component to be treated using the Wannier-Fourier interpolation approach described above, once the long-range components have been subtracted from the total matrix elements $g_{mn\nu}(\mathbf{k}, \mathbf{q})$. A data-driven compression technique based on a singular value decomposition of the short-range e-ph matrix elements in the Wannier basis has been recently developed and shown to significantly accelerate e-ph calculations while preserving quantitative accuracy [372].

[373] and [374] derived the analytic expression for the dipole e-ph matrix, which takes the form:

$$\begin{aligned} g^{\mathcal{L},D}_{mn\nu}(\mathbf{k}, \mathbf{q}) = i\, \frac{4\pi}{V_{\text{cell}}} \frac{e^2}{4\pi\epsilon_0} \sum_{\kappa} \left(\frac{\hbar}{2M_\kappa \omega_{\mathbf{q}\nu}} \right)^{1/2} \\ \times \sum_{\mathbf{G} \neq -\mathbf{q}} e^{-i(\mathbf{q}+\mathbf{G})\cdot\boldsymbol{\tau}_\kappa} \frac{(\mathbf{q}+\mathbf{G}) \cdot \mathbf{Z}^*_\kappa \cdot \mathbf{e}_{\kappa,\mathbf{q}\nu}}{(\mathbf{q}+\mathbf{G}) \cdot \boldsymbol{\epsilon}^\infty \cdot (\mathbf{q}+\mathbf{G})} \\ \times \sum_i V_{\mathbf{k}+\mathbf{q}+\mathbf{G},mi} V^\dagger_{\mathbf{k},in}. \end{aligned} \tag{81}$$

This term is of the order $1/\mathbf{q}$ and diverges as $\mathbf{q}$ approaches the zone center. In Eq. (81), ϵ_0 is the vacuum permittivity, $\boldsymbol{\epsilon}^\infty$ is the high-frequency dielectric tensor of the material, $\mathbf{G}$ is a reciprocal lattice vector, and $\mathbf{Z}^*_\kappa$ is the Born effective charge tensor of the atom κ. The unitary matrix $V_\mathbf{k}$ is the Wannierization matrix introduced in Eq. (6) and comes from the overlap integral between the KS wavefunctions $\langle \psi_{m\mathbf{k}+\mathbf{q}} | e^{i\mathbf{q}\cdot\mathbf{r}} | \psi_{n\mathbf{k}} \rangle = \sum_i V_{\mathbf{k}+\mathbf{q},mi} V^\dagger_{\mathbf{k},in}$ in the $\mathbf{q} + \mathbf{G} \to 0$ limit.

The quadrupole contribution is of the order of $|\mathbf{q}|^0$, and the corresponding $g^{\mathcal{L},Q}_{mn\nu}(\mathbf{k}, \mathbf{q})$ expression was derived in [309, 312, 313, 375, 376]. In the maximally localized Wannier gauge, $g^{\mathcal{L},Q}_{mn\nu}(\mathbf{k}, \mathbf{q})$

can be written as:

$$
\begin{aligned}
g^{\mathcal{L},Q}_{mn\nu}(\mathbf{k},\mathbf{q}) = \frac{4\pi}{V_{\text{cell}}}\frac{e^2}{4\pi\epsilon_0}\sum_{\kappa\alpha}\left(\frac{\hbar}{2M_\kappa\omega_{\mathbf{q}\nu}}\right)^{1/2} \\
\times \sum_{\mathbf{G}\neq-\mathbf{q}} \frac{e^{-i(\mathbf{q}+\mathbf{G})\cdot\boldsymbol{\tau}_\kappa} e_{\kappa\alpha,\mathbf{q}\nu}}{(\mathbf{q}+\mathbf{G})\cdot\boldsymbol{\epsilon}^\infty\cdot(\mathbf{q}+\mathbf{G})} \\
\times \sum_{\beta\gamma}\Bigg[\frac{1}{2}Q_{\kappa,\alpha\beta\gamma}(q_\beta+G_\beta)(q_\gamma+G_\gamma) \\
\times \sum_i V_{\mathbf{k}+\mathbf{q}+\mathbf{G},mi}V^\dagger_{\mathbf{k},in} \\
- Z^*_{\kappa,\alpha\beta}(q_\beta+G_\beta)\sum_{ij} V_{\mathbf{k}+\mathbf{q}+\mathbf{G},mi}(q_\gamma+G_\gamma) \\
\times\Big(A^{W,\gamma}_{\mathbf{k},ij} + \langle u^{\text{W}}_{i\mathbf{k}}|V^{\text{Hxc},\mathcal{E}_\gamma}|u^{\text{W}}_{j\mathbf{k}}\rangle\Big)V^\dagger_{\mathbf{k},jn}\Bigg].
\end{aligned}
\tag{82}
$$

where $\mathbf{Q}_\kappa$ is the dynamical quadrupole tensor that can be computed using DFPT [377], $V^{\text{Hxc},\mathcal{E}_\gamma}(\mathbf{r})$ is the self-consistent potential induced by a uniform electric field $\mathcal{E}_\gamma$ along the Cartesian direction γ [312, 376], $\mathbf{A}^{\text{W}}_{\mathbf{k},ij}$ is the Berry connection introduced in Eq. (63), and $u^{\text{W}}_{j\mathbf{k}}$ is the smooth cell-periodic part of the Bloch wavefunction in the Wannier gauge ($|u^{\text{W}}_{j\mathbf{k}}\rangle = \sum_n V_{\mathbf{k},jn}\,|u_{n\mathbf{k}}\rangle$) [376].

Equations (81) and (82) are for the long-range dipole and quadrupole components of the e-ph matrix elements in 3D bulk crystals. During the past few years, several formalisms have been proposed to treat the long-range contributions in 2D materials [320, 337, 376, 378–381]. For example, a unified description of polar e-ph interactions that allows a smooth transition from 3D to 2D was developed by [381]. Their formalism reduces to the 3D approach of [373, 374], and to the 2D approach of [378, 379]. Another strategy was followed by [380] and [320, 376] who built on the general formalism for treating long-range electrostatic interactions in 2D crystals developed by [382]. Importantly, [320, 376] showed that the long-range e-ph matrix elements have a spurious dependence on the Wannier gauge that can be eliminated by including the contribution associated with the Berry connection in Eq. (82). Therefore, in order to restore the gauge covariance in the long-wavelength limit any beyond-Fröhlich Wannier approach should incorporate this term. The contribution from $V^{\text{Hxc},\boldsymbol{\mathcal{E}}}$ term, on the other hand, was found to represent less that 0.1% of the total quadrupole correction [312, 376].

3.7.2 Codes

`EPW` [168, 356, 357, 383], the first open-source code for the study of e-ph interaction using MLWFs, was publicly released in 2010 and has been distributed within the `Quantum ESPRESSO` suite [55, 384] since 2016. Several Wannier-based open-source codes exist today to compute physical properties related to e-ph interactions such as `Perturbo` [358, 385], `Phoebe` [359, 386], `elphbolt` [387, 388], and `EPIq` [360, 389]. At present, `EPW`, `Perturbo`, `Phoebe`, and `EPIq` are all interfaced with `Quantum ESPRESSO` [55] to generate the relevant first-principles input data, and use `Wannier90` [96] in standalone or library mode to compute the required quantities in the Wannier representation. `elphbolt`, on the other hand, relies on `EPW` to generate the required Wannier space information. All codes follow an overall similar workflow to compute e-ph matrix elements on fine grids, as outlined below and summarized in Fig. 10.

1. The initial step is to perform DFT calculations with `Quantum ESPRESSO` on a uniform coarse electronic $\mathbf{k}$ grid to obtain the band energies and Bloch wavefunctions. In addition, DFPT calculations with `Quantum ESPRESSO` are carried out on an irreducible coarse $\mathbf{q}$ grid to obtain the dynamical matrices and the derivatives of the self-consistent potential with respect to the phonon perturbations. `Phoebe` and `EPIq` require that the e-ph matrix elements on the coarse electron and phonon grids are also computed with `Quantum ESPRESSO` since these quantities are later passed to the two codes. `EPW` and `PERTURBO`, on the other hand, compute the e-ph matrix elements on the coarse $\mathbf{k}$ and $\mathbf{q}$ grids internally by reading the files generated from the DFT and DFPT calculations.

2. Next, one must perform a precise Wannierization of the system using `Wannier90` in standalone mode with `PERTURBO`, `Phoebe`, and `EPIq`, or in library mode with `EPW`. This step produces the MLWFs and the Wannierization matrices $V_{\mathbf{k}}$ that transform the DFT Bloch wavefunctions into MLWFs.

3. The next step is to compute the e-ph matrix elements on the coarse $\mathbf{k}$ and $\mathbf{q}$ grids in the Bloch representation and transform them, along with the electronic Hamiltonian and the dynamical matrix, from the Bloch to the Wannier representation. As noticed at point 2, `Phoebe` and `EPIq` use the e-ph matrix elements on the coarse electron and phonon grids computed directly with `Quantum ESPRESSO`.

4. The final step is to perform an inverse Fourier transform of the electronic Hamiltonian, dynamical matrix, and e-ph matrix elements from the Wannier to the Bloch representation. At this stage, the electronic eigenvalues, phonon frequencies, and e-ph matrix elements can be efficiently computed on ultra-dense $\mathbf{k}'$ and $\mathbf{q}'$ grids and further used to carry out calculations of various materials properties.

To extend the Wannier-based interpolation scheme to systems with long-range e-ph contributions, the strategy is as follows. First, the total matrix elements $g_{mn\nu}(\mathbf{k},\mathbf{q})$ are calculated on the coarse $\mathbf{k}$ and $\mathbf{q}$ grids. Second, the long-range contributions $g^{\mathcal{L},D}_{mn\nu}(\mathbf{k},\mathbf{q})$ and $g^{\mathcal{L},Q}_{mn\nu}(\mathbf{k},\mathbf{q})$ are evaluated on the same coarse grids using Eqs. (81) and (82) and subtracted from $g_{mn\nu}(\mathbf{k},\mathbf{q})$, leaving out the short-range component $g^{\mathcal{S}}_{mn\nu}(\mathbf{k},\mathbf{q})$. Third, the short-range e-ph matrix elements are interpolated to ultra-dense $\mathbf{k}'$ and $\mathbf{q}'$ grids using the standard approach based on MLWFs. Fourth, the long-range contributions are computed using Eqs. (81) and (82) on the fine $\mathbf{k}'$ and $\mathbf{q}'$ grids and added back to the short-range component to recover the total $g_{mn\nu}(\mathbf{k}',\mathbf{q}')$ matrix elements. In this last step, the Wannierization matrix $V_{\mathbf{k}}$ given by Eq. (6) is replaced with the transformation matrix $\mathcal{U}^{\dagger}_{\mathbf{k}'}$ given by Eq. (18) in Eqs. (81) and (82).

A wide range of properties can be currently computed with `EPW`, `Perturbo`, `Phoebe`, `elphbolt`, and `EPIq`. A full list of the capabilities for the released version of each code can be found on the respective website. In particular, `EPW` computes charge carrier mobility under electric and magnetic fields using BTE, phonon-mediated superconductivity using the anisotropic Migdal-Eliashberg formalism, phonon-assisted direct and indirect optical absorption using quasi-degenerate perturbation theory, small and large polarons without supercells, and zero-point renormalization and temperature dependence of band structures using WFPT [168, 383]. `EPW` also comes with the `ZG` toolkit for calculations of band structure renormalization, temperature-dependent optical spectra, temperature-dependent anharmonic phonon dispersions, and an-

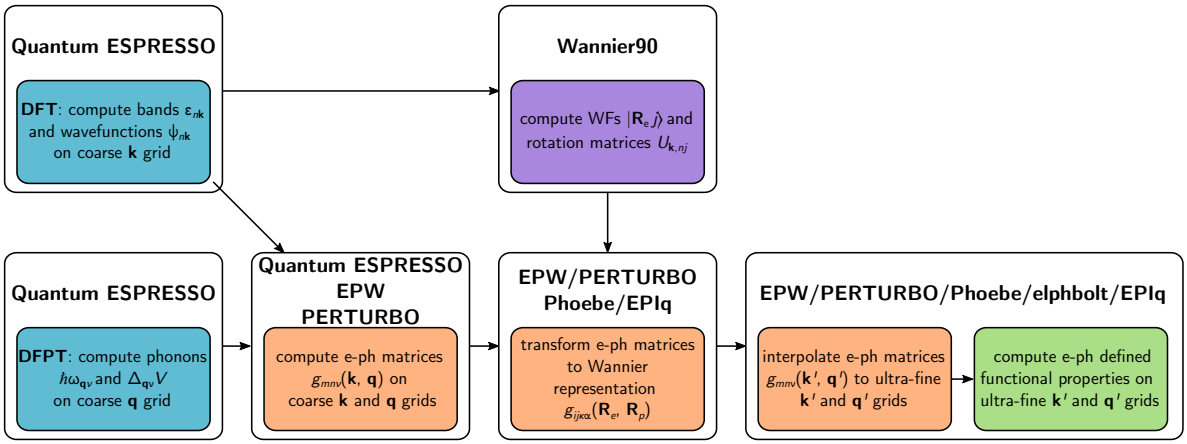

Figure 10: Workflow to compute e-ph interactions on ultra-fine grids using WFs. The user performs DFT and DFPT calculations on coarse k and q-point grids with `Quantum ESPRESSO`. Next, the user computes the e-ph matrix elements on the coarse grids and transforms them in localized Wannier basis using the rotation matrices obtained with `Wannier90`. Note that `Phoebe` and `EPIq` read the e-ph matrix elements on the coarse grids computed with `Quantum ESPRESSO`, while `EPW` and `PERTURBO` compute them internally. Finally, `EPW/PERTURBO/Phoebe/EPIq` interpolate the band structure, phonon dispersion, and e-ph matrix elements on ultra-fine k'- and q'-point grids, and perform calculations of various materials properties.

harmonic e-ph couplings via the special displacement method [390–393]. `Perturbo` calculates phonon-limited transport properties using BTE, ultrafast carrier dynamics, magnetotransport, and high-field electron transport [358, 385]. `Perturbo` is interfaced with the `TDEP` package [394] that computes temperature-dependent anharmonic phonons. `Phoebe` provides various tools to predict electron and phonon transport properties at different levels of theory and accuracy, including full scattering matrix BTE solutions such as the relaxons method and models based on the Wigner distribution [359, 386]. `elphbolt` solves the coupled electron and phonon BTEs, and the effect of the mutual e-ph drag on the electrical and thermal transport coefficients [387, 388]. `EPIq` computes phonon-mediated superconducting properties based on the Migdal-Eliashberg formalism, adiabatic and non-adiabatic phonon frequencies, double-resonant Raman intensities, and excited carriers lifetimes [360, 389]. `EPIq` is interfaced with the stochastic self-consistent harmonic approximation (SSCHA) [395–398] in order to calculate e-ph interactions in the presence of strong quantum anharmonicity.

3.8 Beyond DFT with localized orbitals

While in most cases DFT is the method of choice for electronic ground state calculations, certain excited state properties, and even the ground state properties of certain materials, may require a "beyond-DFT" treatment for accurate first-principles predictions. Two examples are finite-temperature and spectroscopic properties, as observed in direct and inverse photoemission experiments, which cannot be addressed adequately within conventional DFT. Similarly, the complex physics arising from strong local Coulomb interaction in partially filled orbitals is beyond the scope of a single-particle picture, which can manifest itself in an inaccurate description of the material. In such cases, more advanced methods are needed. One class of approaches is based on diagrammatic many-body perturbation theory; examples include the GW approximation or DMFT (see Sec. 3.8.1). Since such methods are often computationally costly and complex, it may be necessary to extract accurate low-energy effective Hamiltonians

that are treated using these methods in a post-processing step. An efficient alternative is to retain the functional character of DFT and apply physically motivated corrections, as in hybrid or Koopmans-compliant functionals (see Sec. 3.8.2). In this case the theory is no longer based on a pure functional of the density, but the orbitals themselves or their orbital densities become the key variables. Common to both approaches is the importance of improving the description of local, orbital-dependent physics. This is where WFs come in, providing a useful basis for such applications and supporting the physical understanding with chemical intuition.

3.8.1 Dynamical mean-field theory and embedding

Strongly correlated electron systems host a wide variety of physical phenomena, ranging from Mott physics to high-temperature superconductivity to exotic ordered phases [399]. Fundamental to these phenomena is the competition of itinerant versus localized character of electrons, which requires computational methods beyond the single-particle picture. While the representation of electronic states in reciprocal space can be beneficial, the theory of strong local correlations is most naturally formulated in a real-space basis. A key aspect of many beyond-DFT schemes is therefore the combination of itinerant Bloch states with localized molecular orbitals, which can be elegantly formalized with WFs [400].

Beyond-DFT schemes are typically computationally demanding and require a compromise in terms of the number of orbitals that can be treated. Starting from an *ab initio* description of a large number of bands, it is common practice to select a subset of correlated orbitals, such as those describing electronic states in the vicinity of the Fermi level, using projector functions. The result is a so-called downfolded model, which contains only the relevant degrees of freedom [401]. It divides the total system into a subspace of localized orbitals, for which a higher-level method is used, and the remaining KS states, for which the single-particle description within DFT accurately reflects the physics. The embedding *ansatz* is further justified by the observation that correlated physics phenomena typically occur on energy scales of meV to a few eV [402]. For the remainder of this subsection we focus on DMFT as the higher-level method to solve the downfolded many-body problem, but the concepts can be similarly applied to its extensions (see below) and conceptual other approaches (see, e.g., [403–406]).

While the multiband Hubbard model studied with DMFT is naturally related to TB models, a rigorous formalism based on energy functionals allows the combined approach with *ab initio* methods, as in DFT+DMFT [401]. The development of DFT+DMFT methods and software for strongly correlated materials has seen a tremendous surge in the last few decades [407–409]. Routine calculations allow to compute single-particle spectra [410–412], optical conductivity [413, 414], transport [415, 416] and thermoelectric properties [417–419], electronic Raman [420], and two-particle correlation functions (susceptibilities) [421–423]. Recent advances include interactions with core holes as in x-ray absorption and photoemission spectroscopy, and resonant inelastic x-ray scattering [424–427]. Furthermore, routines for lattice optimization [428–430] and for computing phonon spectra [431] have been formalized. This list of references is by no means exhaustive, but is intended to serve as a starting point for the respective topics.

In beyond-DFT methods, it is convenient to describe the total system of interacting electrons in a periodic solid in terms of the momentum- and frequency-dependent retarded single-particle

Green's function

$$\hat{G}(\mathbf{k},\omega) = \left[(\omega+\mu)\mathbb{1} - \hat{H}(\mathbf{k}) - \hat{\Sigma}(\mathbf{k},\omega) + i\eta\right]^{-1}, \tag{83}$$

where μ is the chemical potential and $\hat{H}(\mathbf{k})$ represents the non-interacting Hamiltonian. The frequency- and momentum-dependent electron self-energy is given by $\hat{\Sigma}(\mathbf{k},\omega)$, and η is an infinitesimal positive parameter to ensure physical correctness. For clarity, we have omitted the double-counting correction here, and we refer to [432] for an overview. Starting from a DFT-derived downfolded Hamiltonian, the challenge is to compute the corresponding self-energy correction that accounts for dynamical interaction effects. Various approaches can be formalized, but for the purpose of this review we outline the workflow of single-site DMFT [433]. In DMFT, the self-energy becomes a site-local quantity for a given atomic site $\mathcal{R}$ within the unit cell when expressed in a localized orbital basis. This approximation is conceptually similar to DFT+U [434], but in DMFT the full frequency dependence of the interaction is taken into account. Following this approach, in the DMFT self-consistency cycle, the local lattice self-energy $\Sigma^{\mathcal{R}}(\omega)$ is approximated by that of an auxiliary quantum impurity problem. The most computationally challenging step of the DMFT loop is typically to find the solution to the impurity problem, which allows a user to infer the impurity self-energy via the Dyson equation. The self-energy is embedded into the Hilbert space of the effective Hamiltonian as

$$\Sigma_{mn}(\mathbf{k},\omega) = \sum_{\mathcal{R},ij} P^{\mathcal{R}*}_{mi}(\mathbf{k})\Sigma^{\mathcal{R}}_{ij}(\omega)P^{\mathcal{R}}_{jn}(\mathbf{k})\,. \tag{84}$$

Approximating the lattice self-energy in Eq. (83) by the upfolded impurity self-energy becomes exact for infinite connectivity of the lattice [435, 436]. The projector functions $P^{\mathcal{R}}_{jn}(\mathbf{k})$ in (84) encode the basis transformation from band to orbital basis, i.e., from $|\psi_{n\mathbf{k}}\rangle$, with band index n and wavevector $\mathbf{k}$, to $|\psi^{\mathrm{W}}_{\mathcal{R}_j\mathbf{k}}\rangle$, with orbital index j at site $\mathcal{R}$ (i.e., j is an intrasite index here):

$$P^{\mathcal{R}}_{jn}(\mathbf{k}) = \langle\psi^{\mathrm{W}}_{\mathcal{R}_j\mathbf{k}}|\psi_{n\mathbf{k}}\rangle\ . \tag{85}$$

The local Green's function is then computed as $G^{\mathrm{loc},\mathcal{R}}_{ij}(\omega) = \frac{1}{N}\sum_{\mathbf{k},mn} P^{\mathcal{R}}_{im}(\mathbf{k})G_{mn}(\mathbf{k},\omega)P^{\mathcal{R}*}_{nj}(\mathbf{k})$, where N is the total number of k points of the grid. To determine a suitable localized basis set, some DFT+DMFT codes use projections on atomic orbitals, others rely on `Wannier90` directly for a simple and user-friendly interface. While the two approaches are conceptually similar (for a more detailed overview see [402]), the choice of projectors may affect the results and therefore needs to be carefully analyzed [437]. Note that Eq. (85) assumes that the DFT+DMFT calculation is performed in the band basis in a charge self-consistent mode (i.e., $P(\mathbf{k})$ corresponds to $V_{\mathbf{k}}$ in Eq. (6b)). However, for one-shot calculations, the equations simplify [438]. Wannier interpolation can be used in the DMFT self-consistent loop for an isolated set of bands or at the TB level, which is crucial for accurately resolving low-energy physics [150].

Multiple schemes go beyond standard DMFT, but the discussion above carries over directly to these extensions. Examples include cluster-DMFT approaches (either in real or reciprocal space) [401] or diagrammatic extensions of the self-energy [439], as well as non-equilibrium DMFT [440]. To improve some of the shortcomings of the DFT+DMFT method, a better starting point than DFT may be GW. The combination of GW with DMFT provides a route to include non-local effects beyond DFT as well as to formalize the double-counting correction term [441].

DFT+DMFT codes From the previous section, it becomes clear that a fully integrated DFT+DMFT software suite requires three main components: 1) a DFT implementation (*ab initio* engine) and a routine to construct the localized basis set (e.g., a Wannier engine), 2) a Green's function formalism to implement the DMFT equations, and 3) an impurity solver. At present, there are several open-source implementations that meet these requirements to varying degrees. On the side of more monolithic, publicly available beyond-DFT codes, there are implementations in, for example, `CASTEP` [442], `Abinit` [443], `RSPt` [444–446], `Amulet` [447], and `eDMFT` [448], which include an implementation of DFT and a downfolding routine, as well as choices of internal and externally linked impurity solvers. `ComDMFT` [449], on the other hand, interfaces directly with `Wannier90` for the downfolding procedure. All codes support charge self-consistency.

An alternative philosophy is a more modular library approach, focusing on providing the framework for performing DMFT calculations based on input from a DFT calculation. For this purpose, most codes directly rely on `Wannier90` to benefit from a generic, robust, and flexible interface independent of the flavor of DFT. Examples include `w2dynamics` [450] and `DCORE` [451], as well as `EDIpack` [452], `DMFTwDFT` [453], and `TRIQS` [454–456], with only the latter two packages supporting charge self-consistency at present [438, 453, 457, 458]. All packages contain a number of internal and external impurity solvers. A list of all currently available impurity solvers is beyond the scope of this article, but can be found on the respective websites.

Interaction-parameters codes As in DFT+U, the local interaction parameters that enter the Hubbard model in DFT+DMFT must be chosen appropriately. Starting from a local basis set, the Coulomb integrals can be evaluated, ideally taking into account screening processes and the symmetries of the system to simplify the parametrization of the interaction Hamiltonian [402]. The most widely used approach is the constrained random phase approximation (cRPA) [361]. Currently, the method is implemented in `ABINIT` [459], `SPEX` [460], `VASP` [199], and `RESPACK` [117]. The latter three offer the possibility to use WFs, which are constructed either using an internal Wannier engine or via an interface to `Wannier90` (`wan2respack` [461] in the case of `RESPACK`). The usage of WFs in cRPA has several benefits, e.g., a simplified interpretation of resulting interactions in terms of orbitals, a more compact representation, and the possibility to utilize Wannier interpolation on the Coulomb kernel (see, e.g., [462]). cRPA calculates the Coulomb interaction as a frequency-dependent response function that can be treated in extended DMFT [463], and which can also be combined with the frequency-dependent e-ph interaction [362]. Alternatively, the interaction parameters are treated as free parameters that must be adjusted to match experimental observables.

Post-processing Once the solution to the DFT+DMFT scheme is found (charge) self-consistently (see Fig. 11), converged DMFT quantities such as the self-energy, the local Green's function, or the hybridization function allow computing several physical observables in post-processing applications. Depending on the frequency domain in which the impurity solver operates, it may be necessary to use analytic continuation to obtain the self-energy in the real frequency domain [464, 465]. Such programs are often included in the respective software packages. Since the post-processing step is performed only once after convergence, and therefore does not sig-

nificantly contribute to the overall computational cost, Wannier interpolation (see Sec. 3.3) is particularly beneficial at this stage. A standard observable is the lattice or impurity spectral function, which is directly related to photoemission and absorption spectra. Most software packages provide tools for users to compute such quantities routinely. Transport tensors based on Kubo's linear response theory [466], such as optical and thermal conductivities, as well as Hall and Seebeck coefficients, can be computed using various tools, including `TRIQS/DFTTools` [455] and the `woptic` package [149]. Another option is `LinReTraCe` [467], which relies on a semi-analytical approach valid when a linear expansion of the self-energy is adequate. Tools to evaluate core level spectroscopies within different levels of approximations are available, for example, in `Quanty` [468] and `EDRIXS` [469].

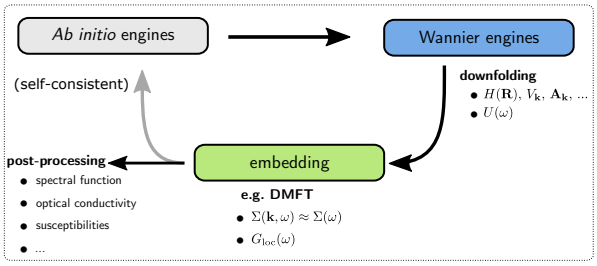

Figure 11: Typical workflow of the embedding formalism. First, the user performs an *ab initio* calculation from which a downfolded model is derived in the basis of localized orbitals. The downfolded model is solved using an appropriate many-body method such as DMFT (depicted). Physical observables can be computed in a post-processing step. For full self-consistency the cycle is iterated until convergence.

3.8.2 Koopmans functionals

Koopmans-compliant (KC) functionals [180–189] are orbital-dependent functionals capable of delivering accurate spectral properties for molecular and extended systems at low computational cost. Remarkably, the KC approach maintains a simple functional formulation while being more accurate than G_0W_0 and comparable to quasi-particle self-consistent GW with vertex correction ($QSGW\tilde{W}$) [183, 184, 187, 189], at a cost which is broadly comparable to standard DFT. The simplicity and accuracy of the KC framework rests on three fundamental concepts: linearization, screening, and localization. First, a generalized linearization condition is imposed on each charged excitation: the energy of any orbital must be independent of the occupation of the orbital itself. This implies that the KC total energy functional is piecewise linear with respect to fractional occupations, and essentially implements a generalized definition of self-interaction-free orbital. Second, electronic screening and orbital relaxation (due to the electron addition/removal process) are taken into account by orbital-dependent screening coefficients, which can be calculated by finite differences [184] or linear-response approaches [182, 187]. Finally, the Koopmans compliance condition is imposed on those variational orbitals—i.e., those minimizing the KC energy functional—which are localized. For periodic systems, these variational orbitals resemble MLWFs [182–184, 187].

Using WFs as a proxy for variational orbitals has allowed the development of a Wannier-interpolation and unfolding scheme to calculate the band structure from a supercell Koopmans-functional calculation [186]. In addition, WFs have fostered the development of a convenient Koopmans formulation that operates fully under PBCs, and is based on explicit BZ sampling

and DFPT [187, 188]. This *Koopmans-Wannier* implementation, which goes under the name of `KCW`, is available in the `Quantum ESPRESSO` distribution; it delivers improved scaling with system size, and makes band-structure calculations with Koopmans functionals straightforward [187–189]. KC functionals resonate with other efforts aimed at calculating excitation energies where WFs and localized orbitals are often a key ingredient [470–477].

3.9 Interoperability between codes in the ecosystem

3.9.1 Library mode for the Wannier engines

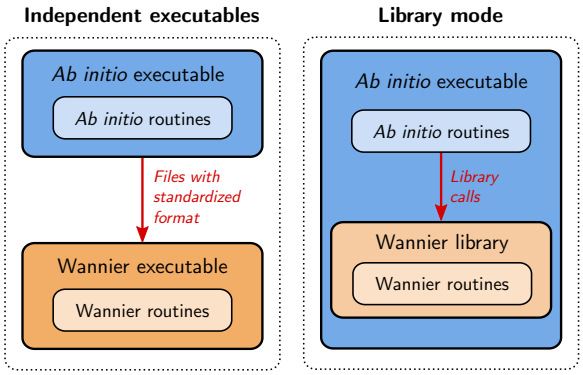

Figure 12: Different approaches for interaction of the *ab initio* codes with the library routines. Left: the *ab initio* codes and the Wannier engine are compiled independently in two different executables. Data exchange happens via files with standardized formats (see also discussion in Secs. 3.2 and 3.9.2). Right: the Wannier engine provides a library mode. The *ab initio* code is linked at compile time to the Wannier library, and a single executable is created. The *ab initio* routines call directly the routines from the Wannier engine via library calls.

When combining two (or more) codes, various approaches are possible. While the most common approach has been to compile the Wannier engine into a different executable than the *ab initio* code, with data being transferred via files with standardized formats, an alternative approach is to expose the Wannier routines via a library interface, as schematically depicted in Fig. 12. In this second approach, a single executable is created, and the main *ab initio* code is responsible for calling the appropriate routines from the Wannier-engine library.

Making sure that the library interface is both easily usable and covers all possible use cases, however, is a non-trivial task. In the specific case of `Wannier90`, for instance, its first release contained a simple interface to allow it to be called as a library from another Fortran program, with the necessary data being passed by the calling program rather than by file. Over time, however, it became apparent that this original library interface did not provide the full functionality needed by an ecosystem of codes, presenting three main issues. First, the interface was not fully compatible with parallel calling codes, because there was no means to distribute the data and make use of `Wannier90`'s internal parallelism. Second, the use of global module variables meant that `Wannier90` was not thread-safe, i.e., a calling program could not call more than one instance of `Wannier90`. The third issue concerns error handling. On detecting an error, `Wannier90` would abort, causing the calling program to crash. The desired behavior would be instead to return an error code, allowing the calling program to decide how to handle it (for instance, exiting gracefully or retrying with different parameters). Work to address all three of

these issues has been carried out by a team at the Scientific Computing Department of STFC at Daresbury Laboratory, UK, in collaboration with three of the present authors (AAM, JRY and GP). A development version is available in the `Wannier90` GitHub repository and will be merged into a future `Wannier90` release.

3.9.2 File I/O generation and parsing

In the first approach mentioned earlier, intermediate files (as listed in Tab. 1) are used to decouple the first-principles calculations from the Wannierization step. As already discussed earlier, the formats defined by `Wannier90` became the *de facto* standards for the codes in the Wannier function software ecosystem. For instance, many TB codes can read the so-called `_tb.dat` or `_hr.dat` files (as already mentioned, these contain on-site energies, hopping terms, ...) to further process the Wannier Hamiltonian. In the past few years many software packages have thus started to implement their own parsers for these I/O files, often focusing only on a specific subset of the file formats relevant for their own use case. However, this leads to a duplication of efforts, also considering that maintaining robust and feature-complete parsers is a non-trivial task. As many of these codes use Python as the programming language of choice, such as `TBmodels` [170], `PythTB` [169], `WannierBerri` [240], and `AiiDA` [478–480], a community effort has been initiated by Jamal I. Mustafa and others, to implement a centralized reference set of parsers for the `Wannier90` input/output files in Python, hosted at `https://github.com/wannier-developers/wannier90io-python/`. The goal of this project is not only to provide a parser library for developers, but also to provide a convenient package directly for users, allowing them to easily load and manipulate the `Wannier90` input/output files for their own use case. In addition, we note that part of the `Wannier90` code base already outputs Python scripts for post-processing; one example is the `berry` module, which outputs scripts using the `matplotlib` [481] library to plot the Berry curvature. However, these scripts are hard-coded into the `Wannier90` codebase as a series of `write` Fortran statements that output Python code, which makes them very difficult to update and maintain. The aforementioned Python library will also facilitate future efforts on moving these post-processing functions into a dedicated Python package, in the hope of smoothening the development experience, as well as allowing users to easily postprocess and visualize the calculation results.

The choice to support and push developments in the Python language is mostly driven by its current prevalence and adoption in the field. Indeed, for the goal of interoperability, the choice of programming language is not crucial, while it is essential to have well defined APIs or file formats. Nevertheless, providing reference implementations avoids duplication efforts in writing file writers and parsers, aiming at obtaining a robust library that can be easily reused, maintained, and where bugs can be quickly resolved. To efficiently address this goal, it is useful to select a popular language such as Python; this can also facilitate external contributions. Nevertheless, we stress that the concept of a common parsing library is not limited to the Python language, but can also be applied to other emerging languages. For example, the Julia package `WannierIO.jl` [482] provides functions to read/write `Wannier90` file formats, and is used by the `Wannier.jl` [120] and `DFTK.jl` [483] packages as their I/O backend.

3.10 Automation, workflows and high-throughput

The diversity of the software ecosystem demonstrates the effectiveness of WFs. However, all methods depend on a robust Wannierization procedure. In the past this was not a very straightforward process, since it involves a series of DFT calculations and construction of WFs, and more importantly it also depends sensitively on various input parameters (number of WFs, initial projections for MLWFs, energy windows, k-point sampling, etc.). Their selection often required experience and chemical intuition, and was often a major challenge not only for beginners, but even for experienced researchers. Fully automated Wannierizations would make the procedure straightforward, and, as a consequence, allow any researcher to easily use all capabilities of the whole ecosystem, while also enabling high-throughput studies for accelerated materials discovery. To this end, it became urgent and necessary to perform algorithmic developments on the Wannierization itself, and to implement robust workflows combining multiple software packages in the ecosystem. On the algorithmic side, Wannierization should provide well-localized WFs without user input (for initial projections or energy windows, for instance); on the workflow side, one would like to orchestrate all different steps from the initial DFT calculations to the Wannier-engine executions to the post-processing steps, while dynamically parsing the outputs and generating new inputs. Moreover, the workflow engine should provide a set of well-tested convergence parameters, and it should be able to handle common errors, and to automatically restart failed calculations. In addition, an automated Wannierization workflow should be ideally modular and composable, to allow better integration with the whole ecosystem: for instance, this has been exploited in the context of automated GW calculations with Wannier-interpolated band structures [484].

Recent development of novel algorithms have largely solved the Wannierization challenge, starting from the "selected columns of the density matrix" SCDM [59, 60, 104] algorithms, which generate initial projections by decomposing the density matrix, to the "projectability disentanglement" PDWF [61], that uses projectability thresholds on atomic orbitals, rather than energy windows, to select which states to drop, keep frozen, or throw in the disentanglement algorithm. Together with the "manifold remixing" MRWF [62] using parallel transport [106] these approaches remove what had been up to now a critical stumbling block.

On the workflow-engine side, several software packages are able to automate the electronic-structure calculations, such as `pymatgen` [485] and `FireWorks` [486], `AFLOW`π [487], `mkite` [488], `ASE` [119] and `ASR` [489], and `AiiDA` [478–480]; some of them, such as `ASE` and `AiiDA`, also provide functionalities or workflows to compute WFs. Equipped with automated Wannierization algorithms and robust workflow engines, it has become now possible to create workflows for automated Wannierizations. For instance, [103] implemented `AiiDA` workflows and gathered Wannier TB models for a group of III-V semiconductor materials; [107] used SCDM algorithm together with `AiiDA` workflows, carefully tested convergence parameters, and benchmarked Wannier interpolation accuracy on a set of 200 structures for entangled bands and a set of 81 structures for isolated bands; [490] Wannierized 1419 ferromagnetic materials with spin-orbit coupling and computed anomalous Hall/Nernst conductivities to identify high-performance transverse-thermoelectric-conversion materials; [491] created a database of Wannier Hamiltonians for 1771 materials; [57] implemented workflows in `ASE` and Wannierized 30 inorganic monolayer materi-

als using an automated protocol; and finally [61] used PDWF to automate the Wannierization, obtaining over 1.3 million MLWF for over 20,000 3D inorganics from the Materials Cloud [492] MC3D database, then using manifold remixing [62] to separately Wannierize back these into the valence and conduction bands of 77 insulators. These high-throughput studies can not only expedite materials discoveries, but also help identify challenging cases for the Wannierization algorithm, and promote further development of robust and automated Wannierization approaches.

4 Conclusions and perspectives

The Wannier function software ecosystem represents a positive model for interoperability and decentralized code development in electronic-structure simulations; a similar spirit is also found in CECAM's Electronic Structure Library [493]. This was made possible both by the nature of the scientific problem and physical quantities involved, and by the design choices originally made in `Wannier77` and `Wannier90`, planned early on as Wannierization engines decoupled from the *ab initio* codes used to compute the electronic structure. The availability of a well-documented, maintained, and modular open-source Wannier engine has pushed researchers to extend `Wannier90`'s functionalities or, when deemed more practical or efficient, to develop novel packages targeting specific materials properties. The growing availability of post-processing features has ignited a positive loop which further attracted developers from different electronic-structure domains to work and use WFs, strengthening the interest in WF-related methods and resulting in the current ecosystem of interoperable software. The ecosystem has been reinforced by the organization of coding weeks and developer workshops, that have proven to be crucial to keep the community engaged and synced, to avoid duplication of efforts, and to collaborate on code maintenance.

While we could not cover here all the existing applications and codes leveraging WFs—notably, we did not discuss their use in the calculation of magnetic interaction parameters [494–497]—we have outlined some of the most popular applications and summarized how they can be implemented in software packages and workflows to calculate advanced materials properties.

Looking forward, we expect that the ongoing efforts in the redesigned `Wannier90`'s library mode will be instrumental in smoothly integrating automated Wannierization procedures within *ab initio* and post-processing codes, with the benefit of reduced file I/O and code maintenance. As Wannierization becomes increasingly automated, we expect researchers to focus on calculations of complex properties, either through high-level programming of simulation workflows, or through the development and extension of post-processing packages. As a result, even more materials properties will become computationally accessible thanks to WFs, and available to the community through the release of dedicated functionalities, either in existing or in new packages of the ecosystem.

Finally, it is worth commenting on two crucial features of an ecosystem, being it biological or software: biodiversity and resilience. A certain level of biodiversity within a software ecosystem, i.e., the existence of multiple software packages with partially overlapping functionalities, can increase its robustness. First, it enables cross-verification of different implementations, increasing

the reliability of the results and facilitating a rapid identification of bugs. Second, it can ensure that the ecosystem capabilities are not lost if a package goes unmaintained or disappears. This aspect is connected to resilience, i.e., the capability of the ecosystem to deliver functionalities—such as the calculation of materials properties—under the loss of some of its components. This is an especially relevant issue in a scientific community where developers might not be able to guarantee long-term support for their code. We highlight that a software ecosystem might display the same dynamics that can be seen in biological settings, including competition and extinction. While a certain level of competition can result in code improvements regarding feature coverage, efficiency, and robustness, we caution that extreme competition might undermine biodiversity. It is thus important to sustain the work of individual developers who contribute to the progress and maintenance of an active, heterogeneous, and efficient ecosystem, encouraging measures to ensure proper scientific recognition. More broadly, the challenge will be to support the software development work, which is crucial for the long-term maintenance and integration of heterogeneous software packages.

We believe that a diverse, resilient, and open Wannier function software ecosystem is a major asset for the electronic-structure community in its quest to understand, discover, and design materials.

5 Acknowledgements

The authors acknowledge especially the generous and crucial support (in alphabetical order) of CCP9, CECAM, E-CAM, ICTP, IYBSSD, MaX, NCCR MARVEL, Psi-k, SISSA, STFC and University of Trieste in the organization of summer schools and developer workshops related to the Wannier function software ecosystem. Pivotal to the move to the present community model were the 2016 San Sebastián workshop, which was funded by E-CAM, NCCR MARVEL, and by the CECAM JCMaxwell node, and the 2022 ICTP Trieste Wannier Developers Meeting and Wannier Summer School, which was funded by CECAM, ICTP, IYBSSD, MaX, NCCR MARVEL, Psi-k, SISSA, and by the University of Trieste, where the present work was conceived and organized.

A.M. acknowledges support from the ICSC – Centro Nazionale di Ricerca in High Performance Computing, Big Data and Quantum Computing, funded by European Union - NextGenerationEU (CUP Grant. No. J93C22000540006, PNRR Investimento M4.C2.1.4). The views and opinions expressed are solely those of the authors and do not necessarily reflect those of the European Union, nor can the European Union be held responsible for them. S.B. acknowledges the Flatiron Institute, a division of the Simons Foundation. E.R.M. acknowledges support from the National Science Foundation under Grant No. DMR-2035518 and Grant No. OAC-2103991. N.M. acknowledges early support by the US National Science Foundation under Grant No. ASC-96-25885. N.M., G.P. and J.Q. acknowledge support from the NCCR MARVEL (a National Centre of Competence in Research, funded by the Swiss National Science Foundation, grant No. 205602). A.A.M. acknowledges the European Science Foundation INTELBIOMAT programme, and the Thomas Young Centre (grant TYC-101) for support. The work of I.S. and S.S.T. was supported by Grant No. PID2021-129035NB-I00 funded by

MCIN/AEI/10.13039/501100011033, and by the IKUR Strategy under the collaboration agreement between the Ikerbasque Foundation and the Material Physics Center on behalf of the Department of Education of the Basque Government. G.P. acknowledges support from the Swiss National Science Foundation (SNSF) Project Funding (grant 200021E_206190 "FISH4DIET"), and from the Open Research Data Program of the ETH Board (project "PREMISE": Open and Reproducible Materials Science Research).

References

[1] A. Marrazzo, S. Beck, E. R. Margine, N. Marzari, A. A. Mostofi, J. Qiao, I. Souza, S. S. Tsirkin, J. R. Yates and G. Pizzi, *The Wannier Function Software Ecosystem for Materials Simulations* (2024), `https://arxiv.org/abs/2312.10769`.

[2] A. Marrazzo, S. Beck, E. R. Margine, N. Marzari, A. A. Mostofi, J. Qiao, I. Souza, S. S. Tsirkin, J. R. Yates and G. Pizzi, *Wannier-function software ecosystem for materials simulations*, Reviews of Modern Physics **96**, 045008 (2024).

[3] G. H. Wannier, *The Structure of Electronic Excitation Levels in Insulating Crystals*, Phys. Rev. **52**, 191 (1937).

[4] N. Marzari and D. Vanderbilt, *Maximally localized generalized Wannier functions for composite energy bands*, Phys. Rev. B **56**, 12847 (1997).

[5] N. Marzari, A. A. Mostofi, J. R. Yates, I. Souza and D. Vanderbilt, *Maximally localized Wannier functions: Theory and applications*, Rev. Mod. Phys. **84**, 1419 (2012).

[6] D. Vanderbilt and R. D. King-Smith, *Electric polarization as a bulk quantity and its relation to surface charge*, Phys. Rev. B **48**, 4442 (1993).

[7] D. Xiao, J. Shi and Q. Niu, *Berry Phase Correction to Electron Density of States in Solids*, Phys. Rev. Lett. **95**, 137204 (2005).

[8] T. Thonhauser, D. Ceresoli, D. Vanderbilt and R. Resta, *Orbital Magnetization in Periodic Insulators*, Phys. Rev. Lett. **95**, 137205 (2005).

[9] A. A. Soluyanov and D. Vanderbilt, *Wannier representation of $\mathbb{Z}_2$ topological insulators*, Phys. Rev. B **83**, 035108 (2011).

[10] D. Vanderbilt, *Berry Phases in Electronic Structure Theory: Electric Polarization, Orbital Magnetization and Topological Insulators*, Cambridge University Press (2018).

[11] I. Souza, N. Marzari and D. Vanderbilt, *Maximally localized Wannier functions for entangled energy bands*, Phys. Rev. B **65**, 035109 (2001).

[12] Y.-S. Lee, M. Buongiorno Nardelli and N. Marzari, *Band Structure and Quantum Conductance of Nanostructures from Maximally Localized Wannier Functions: The Case of Functionalized Carbon Nanotubes*, Phys. Rev. Lett. **95**, 076804 (2005).

[13] J. R. Yates, X. Wang, D. Vanderbilt and I. Souza, *Spectral and Fermi surface properties from Wannier interpolation*, Phys. Rev. B **75**, 195121 (2007).

[14] C. Edmiston and K. Ruedenberg, *Localized Atomic and Molecular Orbitals*, Rev. Mod. Phys. **35**, 457 (1963).

[15] S. F. Boys, *Localized Orbitals and Localized Adjustment Functions*, in *Quantum Theory of Atoms, Molecules, and the Solid State*, edited by P.-O. Löwdin, Academic Press, New York (1966).

[16] E. I. Blount, *Formalisms of band theory*, in *Solid State Phys.*, vol. 13, p. 305, Elsevier (1962).

[17] J. Zak, *Berry's phase for energy bands in solids*, Phys. Rev. Lett. **62**, 2747 (1989).

[18] G. Nenciu, *Dynamics of band electrons in electric and magnetic fields: rigorous justification of the effective Hamiltonians*, Rev. Mod. Phys. **63**, 91 (1991).

[19] R. Resta, *Theory of the electric polarization in crystals*, Ferroelectrics **136**, 51 (1992).

[20] R. D. King-Smith and D. Vanderbilt, *Theory of polarization of crystalline solids*, Phys. Rev. B **47**, 1651 (1993).

[21] G. Panati, *Triviality of Bloch and Bloch-Dirac Bundles*, Annales Henri Poincaré **8**, 995 (2007).

[22] C. Brouder, G. Panati, M. Calandra, C. Mourougane and N. Marzari, *Exponential Localization of Wannier Functions in Insulators*, Phys. Rev. Lett. **98**, 046402 (2007).

[23] G. Panati and A. Pisante, *Bloch Bundles, Marzari-Vanderbilt Functional and Maximally Localized Wannier Functions*, Commun. Math. Phys. **322**, 835 (2013).

[24] J. Des Cloizeaux, *Analytical Properties of n-Dimensional Energy Bands and Wannier Functions*, Phys. Rev. **135**, A698 (1964).

[25] J. Des Cloizeaux, *Energy Bands and Projection Operators in a Crystal: Analytic and Asymptotic Properties*, Phys. Rev. **135**, A685 (1964).

[26] W. Kohn, *Density Functional and Density Matrix Method Scaling Linearly with the Number of Atoms*, Phys. Rev. Lett. **76**, 3168 (1996).

[27] R. Bianco and R. Resta, *Mapping topological order in coordinate space*, Phys. Rev. B **84**, 241106 (2011).

[28] R. Bianco and R. Resta, *Orbital Magnetization as a Local Property*, Phys. Rev. Lett. **110**, 087202 (2013).

[29] A. Marrazzo and R. Resta, *Irrelevance of the Boundary on the Magnetization of Metals*, Phys. Rev. Lett. **116**, 137201 (2016).

[30] A. Marrazzo and R. Resta, *Local Theory of the Insulating State*, Phys. Rev. Lett. **122**, 166602 (2019).

[31] A. Calzolari, N. Marzari, I. Souza and M. Buongiorno Nardelli, *Ab initio transport properties of nanostructures from maximally localized Wannier functions*, Phys. Rev. B **69**, 035108 (2004).

[32] F. Mauri, G. Galli and R. Car, *Orbital formulation for electronic-structure calculations with linear system-size scaling*, Phys. Rev. B **47**, 9973 (1993).

[33] P. Ordejón, D. A. Drabold, M. P. Grumbach and R. M. Martin, *Unconstrained minimization approach for electronic computations that scales linearly with system size*, Phys. Rev. B **48**, 14646 (1993).

[34] R. W. Nunes and D. Vanderbilt, *Generalization of the density-matrix method to a nonorthogonal basis*, Phys. Rev. B **50**, 17611 (1994).

[35] P. A. M. Dirac, *Quantum Mechanics of Many-Electron Systems*, Proceedings of the Royal Society of London. Series A, Containing Papers of a Mathematical and Physical Character **123**, 714 (1929).

[36] R. M. Martin, *Electronic Structure: Basic Theory and Practical Methods*, Cambridge University Press, 2 ed. (2020).

[37] F. Giustino, *Materials Modelling using Density Functional Theory*, Oxford University Press (2014).

[38] M. T. Yin and M. L. Cohen, *Microscopic Theory of the Phase Transformation and Lattice Dynamics of Si*, Phys. Rev. Lett. **45**, 1004 (1980).

[39] N. Marzari, A. Ferretti and C. Wolverton, *Electronic-structure methods for materials design*, Nature Materials **20**, 736 (2021).

[40] L. Talirz, L. M. Ghiringhelli and B. Smit, *Trends in Atomistic Simulation Software Usage [Article v1.0]*, Living Journal of Computational Molecular Science **3**, 1483 (2021).

[41] P. Anderson, *More is different*, Science **177**, 393 (1972).

[42] W. E. Pickett, *Pseudopotential methods in condensed matter applications*, Computer Physics Reports **9**, 115 (1989).

[43] R. M. Martin, *Electronic Structure: Basic Theory and Practical Methods*, Cambridge University Press (2004).

[44] F. Bloch, *Über die Quantenmechanik der Elektronen in Kristallgittern*, Zeitschrift für Physik **52**, 555 (1929).

[45] S. Kivelson, *Wannier functions in one-dimensional disordered systems: Application to fractionally charged solitons*, Phys. Rev. B **26**, 4269 (1982).

[46] J. Callaway and A. J. Hughes, *Localized Defects in Semiconductors*, Phys. Rev. **156**, 860 (1967).

[47] S. Satpathy and Z. Pawlowska, *Construction of Bond-Centered Wannier Functions for Silicon Valence Bands*, physica status solidi (b) **145**, 555 (1988).

[48] B. Sporkmann and H. Bross, *Calculation of Wannier functions for fcc transition metals by Fourier transformation of Bloch functions*, Phys. Rev. B **49**, 10869 (1994).

[49] R. J. Duffin, Duke Mathem. J. **20**, 233 (1953).

[50] J. Pipek and P. G. Mezey, *A fast intrinsic localization procedure applicable for ab initio and semiempirical linear combination of atomic orbital wave functions*, J. Chem. Phys. **90**, 4916 (1989).

[51] R. S. Mulliken, *Electronic Population Analysis on LCAO-MO Molecular Wave Functions. I*, J. Chem. Phys. **23**, 1833 (2004).

[52] E. O. Jónsson, S. Lehtola, M. Puska and H. Jónsson, *Theory and Applications of Generalized Pipek-Mezey Wannier Functions*, J. Chem. Theory Comput. **13**, 460 (2017).

[53] M. C. Clement, X. Wang and E. F. Valeev, *Robust Pipek-Mezey Orbital Localization in Periodic Solids*, J. Chem. Theory Comput. **17**, 7406 (2021).

[54] P. Giannozzi, S. Baroni, N. Bonini, M. Calandra, R. Car, C. Cavazzoni, D. Ceresoli, G. L. Chiarotti, M. Cococcioni, I. Dabo, A. D. Corso, S. de Gironcoli, S. Fabris, G. Fratesi, R. Gebauer, U. Gerstmann, C. Gougoussis, A. Kokalj, M. Lazzeri, L. Martin-Samos, N. Marzari, F. Mauri, R. Mazzarello, S. Paolini, A. Pasquarello, L. Paulatto, C. Sbraccia, S. Scandolo, G. Sclauzero, A. P. Seitsonen, A. Smogunov, P. Umari and R. M. Wentzcovitch, *QUANTUM ESPRESSO: a modular and open-source software project for quantum simulations of materials*, J. Phys.: Condens. Matter **21**, 395502 (2009).

[55] P. Giannozzi, O. Andreussi, T. Brumme, O. Bunau, M. B. Nardelli, M. Calandra, R. Car, C. Cavazzoni, D. Ceresoli, M. Cococcioni, N. Colonna, I. Carnimeo, A. D. Corso, S. de Gironcoli, P. Delugas, R. A. DiStasio, A. Ferretti, A. Floris, G. Fratesi, G. Fugallo, R. Gebauer, U. Gerstmann, F. Giustino, T. Gorni, J. Jia, M. Kawamura, H.-Y. Ko, A. Kokalj, E. Küçükbenli, M. Lazzeri, M. Marsili, N. Marzari, F. Mauri, N. L. Nguyen, H.-V. Nguyen, A. O. de-la Roza, L. Paulatto, S. Poncé, D. Rocca, R. Sabatini, B. Santra, M. Schlipf, A. P. Seitsonen, A. Smogunov, I. Timrov, T. Thonhauser, P. Umari, N. Vast, X. Wu and S. Baroni, *Advanced capabilities for materials modelling with Quantum ESPRESSO*, J. Phys.: Condens. Matter **29**, 465901 (2017).

[56] K. S. Thygesen, L. B. Hansen and K. W. Jacobsen, *Partly Occupied Wannier Functions*, Phys. Rev. Lett. **94**, 026405 (2005).

[57] P. F. Fontana, A. H. Larsen, T. Olsen and K. S. Thygesen, *Spread-balanced Wannier functions: Robust and automatable orbital localization*, Phys. Rev. B **104**, 125140 (2021).

[58] X. Qian, J. Li, L. Qi, C.-Z. Wang, T.-L. Chan, Y.-X. Yao, K.-M. Ho and S. Yip, *Quasi-atomic orbitals for ab initio tight-binding analysis*, Phys. Rev. B **78**, 245112 (2008).

[59] A. Damle, L. Lin and L. Ying, *Compressed Representation of Kohn–Sham Orbitals via Selected Columns of the Density Matrix*, J. Chem. Theory Comput. **11**, 1463 (2015).

[60] A. Damle, L. Lin and L. Ying, *SCDM-k: Localized orbitals for solids via selected columns of the density matrix*, J. Comput. Phys. **334**, 1 (2017).

[61] J. Qiao, G. Pizzi and N. Marzari, *Projectability disentanglement for accurate and automated electronic-structure Hamiltonians*, npj Comput. Mater. **9**, 208 (2023).

[62] J. Qiao, G. Pizzi and N. Marzari, *Automated mixing of maximally localized Wannier functions into target manifolds*, npj Comput. Mater. **9**, 206 (2023).

[63] M. Gibertini, G. Pizzi and N. Marzari, *Engineering polar discontinuities in honeycomb lattices*, Nat. Commun. **5**, 5157 (2014).

[64] R. Resta, *Macroscopic polarization in crystalline dielectrics: the geometric phase approach*, Rev. Mod. Phys. **66**, 899 (1994).

[65] R. Clausius, Die Mechanische Behandlung der Electrica (1879).

[66] O. F. Mossotti, Memorie di Matematica e di Fisica della Società Italiana delle Scienze Residente in Modena **24** (1850).

[67] J. P. Provost and G. Vallee, *Riemannian structure on manifolds of quantum states*, Commun. Math. Phys. **76**, 289 (1980).

[68] T. Thonhauser and D. Vanderbilt, *Insulator/Chern-insulator transition in the Haldane model*, Phys. Rev. B **74**, 235111 (2006).

[69] B. Bernevig and T. Hughes, *Topological Insulators and Topological Superconductors*, Princeton University Press (2013).

[70] J. Zak, *Band representations of space groups*, Phys. Rev. B **26**, 3010 (1982).

[71] L. Michel and J. Zak, *Connectivity of energy bands in crystals*, Phys. Rev. B **59**, 5998 (1999).

[72] B. Bradlyn, L. Elcoro, J. Cano, M. G. Vergniory, Z. Wang, C. Felser, M. I. Aroyo and B. A. Bernevig, *Topological quantum chemistry*, Nature **547**, 298 (2017).

[73] M. G. Vergniory, L. Elcoro, Z. Wang, J. Cano, C. Felser, M. I. Aroyo, B. A. Bernevig and B. Bradlyn, *Graph theory data for topological quantum chemistry*, Phys. Rev. E **96** (2017).

[74] J. Cano, B. Bradlyn, Z. Wang, L. Elcoro, M. G. Vergniory, C. Felser, M. I. Aroyo and B. A. Bernevig, *Building blocks of topological quantum chemistry: Elementary band representations*, Phys. Rev. B **97**, 035139 (2018).

[75] H. C. Po, A. Vishwanath and H. Watanabe, *Symmetry-based indicators of band topology in the 230 space groups*, Nat. Commun. **8** (2017).

[76] E. Khalaf, H. C. Po, A. Vishwanath and H. Watanabe, *Symmetry Indicators and Anomalous Surface States of Topological Crystalline Insulators*, Phys. Rev. X **8**, 031070 (2018).

[77] Z. Song, T. Zhang, Z. Fang and C. Fang, *Quantitative mappings between symmetry and topology in solids*, Nat. Commun. **9** (2018).

[78] J. Kruthoff, J. de Boer, J. van Wezel, C. L. Kane and R.-J. Slager, *Topological Classification of Crystalline Insulators through Band Structure Combinatorics*, Phys. Rev. X **7**, 041069 (2017).

[79] M. Vergniory, L. Elcoro, C. Felser, N. Regnault, B. A. Bernevig and Z. Wang, *A complete catalogue of high-quality topological materials*, Nature **566**, 480—485 (2019).

[80] T. Zhang, Y. Jiang, Z. Song, H. Huang, Y. He, Z. Fang, H. Weng and C. Fang, *Catalogue of topological electronic materials*, Nature **566**, 475 (2019).

[81] F. Tang, H. Po, A. Vishwanath and X. Wan, *Comprehensive search for topological materials using symmetry indicators*, Nature **566**, 486 (2019).

[82] B. J. Wieder, B. Bradlyn, J. Cano, Z. Wang, M. G. Vergniory, L. Elcoro, A. A. Soluyanov, C. Felser, T. Neupert, N. Regnault and B. A. Bernevig, *Topological materials discovery from crystal symmetry*, Nat. Rev. Mater. **7**, 196 (2022).

[83] A. A. Mostofi, J. R. Yates, Y.-S. Lee, I. Souza, D. Vanderbilt and N. Marzari, *Wannier90: A tool for obtaining maximally-localised Wannier functions*, Comput. Phys. Commun. **178**, 685 (2008).

[84] M. Posternak, A. Baldereschi, S. Massidda and N. Marzari, *Maximally localized Wannier functions in antiferromagnetic MnO within the FLAPW formalism*, Phys. Rev. B **65**, 184422 (2002).

[85] G. Berghold, C. J. Mundy, A. H. Romero, J. Hutter and M. Parrinello, *General and efficient algorithms for obtaining maximally localized Wannier functions*, Phys. Rev. B **61**, 10040 (2000).

[86] A. Ferretti, A. Calzolari, B. Bonferroni and R. D. Felice, *Maximally localized Wannier functions constructed from projector-augmented waves or ultrasoft pseudopotentials*, J. Phys.: Condens. Matter **19**, 036215 (2007).

[87] F. Freimuth, Y. Mokrousov, D. Wortmann, S. Heinze and S. Blügel, *Maximally localized Wannier functions within the FLAPW formalism*, Phys. Rev. B **78**, 035120 (2008).

[88] J. Kune, R. Arita, P. Wissgott, A. Toschi, H. Ikeda and K. Held, *Wien2wannier: From linearized augmented plane waves to maximally localized Wannier functions*, Comput. Phys. Commun. **181**, 1888 (2010).

[89] M. Stengel and N. A. Spaldin, *Accurate polarization within a unified Wannier function formalism*, Phys. Rev. B **73**, 075121 (2006).

[90] P. L. Silvestrelli, *Maximally localized Wannier functions for simulations with supercells of general symmetry*, Phys. Rev. B **59**, 9703 (1999).

[91] F. Gygi, J.-L. Fattebert and E. Schwegler, *Computation of Maximally Localized Wannier Functions using a simultaneous diagonalization algorithm*, Comput. Phys. Commun. **155**, 1 (2003).

[92] K. D. Stubbs, A. B. Watson and J. Lu, *Iterated projected position algorithm for constructing exponentially localized generalized Wannier functions for periodic and nonperiodic insulators in two dimensions and higher*, Phys. Rev. B **103**, 075125 (2021).

[93] R. Sakuma, *Symmetry-adapted Wannier functions in the maximal localization procedure*, Phys. Rev. B **87**, 235109 (2013).

[94] T. Koretsune, *Construction of maximally-localized Wannier functions using crystal symmetry*, Comput. Phys. Commun. **285**, 108645 (2023).

[95] R. Wang, E. A. Lazar, H. Park, A. J. Millis and C. A. Marianetti, *Selectively localized Wannier functions*, Phys. Rev. B **90**, 165125 (2014).

[96] G. Pizzi, V. Vitale, R. Arita, S. Blügel, F. Freimuth, G. Géranton, M. Gibertini, D. Gresch, C. Johnson, T. Koretsune, J. Ibañez-Azpiroz, H. Lee, J.-M. Lihm, D. Marchand, A. Marrazzo, Y. Mokrousov, J. I. Mustafa, Y. Nohara, Y. Nomura, L. Paulatto, S. Poncé, T. Ponweiser, J. Qiao, F. Thöle, S. S. Tsirkin, M. Wierzbowska, N. Marzari, D. Vanderbilt, I. Souza, A. A. Mostofi and J. R. Yates, *Wannier90 as a community code: new features and applications*, J. Phys. Condens. Matter **32**, 165902 (2020).

[97] G.-X. Zhi, C. Xu, S.-Q. Wu, F. Ning and C. Cao, *WannSymm: A symmetry analysis code for Wannier orbitals*, Computer Physics Communications **271**, 108196 (2022).

[98] A. Damle, A. Levitt and L. Lin, *Variational Formulation for Wannier Functions with Entangled Band Structure*, Multiscale Model. Simul. **17**, 167 (2019).

[99] F. Giustino and A. Pasquarello, *Mixed Wannier-Bloch Functions for Electrons and Phonons in Periodic Systems*, Phys. Rev. Lett. **96**, 216403 (2006).

[100] A. Mahler, J. Williams, N. Q. Su and W. Yang, *Localized orbital scaling correction for periodic systems*, Phys. Rev. B **106**, 035147 (2022).

[101] J. I. Mustafa, S. Coh, M. L. Cohen and S. G. Louie, *Automated construction of maximally localized Wannier functions: Optimized projection functions method*, Phys. Rev. B **92**, 165134 (2015).

[102] S. Tillack, A. Gulans and C. Draxl, *Maximally localized Wannier functions within the* (L)APW + LO *method*, Phys. Rev. B **101**, 235102 (2020).

[103] D. Gresch, Q. Wu, G. W. Winkler, R. Häuselmann, M. Troyer and A. A. Soluyanov, *Automated construction of symmetrized Wannier-like tight-binding models from ab initio calculations*, Phys. Rev. Mater. **2**, 103805 (2018).

[104] A. Damle and L. Lin, *Disentanglement via Entanglement: A Unified Method for Wannier Localization*, Multiscale Model. Simul. **16**, 1392 (2018).

[105] E. Cancès, A. Levitt, G. Panati and G. Stoltz, *Robust determination of maximally localized Wannier functions*, Phys. Rev. B **95**, 075114 (2017).

[106] D. Gontier, A. Levitt and S. Siraj-dine, *Numerical construction of Wannier functions through homotopy*, J. Math. Phys. **60**, 031901 (2019).

[107] V. Vitale, G. Pizzi, A. Marrazzo, J. R. Yates, N. Marzari and A. A. Mostofi, *Automated high-throughput Wannierisation*, npj Comput. Mater. **6**, 1 (2020).

[108] L. A. Agapito, A. Ferretti, A. Calzolari, S. Curtarolo and M. Buongiorno Nardelli, *Effective and accurate representation of extended Bloch states on finite Hilbert spaces*, Phys. Rev. B **88**, 165127 (2013).

[109] N. Marzari, D. Vanderbilt and M. C. Payne, *Ensemble Density-Functional Theory for Ab Initio Molecular Dynamics of Metals and Finite-Temperature Insulators*, Phys. Rev. Lett. **79**, 1337 (1997).

[110] S. J. Clark, M. D. Segall, C. J. Pickard, P. J. Hasnip, M. J. Probert, K. Refson and M. C. Payne, *First principles methods using CASTEP*, Zeitschrift für Kristallographie **220**, 567 (2005).

[111] J. C. A. Prentice, J. Aarons, J. C. Womack, A. E. A. Allen, L. Andrinopoulos, L. Anton, R. A. Bell, A. Bhandari, G. A. Bramley, R. J. Charlton, R. J. Clements, D. J. Cole, G. Constantinescu, F. Corsetti, S. M.-M. Dubois, K. K. B. Duff, J. M. Escartín, A. Greco, Q. Hill, L. P. Lee, E. Linscott, D. D. O'Regan, M. J. S. Phipps, L. E. Ratcliff, A. R. Serrano, E. W. Tait, G. Teobaldi, V. Vitale, N. Yeung, T. J. Zuehlsdorff, J. Dziedzic, P. D. Haynes, N. D. M. Hine, A. A. Mostofi, M. C. Payne and C.-K. Skylaris, *The ONETEP linear-scaling density functional theory program*, J. Chem. Phys. **152** (2020).

[112] A. A. Mostofi, J. R. Yates, G. Pizzi, Y.-S. Lee, I. Souza, D. Vanderbilt and N. Marzari, *An updated version of wannier90: A tool for obtaining maximally-localised Wannier functions*, Comput. Phys. Commun. **185**, 2309 (2014).

[113] J. Enkovaara, C. Rostgaard, J. J. Mortensen, J. Chen, M. Dułak, L. Ferrighi, J. Gavnholt, C. Glinsvad, V. Haikola, H. A. Hansen, H. H. Kristoffersen, M. Kuisma, A. H. Larsen, L. Lehtovaara, M. Ljungberg, O. Lopez-Acevedo, P. G. Moses, J. Ojanen, T. Olsen, V. Petzold, N. A. Romero, J. Stausholm-Møller, M. Strange, G. A. Tritsaris, M. Vanin, M. Walter, B. Hammer, H. Häkkinen, G. K. H. Madsen, R. M. Nieminen, J. K. Nørskov, M. Puska, T. T. Rantala, J. Schiøtz, K. S. Thygesen and K. W. Jacobsen, *Electronic structure calculations with GPAW: a real-space implementation of the projector augmented-wave method*, J. Phys.: Condens. Matter **22**, 253202 (2010).

[114] F. Gygi, *Architecture of Qbox: A scalable first-principles molecular dynamics code*, IBM Journal of Research and Development **52**, 137 (2008).

[115] T. D. Kühne, M. Iannuzzi, M. Del Ben, V. V. Rybkin, P. Seewald, F. Stein, T. Laino, R. Z. Khaliullin, O. Schütt, F. Schiffmann, D. Golze, J. Wilhelm, S. Chulkov, M. H. Bani-Hashemian, V. Weber, U. Borštnik, M. Taillefumier, A. S. Jakobovits, A. Lazzaro, H. Pabst, T. Müller, R. Schade, M. Guidon, S. Andermatt, N. Holmberg, G. K. Schenter, A. Hehn, A. Bussy, F. Belleflamme, G. Tabacchi, A. Glöß, M. Lass, I. Bethune, C. J. Mundy, C. Plessl, M. Watkins, J. VandeVondele, M. Krack and J. Hutter, *CP2K: An electronic structure and molecular dynamics software package - Quickstep: Efficient and accurate electronic structure calculations*, J. Chem. Phys. **152**, 194103 (2020).

[116] H. Weng, T. Ozaki and K. Terakura, *Revisiting magnetic coupling in transition-metal-benzene complexes with maximally localized Wannier functions*, Phys. Rev. B **79**, 235118 (2009).

[117] K. Nakamura, Y. Yoshimoto, Y. Nomura, T. Tadano, M. Kawamura, T. Kosugi, K. Yoshimi, T. Misawa and Y. Motoyama, *RESPACK: An ab initio tool for derivation of effective low-energy model of material*, Comput. Phys. Commun. **261**, 107781 (2021).

[118] C. M. Zicovich-Wilson, R. Dovesi and V. R. Saunders, *A general method to obtain well localized Wannier functions for composite energy bands in linear combination of atomic orbital periodic calculations*, J. Chem. Phys. **115**, 9708 (2001).

[119] A. H. Larsen, J. J. Mortensen, J. Blomqvist, I. E. Castelli, R. Christensen, M. Dułak, J. Friis, M. N. Groves, B. Hammer, C. Hargus, E. D. Hermes, P. C. Jennings, P. B. Jensen, J. Kermode, J. R. Kitchin, E. L. Kolsbjerg, J. Kubal, K. Kaasbjerg, S. Lysgaard, J. B. Maronsson, T. Maxson, T. Olsen, L. Pastewka, A. Peterson, C. Rostgaard, J. Schiøtz, O. Schütt, M. Strange, K. S. Thygesen, T. Vegge, L. Vilhelmsen, M. Walter, Z. Zeng and K. W. Jacobsen, *The atomic simulation environment—a Python library for working with atoms*, J. Phys.: Condens. Matter **29**, 273002 (2017).

[120] J. Qiao, G. Pizzi and N. Marzari, *Wannier.jl: A playground for Wannier functions*, `https://wannierjl.org` (2023), accessed on 2023-07-05.

[121] J. Bezanson, A. Edelman, S. Karpinski and V. B. Shah, *Julia: A Fresh Approach to Numerical Computing*, SIAM Review **59**, 65 (2017).

[122] L. S. Blackford, A. Petitet, R. Pozo, K. Remington, R. C. Whaley, J. Demmel, J. Dongarra, I. Duff, S. Hammarling, G. Henry *et al.*, *An updated set of basic linear algebra subprograms (BLAS)*, ACM Transactions on Mathematical Software **28**, 135 (2002).

[123] E. Anderson, Z. Bai, C. Bischof, S. Blackford, J. Demmel, J. Dongarra, J. Du Croz, A. Greenbaum, S. Hammarling, A. McKenney and D. Sorensen, *LAPACK Users' Guide*, Society for Industrial and Applied Mathematics, Philadelphia, PA, third ed. (1999).

[124] M. Frigo and S. G. Johnson, *The Design and Implementation of FFTW3*, Proceedings of the IEEE **93**, 216 (2005).

[125] R. Rew and G. Davis, *NetCDF: an interface for scientific data access*, IEEE Computer Graphics and Applications **10**, 76 (1990).

[126] The HDF Group, *2023*, `https://www.hdfgroup.org/HDF5/` (2023), accessed on 2023-12-14.

[127] K. Roberts, *The publication of scientific fortran programs*, Computer Physics Communications **1**, 1 (1969).

[128] CECAM-ESL, *The CECAM Electronic Structure Library (ESL)*, `https://esl.cecam.org` (2023), accessed on 2023-12-14.

[129] S. P. Huber, E. Bosoni, M. Bercx, J. Bröder, A. Degomme, V. Dikan, K. Eimre, E. Flage-Larsen, A. Garcia, L. Genovese, D. Gresch, C. Johnston, G. Petretto, S. Poncé, G.-M. Rignanese, C. J. Sewell, B. Smit, V. Tseplyaev, M. Uhrin, D. Wortmann, A. V. Yakutovich, A. Zadoks, P. Zarabadi-Poor, B. Zhu, N. Marzari and G. Pizzi, *Common workflows for computing material properties using different quantum engines*, npj Comput. Mater. **7**, 136 (2021).

[130] E. Bosoni, L. Beal, M. Bercx, P. Blaha, S. Blügel, J. Bröder, M. Callsen, S. Cottenier, A. Degomme, V. Dikan, K. Eimre, E. Flage-Larsen, M. Fornari, A. Garcia, L. Genovese, M. Giantomassi, S. P. Huber, H. Janssen, G. Kastlunger, M. Krack, G. Kresse, T. D. Kühne, K. Lejaeghere, G. K. H. Madsen, M. Marsman, N. Marzari, G. Michalicek, H. Mirhosseini, T. M. A. Müller, G. Petretto, C. J. Pickard, S. Poncé, G.-M. Rignanese, O. Rubel, T. Ruh, M. Sluydts, D. E. P. Vanpoucke, S. Vijay, M. Wolloch, D. Wortmann, A. V. Yakutovich, J. Yu, A. Zadoks, B. Zhu and G. Pizzi, *How to verify the precision of density-functional-theory implementations via reproducible and universal workflows*, Nat. Rev. Phys. (2023).

[131] V. Kapil, M. Rossi, O. Marsalek, R. Petraglia, Y. Litman, T. Spura, B. Cheng, A. Cuzzocrea, R. H. Meißner, D. M. Wilkins, B. A. Helfrecht, P. Juda, S. P. Bienvenue, W. Fang, J. Kessler, I. Poltavsky, S. Vandenbrande, J. Wieme, C. Corminboeuf, T. D. Kühne, D. E. Manolopoulos, T. E. Markland, J. O. Richardson, A. Tkatchenko, G. A. Tribello, V. Van Speybroeck and M. Ceriotti, *i-PI 2.0: A universal force engine for advanced molecular simulations*, Comput. Phys. Commun. **236**, 214 (2019).

[132] X. Gonze, B. Amadon, G. Antonius, F. Arnardi, L. Baguet, J.-M. Beuken, J. Bieder, F. Bottin, J. Bouchet, E. Bousquet, N. Brouwer, F. Bruneval, G. Brunin, T. Cavignac, J.-B. Charraud, W. Chen, M. Côté, S. Cottenier, J. Denier, G. Geneste, P. Ghosez, M. Giantomassi, Y. Gillet, O. Gingras, D. R. Hamann, G. Hautier, X. He, N. Helbig, N. Holzwarth, Y. Jia, F. Jollet, W. Lafargue-Dit-Hauret, K. Lejaeghere, M. A. Marques, A. Martin, C. Martins, H. P. Miranda, F. Naccarato, K. Persson, G. Petretto, V. Planes, Y. Pouillon, S. Prokhorenko, F. Ricci, G.-M. Rignanese, A. H. Romero, M. M. Schmitt, M. Torrent, M. J. van Setten, B. Van Troeye, M. J. Verstraete, G. Zérah and J. W. Zwanziger, *The Abinit project: Impact, environment and recent developments*, Comput. Phys. Commun. **248**, 107042 (2020).

[133] L. E. Ratcliff, W. Dawson, G. Fisicaro, D. Caliste, S. Mohr, A. Degomme, B. Videau, V. Cristiglio, M. Stella, M. D'Alessandro, S. Goedecker, T. Nakajima, T. Deutsch and L. Genovese, *Flexibilities of wavelets as a computational basis set for large-scale electronic structure calculations*, J. Chem. Phys. **152**, 194110 (2020).

[134] Elk, *The Elk Code*, `http://elk.sourceforge.net/` (2023).

[135] D. Wortmann, G. Michalicek, N. Baadji, M. Betzinger, G. Bihlmayer, J. Bröder, T. Burnus, J. Enkovaara, F. Freimuth, C. Friedrich, C.-R. Gerhorst, S. Granberg Cauchi, U. Grytsiuk, A. Hanke, J.-P. Hanke, M. Heide, S. Heinze, R. Hilgers, H. Janssen, D. A. Klüppelberg, R. Kovacik, P. Kurz, M. Lezaic, G. K. H. Madsen, Y. Mokrousov,

A. Neukirchen, M. Redies, S. Rost, M. Schlipf, A. Schindlmayr, M. Winkelmann and S. Blügel, *FLEUR*, Zenodo (2023).

[136] N. Tancogne-Dejean, M. J. T. Oliveira, X. Andrade, H. Appel, C. H. Borca, G. L. Breton, F. Buchholz, A. Castro, S. Corni, A. A. Correa, U. D. Giovannini, A. Delgado, F. G. Eich, J. Flick, G. Gil, A. Gomez, N. Helbig, H. Hübener, R. Jestädt, J. Jornet-Somoza, A. H. Larsen, I. V. Lebedeva, M. Lüders, M. A. L. Marques, S. T. Ohlmann, S. Pipolo, M. Rampp, C. A. Rozzi, D. A. Strubbe, S. A. Sato, C. Schäfer, I. Theophilou, A. Welden and A. Rubio, *Octopus, a computational framework for exploring light-driven phenomena and quantum dynamics in extended and finite systems*, J. Chem. Phys. **152** (2020).

[137] T. Ozaki and H. Kino, *Efficient projector expansion for the ab initio LCAO method*, Phys. Rev. B **72**, 045121 (2005).

[138] Q. Sun, T. C. Berkelbach, N. S. Blunt, G. H. Booth, S. Guo, Z. Li, J. Liu, J. D. McClain, E. R. Sayfutyarova, S. Sharma, S. Wouters and G. K.-L. Chan, *PySCF: the Python-based simulations of chemistry framework*, WIREs Computational Molecular Science **8**, e1340 (2018).

[139] Q. Sun, X. Zhang, S. Banerjee, P. Bao, M. Barbry, N. S. Blunt, N. A. Bogdanov, G. H. Booth, J. Chen, Z.-H. Cui, J. J. Eriksen, Y. Gao, S. Guo, J. Hermann, M. R. Hermes, K. Koh, P. Koval, S. Lehtola, Z. Li, J. Liu, N. Mardirossian, J. D. McClain, M. Motta, B. Mussard, H. Q. Pham, A. Pulkin, W. Purwanto, P. J. Robinson, E. Ronca, E. R. Sayfutyarova, M. Scheurer, H. F. Schurkus, J. E. T. Smith, C. Sun, S.-N. Sun, S. Upadhyay, L. K. Wagner, X. Wang, A. White, J. D. Whitfield, M. J. Williamson, S. Wouters, J. Yang, J. M. Yu, T. Zhu, T. C. Berkelbach, S. Sharma, A. Y. Sokolov and G. K.-L. Chan, *Recent developments in the PySCF program package*, J. Chem. Phys. **153**, 024109 (2020).

[140] J. M. Soler, E. Artacho, J. D. Gale, A. García, J. Junquera, P. Ordejón and D. Sánchez-Portal, *The SIESTA method for ab initio order-N materials simulation*, J. Phys.: Condens. Matter **14**, 2745 (2002).

[141] G. Kresse and D. Joubert, *From ultrasoft pseudopotentials to the projector augmented-wave method*, Phys. Rev. B **59**, 1758 (1999).

[142] P. Blaha, K. Schwarz, F. Tran, R. Laskowski, G. K. H. Madsen and L. D. Marks, *WIEN2k: An APW+lo program for calculating the properties of solids*, J. Chem. Phys. **152**, 074101 (2020).

[143] W. S. E. Registry (2024), the Wannier Software Ecosystem Registry is available at `https://wannier-developers.github.io/wannier-ecosystem-registry/`.

[144] W. S. E. Registry (2024), the GitHub repository of the Wannier Software Ecosystem Registry is available at `https://github.com/wannier-developers/wannier-ecosystem-registry`.

[145] M. Buongiorno Nardelli, F. T. Cerasoli, M. Costa, S. Curtarolo, R. De Gennaro, M. Fornari, L. Liyanage, A. R. Supka and H. Wang, *PAOFLOW: A utility to construct*

and operate on ab initio Hamiltonians from the projections of electronic wavefunctions on atomic orbital bases, including characterization of topological materials, Comput. Mater. Sci. **143**, 462 (2018).

[146] C.-C. Lee, Y.-T. Lee, M. Fukuda and T. Ozaki, *Tight-binding calculations of optical matrix elements for conductivity using nonorthogonal atomic orbitals: Anomalous Hall conductivity in bcc Fe*, Phys. Rev. B **98**, 115115 (2018).

[147] C. Wang, S. Zhao, X. Guo, X. Ren, B.-L. Gu, Y. Xu and W. Duan, *First-principles calculation of optical responses based on nonorthogonal localized orbitals*, New J. Phys. **21**, 093001 (2019).

[148] G. Jin, D. Zheng and L. He, *Calculation of Berry curvature using non-orthogonal atomic orbitals*, J. Phys.: Condens. Matter **33**, 325503 (2021).

[149] E. Assmann, P. Wissgott, J. Kuneš, A. Toschi, P. Blaha and K. Held, *woptic: Optical conductivity with Wannier functions and adaptive k-mesh refinement*, Comput. Phys. Commun. **202**, 1 (2016).

[150] J. Kaye, S. Beck, A. Barnett, L. V. Muñoz and O. Parcollet, *Automatic, high-order, and adaptive algorithms for Brillouin zone integration*, SciPost Phys. **15**, 062 (2023).

[151] L. Van Muñoz, J. Kaye, A. Barnett and S. Beck, *High-order and adaptive optical conductivity calculations using Wannier interpolation* (2024), `https://arxiv.org/abs/2406.15466`.

[152] G. K. Madsen and D. J. Singh, *BoltzTraP. A code for calculating band-structure dependent quantities*, Comput. Phys. Commun. **175**, 67 (2006).

[153] G. K. Madsen, J. Carrete and M. J. Verstraete, *BoltzTraP2, a program for interpolating band structures and calculating semi-classical transport coefficients*, Comput. Phys. Commun. **231**, 140 (2018).

[154] M. Graf and P. Vogl, *Electromagnetic fields and dielectric response in empirical tight-binding theory*, Phys. Rev. B **51**, 4940 (1995).

[155] J. Ziman, *Principles of the Theory of Solids*, Cambridge University Press, 2nd ed. (1972).

[156] W. W. Schulz, P. B. Allen and N. Trivedi, *Hall coefficient of cubic metals*, Phys. Rev. B **45**, 10886 (1992).

[157] K. Uehara and J. S. Tse, *Calculations of transport properties with the linearized augmented plane-wave method*, Phys. Rev. B **61**, 1639 (2000).

[158] G. Pizzi, D. Volja, B. Kozinsky, M. Fornari and N. Marzari, *BoltzWann: A code for the evaluation of thermoelectric and electronic transport properties with a maximally-localized Wannier functions basis*, Comput. Phys. Commun. **185**, 422 (2014).

[159] Y. Yao, L. Kleinman, A. H. MacDonald, J. Sinova, T. Jungwirth, D.-s. Wang, E. Wang and Q. Niu, *First Principles Calculation of Anomalous Hall Conductivity in Ferromagnetic bcc Fe*, Phys. Rev. Lett. **92**, 037204 (2004).

[160] I. Sodemann and L. Fu, *Quantum Nonlinear Hall Effect Induced by Berry Curvature Dipole in Time-Reversal Invariant Materials*, Phys. Rev. Lett. **115**, 216806 (2015).

[161] D. Xiao, Y. Yao, Z. Fang and Q. Niu, *Berry-Phase Effect in Anomalous Thermoelectric Transport*, Phys. Rev. Lett. **97**, 026603 (2006).

[162] Y. Gao, S. A. Yang and Q. Niu, *Intrinsic relative magnetoconductivity of nonmagnetic metals*, Phys. Rev. B **95**, 165135 (2017).

[163] T. Yokouchi, Y. Ikeda, T. Morimoto and Y. Shiomi, *Giant Magnetochiral Anisotropy in Weyl Semimetal WTe_2 Induced by Diverging Berry Curvature*, Phys. Rev. Lett. **130**, 136301 (2023).

[164] D. Xiao, M.-C. Chang and Q. Niu, *Berry phase effects on electronic properties*, Rev. Mod. Phys. **82**, 1959 (2010).

[165] Y. Gao, *Semiclassical dynamics and nonlinear charge current*, Front. Phys. **14**, 33404 (2019).

[166] S. Baroni, S. de Gironcoli, A. D. Corso and P. Giannozzi, *Phonons and related properties of extended systems from density-functional perturbation theory*, Rev. Mod. Phys. **73**, 515 (2001).

[167] J.-M. Lihm and C.-H. Park, *Wannier Function Perturbation Theory: Localized Representation and Interpolation of Wave Function Perturbation*, Phys. Rev. X **11**, 041053 (2021).

[168] H. Lee, S. Poncé, K. Bushick, S. Hajinazar, J. Lafuente-Bartolome, J. Leveillee, C. Lian, J.-M. Lihm, F. Macheda, H. Mori, H. Paudyal, W. H. Sio, S. Tiwar, M. Zacharias, X. Zhang, N. Bonini, E. Kioupakis, E. R. Margine and F. Giustino, *Electron-phonon physics from first principles using the EPW code*, npj Comput. Mater. **9**, 156 (2023).

[169] PythTB (2023), the PythTB code package is available at `http://www.physics.rutgers.edu/pythtb/about.html`.

[170] TBmodels (2023), the TBmodels code package is available at `https://tbmodels.greschd.ch/en/latest/index.html`.

[171] Numba-PythTB (2023), the high-performance Numba implementation of PythTB is available at `https://github.com/mikelgda/yeet-pythtb`.

[172] Q. Wu, S. Zhang, H.-F. Song, M. Troyer and A. A. Soluyanov, *WannierTools: An open-source software package for novel topological materials*, Comput. Phys. Commun. **224**, 405 (2018).

[173] S. Kümmel and L. Kronik, *Orbital-dependent density functionals: Theory and applications*, Rev. Mod. Phys. **80**, 3 (2008).

[174] A. D. Becke, *Perspective: Fifty years of density-functional theory in chemical physics*, J. Chem. Phys. **140**, 18A301 (2014).

[175] C. Lee, W. Yang and R. G. Parr, *Development of the Colle-Salvetti correlation-energy formula into a functional of the electron density*, Phys. Rev. B **37**, 785 (1988).

[176] A. D. Becke, *Density-functional exchange-energy approximation with correct asymptotic behavior*, Phys. Rev. A **38**, 3098 (1988).

[177] J. P. Perdew, M. Ernzerhof and K. Burke, *Rationale for mixing exact exchange with density functional approximations*, J. Chem. Phys. **105**, 9982 (1996).

[178] J. Heyd, G. E. Scuseria and M. Ernzerhof, *Hybrid functionals based on a screened Coulomb potential*, J. Chem. Phys. **118**, 8207 (2003).

[179] D. Golze, M. Dvorak and P. Rinke, *The GW Compendium: A Practical Guide to Theoretical Photoemission Spectroscopy*, Front. Chem. **7** (2019).

[180] I. Dabo, A. Ferretti, N. Poilvert, Y. Li, N. Marzari and M. Cococcioni, *Koopmans' condition for density-functional theory*, Phys. Rev. B **82**, 115121 (2010).

[181] G. Borghi, A. Ferretti, N. L. Nguyen, I. Dabo and N. Marzari, *Koopmans-compliant functionals and their performance against reference molecular data*, Phys. Rev. B **90**, 075135 (2014).

[182] N. Colonna, N. L. Nguyen, A. Ferretti and N. Marzari, *Screening in Orbital-Density-Dependent Functionals*, J. Chem. Theory Comput. **14**, 2549 (2018).

[183] N. Colonna, N. L. Nguyen, A. Ferretti and N. Marzari, *Koopmans-Compliant Functionals and Potentials and Their Application to the GW100 Test Set*, J. Chem. Theory Comput. **15**, 1905 (2019).

[184] N. L. Nguyen, N. Colonna, A. Ferretti and N. Marzari, *Koopmans-Compliant Spectral Functionals for Extended Systems*, Phys. Rev. X **8**, 021051 (2018).

[185] J. D. Elliott, N. Colonna, M. Marsili, N. Marzari and P. Umari, *Koopmans Meets Bethe–Salpeter: Excitonic Optical Spectra without GW*, J. Chem. Theory Comput. **15**, 3710 (2019).

[186] R. De Gennaro, N. Colonna, E. Linscott and N. Marzari, *Bloch's theorem in orbital-density-dependent functionals: Band structures from Koopmans spectral functionals*, Phys. Rev. B **106**, 035106 (2022).

[187] N. Colonna, R. De Gennaro, E. Linscott and N. Marzari, *Koopmans Spectral Functionals in Periodic Boundary Conditions*, J. Chem. Theory Comput. **18**, 5435 (2022).

[188] E. B. Linscott, N. Colonna, R. De Gennaro, N. L. Nguyen, G. Borghi, A. Ferretti, I. Dabo and N. Marzari, *koopmans: An Open-Source Package for Accurately and Efficiently Predicting Spectral Properties with Koopmans Functionals* **19**, 7097 (2023).

[189] A. Marrazzo and N. Colonna, *Spin-dependent interactions in orbital-density-dependent functionals: non-collinear Koopmans spectral functionals* (2024), `https://arxiv.org/abs/2402.14575`.

[190] D. Koelling and J. Wood, *On the interpolation of eigenvalues and a resultant integration scheme*, J. Comput. Phys. **67**, 253 (1986).

[191] W. E. Pickett, H. Krakauer and P. B. Allen, *Smooth Fourier interpolation of periodic functions*, Phys. Rev. B **38**, 2721 (1988).

[192] W. E, C. J. García-Cervera and J. Lu, *A sub-linear scaling algorithm for computing the electronic structure of materials*, Commun. Math. Sci. **5**, 999 (2007).

[193] X. Wu, A. Selloni and R. Car, *Order-N implementation of exact exchange in extended insulating systems*, Phys. Rev. B **79**, 085102 (2009).

[194] C. J. García-Cervera, J. Lu, Y. Xuan and W. E, *Linear-scaling subspace-iteration algorithm with optimally localized nonorthogonal wave functions for Kohn-Sham density functional theory*, Phys. Rev. B **79**, 115110 (2009).

[195] J. DiStasio, Robert A., B. Santra, Z. Li, X. Wu and R. Car, *The individual and collective effects of exact exchange and dispersion interactions on the ab initio structure of liquid water*, J. Chem. Phys. **141**, 084502 (2014).

[196] J. Mountjoy, M. Todd and N. J. Mosey, *Exact exchange with non-orthogonal generalized Wannier functions*, J. Chem. Phys. **146**, 104108 (2017).

[197] I. Carnimeo, S. Baroni and P. Giannozzi, *Fast hybrid density-functional computations using plane-wave basis sets*, Electron. Struct. **1**, 015009 (2019).

[198] A. Marrazzo, M. Gibertini, D. Campi, N. Mounet and N. Marzari, *Relative Abundance of $\mathbb{Z}_2$ Topological Order in Exfoliable Two-Dimensional Insulators*, Nano Lett. **19**, 8431 (2019).

[199] M. Kaltak, *Merging GW with DMFT*, Ph.D. thesis, University of Vienna (2015).

[200] D. Sangalli, A. Ferretti, H. Miranda, C. Attaccalite, I. Marri, E. Cannuccia, P. Melo, M. Marsili, F. Paleari, A. Marrazzo, G. Prandini, P. Bonfà, M. O. Atambo, F. Affinito, M. Palummo, A. Molina-Sánchez, C. Hogan, M. Grüning, D. Varsano and A. Marini, *Many-body perturbation theory calculations using the yambo code*, J. Phys. Condens. Matter **31**, 325902 (2019).

[201] A. Ferretti, G. Mallia, L. Martin-Samos, G. Bussi, A. Ruini, B. Montanari and N. M. Harrison, *Ab initio complex band structure of conjugated polymers: Effects of hydrid density functional theory and GW schemes*, Phys. Rev. B **85**, 235105 (2012).

[202] I. Aguilera, C. Friedrich, G. Bihlmayer and S. Blügel, *GW study of topological insulators Bi_2Se_3, Bi_2Te_3, and Sb_2Te_3: Beyond the perturbative one-shot approach*, Phys. Rev. B **88**, 045206 (2013).

[203] D. R. Hamann and D. Vanderbilt, *Maximally localized Wannier functions for GW quasiparticles*, Phys. Rev. B **79**, 045109 (2009).

[204] G. Onida, L. Reining and A. Rubio, *Electronic excitations: density-functional versus many-body Green's-function approaches*, Rev. Mod. Phys. **74**, 601 (2002).

[205] S. M. Dancoff, *Non-Adiabatic Meson Theory of Nuclear Forces*, Phys. Rev. **78**, 382 (1950).

[206] S. Hirata and M. Head-Gordon, *Time-dependent density functional theory within the Tamm–Dancoff approximation*, Chem. Phys. Lett. **314**, 291 (1999).

[207] M. Rohlfing and S. G. Louie, *Electron-hole excitations and optical spectra from first principles*, Phys. Rev. B **62**, 4927 (2000).

[208] P. Umari, X. Qian, N. Marzari, G. Stenuit, L. Giacomazzi and S. Baroni, *Accelerating GW calculations with optimal polarizability basis*, physica status solidi (b) **248**, 527 (2011).

[209] F. Giustino, M. L. Cohen and S. G. Louie, *GW method with the self-consistent Sternheimer equation*, Phys. Rev. B **81**, 115105 (2010).

[210] D. Rocca, D. Lu and G. Galli, *Ab initio calculations of optical absorption spectra: Solution of the Bethe–Salpeter equation within density matrix perturbation theory*, J. Chem. Phys. **133**, 164109 (2010).

[211] M. Marsili, E. Mosconi, F. De Angelis and P. Umari, *Large-scale GW-BSE calculations with N^3 scaling: Excitonic effects in dye-sensitized solar cells*, Phys. Rev. B **95**, 075415 (2017).

[212] B. Walker, A. M. Saitta, R. Gebauer and S. Baroni, *Efficient Approach to Time-Dependent Density-Functional Perturbation Theory for Optical Spectroscopy*, Phys. Rev. Lett. **96**, 113001 (2006).

[213] D. Rocca, R. Gebauer, Y. Saad and S. Baroni, *Turbo charging time-dependent density-functional theory with Lanczos chains*, J. Chem. Phys. **128**, 154105 (2008).

[214] A. C. Dias, J. F. Silveira and F. Qu, *WanTiBEXOS: A Wannier based Tight Binding code for electronic band structure, excitonic and optoelectronic properties of solids*, Comput. Phys. Commun. **285**, 108636 (2023).

[215] A. J. Uría-Álvarez, J. J. Esteve-Paredes, M. García-Blázquez and J. J. Palacios, *Efficient computation of optical excitations in two-dimensional materials with the Xatu code*, Computer Physics Communications **295**, 109001 (2024).

[216] J. B. Haber, D. Y. Qiu, F. H. da Jornada and J. B. Neaton, *Maximally localized exciton Wannier functions for solids*, Phys. Rev. B **108**, 125118 (2023).

[217] J.-M. Lihm and C.-H. Park, *Reliable methods for seamless stitching of tight-binding models based on maximally localized Wannier functions*, Phys. Rev. B **99**, 125117 (2019).

[218] D. H. Lee and J. D. Joannopoulos, *Simple scheme for surface-band calculations. I*, Phys. Rev. B **23**, 4988 (1981).

[219] D. H. Lee and J. D. Joannopoulos, *Simple scheme for surface-band calculations. II. The Green's function*, Phys. Rev. B **23**, 4997 (1981).

[220] M. Buongiorno Nardelli, *Electronic transport in extended systems: Application to carbon nanotubes*, Phys. Rev. B **60**, 7828 (1999).

[221] R. Landauer, *Electrical resistance of disordered one-dimensional lattices*, The Philosophical Magazine: A Journal of Theoretical Experimental and Applied Physics **21**, 863 (1970).

[222] M. P. L. Sancho, J. M. L. Sancho and J. Rubio, *Quick iterative scheme for the calculation of transfer matrices: application to Mo (100)*, J. Phys. F: Met. Phys. **14**, 1205 (1984).

[223] M. Shelley, N. Poilvert, A. A. Mostofi and N. Marzari, *Automated quantum conductance calculations using maximally-localised Wannier functions*, Comput. Phys. Commun. **182**, 2174 (2011).

[224] M. Brandbyge, J.-L. Mozos, P. Ordejón, J. Taylor and K. Stokbro, *Density-functional method for nonequilibrium electron transport*, Phys. Rev. B **65**, 165401 (2002).

[225] A. R. Rocha, V. M. García-Suárez, S. Bailey, C. Lambert, J. Ferrer and S. Sanvito, *Spin and molecular electronics in atomically generated orbital landscapes*, Phys. Rev. B **73**, 085414 (2006).

[226] T. Ozaki, K. Nishio and H. Kino, *Efficient implementation of the nonequilibrium Green function method for electronic transport calculations*, Phys. Rev. B **81**, 035116 (2010).

[227] J. E. Fonseca, T. Kubis, M. Povolotskyi, B. Novakovic, A. Ajoy, G. Hegde, H. Ilatikhameneh, Z. Jiang, P. Sengupta, Y. Tan and G. Klimeck, *Efficient and realistic device modeling from atomic detail to the nanoscale*, J. Comput. Electron. **12**, 592 (2013).

[228] K.-C. Wang, T. K. Stanev, D. Valencia, J. Charles, A. Henning, V. K. Sangwan, A. Lahiri, D. Mejia, P. Sarangapani, M. Povolotskyi, A. Afzalian, J. Maassen, G. Klimeck, M. C. Hersam, L. J. Lauhon, N. P. Stern and T. Kubis, *Control of interlayer physics in 2H transition metal dichalcogenides*, Journal of Applied Physics **122**, 224302 (2017).

[229] K.-C. Wang, D. Valencia, J. Charles, A. Henning, M. E. Beck, V. K. Sangwan, L. J. Lauhon, M. C. Hersam and T. Kubis, *Atomic-level charge transport mechanism in gate-tunable anti-ambipolar van der Waals heterojunctions*, Applied Physics Letters **118**, 083103 (2021).

[230] P. Sarangapani, J. Charles and T. Kubis, *Tuning Band Tails in Mono- and Multilayered Transition-Metal Dichalcogenides: A Detailed Assessment and a Quick-Reference Guide*, Phys. Rev. Appl. **17**, 024005 (2022).

[231] S. Birner, T. Zibold, T. Andlauer, T. Kubis, M. Sabathil, A. Trellakis and P. Vogl, *nextnano: General Purpose 3-D Simulations*, IEEE Transactions on Electron Devices **54**, 2137 (2007).

[232] G. Fiori and G. Iannaccone, *Simulation of Graphene Nanoribbon Field-Effect Transistors*, IEEE Electron Device Letters **28**, 760 (2007).

[233] S. Bruzzone, G. Iannaccone, N. Marzari and G. Fiori, *An Open-Source Multiscale Framework for the Simulation of Nanoscale Devices*, IEEE Transactions on Electron Devices **61**, 48 (2014).

[234] C. W. Groth, M. Wimmer, A. R. Akhmerov and X. Waintal, *Kwant: a software package for quantum transport*, New J. Phys. **16**, 063065 (2014).

[235] K. Thygesen and K. Jacobsen, *Molecular transport calculations with Wannier functions*, Chemical Physics **319**, 111 (2005).

[236] K. S. Thygesen and A. Rubio, *Conserving GW scheme for nonequilibrium quantum transport in molecular contacts*, Phys. Rev. B **77**, 115333 (2008).

[237] Z. Fang, N. Nagaosa, K. S. Takahashi, A. Asamitsu, R. Mathieu, T. Ogasawara, H. Yamada, M. Kawasaki, Y. Tokura and K. Terakura, *The Anomalous Hall Effect and Magnetic Monopoles in Momentum Space*, Science **302**, 92 (2003).

[238] X. Wang, J. R. Yates, I. Souza and D. Vanderbilt, *Ab initio calculation of the anomalous Hall conductivity by Wannier interpolation*, Phys. Rev. B **74**, 195118 (2006).

[239] M. G. Lopez, D. Vanderbilt, T. Thonhauser and I. Souza, *Wannier-based calculation of the orbital magnetization in crystals*, Phys. Rev. B **85**, 014435 (2012).

[240] S. S. Tsirkin, *High performance Wannier interpolation of Berry curvature and related quantities with WannierBerri code*, npj Comput. Mater. **7**, 33 (2021).

[241] J. Markel, *FFT pruning*, IEEE Transactions on Audio and Electroacoustics **19**, 305 (1971).

[242] H. Sorensen and C. Burrus, *Efficient computation of the DFT with only a subset of input or output points*, IEEE Transactions on Signal Processing **41**, 1184 (1993).

[243] dynamics-w90 (2023), the DYNAMICS-W90 code package is available at `https://github.com/michaelschueler/dynamics-w90`.

[244] J. Železný, *Linres: Wannier linear response* (2023), `https://bitbucket.org/zeleznyj/wannier-linear-response/wiki/Home`.

[245] G. Cistaro, M. Malakhov, J. J. Esteve-Paredes, A. J. Uría-Álvarez, R. E. F. Silva, F. Martín, J. J. Palacios and A. Picón, *Theoretical Approach for Electron Dynamics and Ultrafast Spectroscopy (EDUS)*, J. Chem. Theory Comput. **19**, 333 (2023).

[246] J.-M. Lihm, *Accurate calculation of Wannier centers and position matrix elements I: Translationally-invariant formula* (2022), Wannier 2022 Developers Meeting, `http://video.ictp.it/WEB/2022/2022_05_23-smr3757/2022_05_23-11_00-smr3757.mp4`.

[247] M. Ghim, *Accurate calculation of Wannier centers and position matrix elements II: Higher-order finite difference* (2022), Wannier 2022 Developers Meeting, `http://video.ictp.it/WEB/2022/2022_05_23-smr3757/2022_05_23-11_20-smr3757.mp4`.

[248] B. A. Foreman, *Consequences of local gauge symmetry in empirical tight-binding theory*, Phys. Rev. B **66**, 165212 (2002).

[249] PythTB, *PythTB tight-binding formalism and conventions*, `https://www.physics.rutgers.edu/pythtb/_downloads/e39c23ce476d399b268efa520e7a9091/pythtb-formalism.pdf` (2023), accessed: 2023-06-20.

[250] T. G. Pedersen, K. Pedersen and T. Brun Kriestensen, *Optical matrix elements in tight-binding calculations*, Phys. Rev. B **63**, 201101 (2001).

[251] J. Ibañez-Azpiroz, F. de Juan and I. Souza, *Assessing the role of interatomic position matrix elements in tight-binding calculations of optical properties*, SciPost Phys. **12**, 070 (2022).

[252] M. Schüler, J. A. Marks, Y. Murakami, C. Jia and T. P. Devereaux, *Gauge invariance of light-matter interactions in first-principle tight-binding models*, Phys. Rev. B **103**, 155409 (2021).

[253] J. Qiao, J. Zhou, Z. Yuan and W. Zhao, *Calculation of intrinsic spin Hall conductivity by Wannier interpolation*, Phys. Rev. B **98**, 214402 (2018).

[254] J. H. Ryoo, C.-H. Park and I. Souza, *Computation of intrinsic spin Hall conductivities from first principles using maximally localized Wannier functions*, Phys. Rev. B **99**, 235113 (2019).

[255] C. Aversa and J. E. Sipe, *Nonlinear optical susceptibilities of semiconductors: Results with a length-gauge analysis*, Phys. Rev. B **52**, 14636 (1995).

[256] C. Wang, X. Liu, L. Kang, B.-L. Gu, Y. Xu and W. Duan, *First-principles calculation of nonlinear optical responses by Wannier interpolation*, Phys. Rev. B **96**, 115147 (2017).

[257] J. Ibañez Azpiroz, S. S. Tsirkin and I. Souza, *Ab initio calculation of the shift photocurrent by Wannier interpolation*, Phys. Rev. B **97**, 245143 (2018).

[258] X. Liu, S. S. Tsirkin and I. Souza, *Covariant derivatives of Berry-type quantities: Application to nonlinear transport* (2023), `https://arxiv.org/abs/2303.10129`.

[259] X. Wang, D. Vanderbilt, J. R. Yates and I. Souza, *Fermi-surface calculation of the anomalous Hall conductivity*, Phys. Rev. B **76**, 195109 (2007).

[260] S. A. Nikolaev and I. V. Solovyev, *Orbital magnetization of insulating perovskite transition-metal oxides with a net ferromagnetic moment in the ground state*, Phys. Rev. B **89**, 064428 (2014).

[261] Óscar Pozo Ocaña and I. Souza, *Multipole theory of optical spatial dispersion in crystals*, SciPost Phys. **14**, 118 (2023).

[262] WannierBerri (2023), the implementation is described in the `WannierBerri` documentation available at `https://docs.wannier-berri.org/en/master/docs/mmn2uHu.html`.

[263] M. Z. Hasan and C. L. Kane, *Colloquium: Topological insulators*, Rev. Mod. Phys. **82**, 3045 (2010).

[264] J. Wang and S.-C. Zhang, *Topological states of condensed matter*, Nat. Mater. **16**, 1062 (2017).

[265] F. D. M. Haldane, *Model for a Quantum Hall Effect without Landau Levels: Condensed-Matter Realization of the "Parity Anomaly"*, Phys. Rev. Lett. **61**, 2015 (1988).

[266] T. M. Gunawardana, A. M. Turner and R. Barnett, *Optimally localized single-band Wannier functions for two-dimensional Chern insulators*, Phys. Rev. Res. **6**, 023046 (2024).

[267] A. A. Soluyanov and D. Vanderbilt, *Computing topological invariants without inversion symmetry*, Phys. Rev. B **83**, 235401 (2011).

[268] C. L. Kane and E. J. Mele, *Quantum Spin Hall Effect in Graphene*, Phys. Rev. Lett. **95**, 226801 (2005).

[269] C. L. Kane and E. J. Mele, $\mathbb{Z}_2$ *Topological Order and the Quantum Spin Hall Effect*, Phys. Rev. Lett. **95**, 146802 (2005).

[270] B. A. Bernevig and S.-C. Zhang, *Quantum Spin Hall Effect*, Phys. Rev. Lett. **96**, 106802 (2006).

[271] L. Fu, C. L. Kane and E. J. Mele, *Topological Insulators in Three Dimensions*, Phys. Rev. Lett. **98**, 106803 (2007).

[272] L. Fu, *Topological Crystalline Insulators*, Phys. Rev. Lett. **106**, 106802 (2011).

[273] C. Sgiarovello, M. Peressi and R. Resta, *Electron localization in the insulating state: Application to crystalline semiconductors*, Phys. Rev. B **64**, 115202 (2001).

[274] L. Fidkowski, T. S. Jackson and I. Klich, *Model Characterization of Gapless Edge Modes of Topological Insulators Using Intermediate Brillouin-Zone Functions*, Phys. Rev. Lett. **107**, 036601 (2011).

[275] T. Neupert and F. Schindler, *Lecture Notes on Topological Crystalline Insulators*, in *Topological Matter – Lectures from the Topological Matter School 2017*, edited by D. Bercioux, J. Cayssol, M. G. Vergniory and M. R. Calvo, chap. 2, p. 31, Springer, Cham (2018).

[276] M. Taherinejad, K. F. Garrity and D. Vanderbilt, *Wannier center sheets in topological insulators*, Phys. Rev. B **89**, 115102 (2014).

[277] D. Gresch, G. Autès, O. V. Yazyev, M. Troyer, D. Vanderbilt, B. A. Bernevig and A. A. Soluyanov, *Z2Pack: Numerical implementation of hybrid Wannier centers for identifying topological materials*, Phys. Rev. B **95**, 075146 (2017).

[278] N. Varnava, I. Souza and D. Vanderbilt, *Axion coupling in the hybrid Wannier representation*, Phys. Rev. B **101**, 155130 (2020).

[279] N. P. Armitage, E. J. Mele and A. Vishwanath, *Weyl and Dirac semimetals in three-dimensional solids*, Rev. Mod. Phys. **90**, 015001 (2018).

[280] C. Fang, M. J. Gilbert, X. Dai and B. A. Bernevig, *Multi-Weyl Topological Semimetals Stabilized by Point Group Symmetry*, Phys. Rev. Lett. **108**, 266802 (2012).

[281] S. S. Tsirkin, I. Souza and D. Vanderbilt, *Composite Weyl nodes stabilized by screw symmetry with and without time-reversal invariance*, Phys. Rev. B **96**, 045102 (2017).

[282] D. Gosálbez-Martínez, I. Souza and D. Vanderbilt, *Chiral degeneracies and Fermi-surface Chern numbers in bcc Fe*, Phys. Rev. B **92**, 085138 (2015).

[283] Z2pack (2023), the Z2Pack code package is available at `https://z2pack.greschd.ch/en/latest/index.html`.

[284] C. Fang, H. Weng, X. Dai and Z. Fang, *Topological nodal line semimetals*, Chin. Phys. B **25**, 117106 (2016).

[285] S.-Y. Yang, H. Yang, E. Derunova, S. S. P. Parkin, B. Yan and M. N. Ali, *Symmetry demanded topological nodal-line materials*, Adv. Phys.: X **3**, 1414631 (2018).

[286] R. Yu, X. L. Qi, A. Bernevig, Z. Fang and X. Dai, *Equivalent expression of $\mathbb{Z}_2$ topological invariant for band insulators using the non-Abelian Berry connection*, Phys. Rev. B **84**, 075119 (2011).

[287] A. Alexandradinata, X. Dai and B. A. Bernevig, *Wilson-loop characterization of inversion-symmetric topological insulators*, Phys. Rev. B **89**, 155114 (2014).

[288] A. Alexandradinata, C. Fang, M. J. Gilbert and B. A. Bernevig, *Spin-Orbit-Free Topological Insulators without Time-Reversal Symmetry*, Phys. Rev. Lett. **113**, 116403 (2014).

[289] A. Alexandradinata and B. A. Bernevig, *Berry-phase description of topological crystalline insulators*, Phys. Rev. B **93**, 205104 (2016).

[290] M. Taherinejad, K. F. Garrity and D. Vanderbilt, *Wannier center sheets in topological insulators*, Phys. Rev. B **89**, 115102 (2014).

[291] S. K. Lam, A. Pitrou and S. Seibert, *Numba: A LLVM-Based Python JIT Compiler*, in *Proceedings of the Second Workshop on the LLVM Compiler Infrastructure in HPC*, LLVM '15, Association for Computing Machinery, New York, NY, USA (2015).

[292] D. Grassano, D. Campi, A. Marrazzo and N. Marzari, *Complementary screening for quantum spin Hall insulators in two-dimensional exfoliable materials*, Phys. Rev. Mater. **7**, 094202 (2023).

[293] J. Li, R.-L. Chu, J. K. Jain and S.-Q. Shen, *Topological Anderson Insulator*, Phys. Rev. Lett. **102**, 136806 (2009).

[294] C. W. Groth, M. Wimmer, A. R. Akhmerov, J. Tworzydło and C. W. J. Beenakker, *Theory of the Topological Anderson Insulator*, Phys. Rev. Lett. **103**, 196805 (2009).

[295] H. Jiang, L. Wang, Q.-f. Sun and X. C. Xie, *Numerical study of the topological Anderson insulator in HgTe/CdTe quantum wells*, Phys. Rev. B **80**, 165316 (2009).

[296] P. Corbae, J. D. Hannukainen, Q. Marsal, D. Muñoz-Segovia and A. G. Grushin, *Amorphous topological matter: Theory and experiment*, Europhys. Lett. **142**, 16001 (2023).

[297] D. Ceresoli and R. Resta, *Orbital magnetization and Chern number in a supercell framework: Single* **k***-point formula*, Phys. Rev. B **76**, 012405 (2007).

[298] R. Favata and A. Marrazzo, *Single-point spin Chern number in a supercell framework*, Electron. Struct. **5**, 014005 (2023).

[299] N. Baù and A. Marrazzo, *Local Chern marker for periodic systems*, Phys. Rev. B **109**, 014206 (2024).

[300] N. Baù and A. Marrazzo, *Theory of local $\mathbb{Z}_2$ topological markers for finite and periodic two-dimensional systems* (2024), `https://arxiv.org/abs/2404.04598`.

[301] StraWBerryPy (2023), the StraWBerryPy code package is available at `https://github.com/strawberrypy-developers/strawberrypy.git`.

[302] F. Giustino, *Electron-phonon interactions from first principles*, Rev. Mod. Phys. **89**, 015003 (2017).

[303] W. Li, *Electrical transport limited by electron-phonon coupling from Boltzmann transport equation: An ab initio study of Si, Al, and MoS_2*, Phys. Rev. B **92**, 075405 (2015).

[304] T. Gunst, T. Markussen, K. Stokbro and M. Brandbyge, *First-principles method for electron-phonon coupling and electron mobility: Applications to two-dimensional materials*, Phys. Rev. B **93**, 035414 (2016).

[305] S. Poncé, E. R. Margine and F. Giustino, *Towards predictive many-body calculations of phonon-limited carrier mobilities in semiconductors*, Phys. Rev. B **97**, 121201 (2018).

[306] S. Poncé, W. Li, S. Reichardt and F. Giustino, *First-principles calculations of charge carrier mobility and conductivity in bulk semiconductors and two-dimensional materials*, Rep. Prog. Phys. **83**, 036501 (2020).

[307] S. Poncé, F. Macheda, E. R. Margine, N. Marzari, N. Bonini and F. Giustino, *First-principles predictions of Hall and drift mobilities in semiconductors*, Phys. Rev. Research **3**, 043022 (2021).

[308] N.-E. Lee, J.-J. Zhou, L. A. Agapito and M. Bernardi, *Charge transport in organic molecular semiconductors from first principles: The bandlike hole mobility in a naphthalene crystal*, Phys. Rev. B **97**, 115203 (2018).

[309] J. Park, J.-J. Zhou, V. A. Jhalani, C. E. Dreyer and M. Bernardi, *Long-range quadrupole electron-phonon interaction from first principles*, Phys. Rev. B **102**, 125203 (2020).

[310] J.-J. Zhou, J. Park, I. Timrov, A. Floris, M. Cococcioni, N. Marzari and M. Bernardi, *Ab Initio Electron-Phonon Interactions in Correlated Electron Systems*, Phys. Rev. Lett. **127**, 126404 (2021).

[311] I. Maliyov, J. Park and M. Bernardi, *Ab initio electron dynamics in high electric fields: Accurate prediction of velocity-field curves*, Phys. Rev. B **104**, L100303 (2021).

[312] G. Brunin, H. P. C. Miranda, M. Giantomassi, M. Royo, M. Stengel, M. J. Verstraete, X. Gonze, G.-M. Rignanese and G. Hautier, *Electron-Phonon beyond Fröhlich: Dynamical Quadrupoles in Polar and Covalent Solids*, Phys. Rev. Lett. **125**, 136601 (2020).

[313] G. Brunin, H. P. C. Miranda, M. Giantomassi, M. Royo, M. Stengel, M. J. Verstraete, X. Gonze, G.-M. Rignanese and G. Hautier, *Phonon-limited electron mobility in Si, GaAs, and GaP with exact treatment of dynamical quadrupoles*, Phys. Rev. B **102**, 094308 (2020).

[314] N. H. Protik and D. A. Broido, *Coupled transport of phonons and carriers in semiconductors: A case study of n-doped GaAs*, Phys. Rev. B **101**, 075202 (2020).

[315] N. H. Protik and B. Kozinsky, *Electron-phonon drag enhancement of transport properties from a fully coupled ab initio Boltzmann formalism*, Phys. Rev. B **102**, 245202 (2020).

[316] L. Cheng, C. Zhang and Y. Liu, *Why Two-Dimensional Semiconductors Generally Have Low Electron Mobility*, Phys. Rev. Lett. **125**, 177701 (2020).

[317] A. S. Chaves, A. Antonelli, D. T. Larson and E. Kaxiras, *Boosting the efficiency of ab initio electron-phonon coupling calculations through dual interpolation*, Phys. Rev. B **102**, 125116 (2020).

[318] F. Macheda and N. Bonini, *Magnetotransport phenomena in p-doped diamond from first principles*, Phys. Rev. B **98**, 201201 (2018).

[319] F. Macheda, P. Barone and F. Mauri, *Electron-Phonon Interaction and Longitudinal-Transverse Phonon Splitting in Doped Semiconductors*, Phys. Rev. Lett. **129**, 185902 (2022).

[320] S. Poncé, M. Royo, M. Gibertini, N. Marzari and M. Stengel, *Accurate Prediction of Hall Mobilities in Two-Dimensional Materials through Gauge-Covariant Quadrupolar Contributions*, Phys. Rev. Lett. **130**, 166301 (2023).

[321] J. Noffsinger, E. Kioupakis, C. G. Van de Walle, S. G. Louie and M. L. Cohen, *Phonon-Assisted Optical Absorption in Silicon from First Principles*, Phys. Rev. Lett. **108**, 167402 (2012).

[322] K. Bushick and E. Kioupakis, *Phonon-Assisted Auger-Meitner Recombination in Silicon from First Principles*, Phys. Rev. Lett. **131**, 076902 (2023).

[323] X. Zhang, G. Shi, J. A. Leveillee, F. Giustino and E. Kioupakis, *Ab initio theory of free-carrier absorption in semiconductors*, Phys. Rev. B **106**, 205203 (2022).

[324] M. Calandra, G. Profeta and F. Mauri, *Adiabatic and nonadiabatic phonon dispersion in a Wannier function approach*, Phys. Rev. B **82**, 165111 (2010).

[325] E. R. Margine and F. Giustino, *Anisotropic Migdal-Eliashberg theory using Wannier functions*, Phys. Rev. B **87**, 024505 (2013).

[326] J. Lafuente-Bartolome, I. G. Gurtubay and A. Eiguren, *Fully anisotropic superconductivity with few Helmholtz Fermi-surface harmonics*, Phys. Rev. B **102**, 161107 (2020).

[327] I. Errea, F. Belli, L. Monacelli, A. Sanna, T. Koretsune, T. Tadano, R. Bianco, M. Calandra, R. Arita, F. Mauri and J. A. Flores-Livas, *Quantum crystal structure in the 250-kelvin superconducting lanthanum hydride*, Nature **578**, 66 (2020).

[328] B. Lilia, R. Hennig, P. Hirschfeld, G. Profeta, A. Sanna, E. Zurek, W. E. Pickett, M. Amsler, R. Dias, M. I. Eremets, C. Heil, R. J. Hemley, H. Liu, Y. Ma, C. Pierleoni, A. N. Kolmogorov, N. Rybin, D. Novoselov, V. Anisimov, A. R. Oganov, C. J. Pickard, T. Bi, R. Arita, I. Errea, C. Pellegrini, R. Requist, E. K. U. Gross, E. R. Margine, S. R. Xie, Y. Quan, A. Hire, L. Fanfarillo, G. R. Stewart, J. J. Hamlin, V. Stanev, R. S. Gonnelli, E. Piatti, D. Romanin, D. Daghero and R. Valenti, *The 2021 room-temperature superconductivity roadmap*, J. Phys.: Condens. Matter **34**, 183002 (2022).

[329] C. R. Tomassetti, G. P. Kafle, E. T. Marcial, E. R. Margine and A. N. Kolmogorov, *Prospect of high-temperature superconductivity in layered metal borocarbides*, J. Mater. Chem. C **12**, 4870 (2024).

[330] R. Lucrezi, P. P. Ferreira, S. Hajinazar, H. Mori, H. Paudyal, E. R. Margine and C. Heil, *Full-bandwidth anisotropic Migdal-Eliashberg theory and its application to superhydrides*, Communications Physics **7**, 33 (2024).

[331] H. Mori, T. Nomoto, R. Arita and E. R. Margine, *Efficient anisotropic Migdal-Eliashberg calculations with the Intermediate Representation basis and Wannier interpolation* (2024), `https://arxiv.org/abs/2404.11528`.

[332] W. H. Sio, C. Verdi, S. Poncé and F. Giustino, *Polarons from First Principles, without Supercells*, Phys. Rev. Lett. **122**, 246403 (2019).

[333] J. Lafuente-Bartolome, C. Lian, W. H. Sio, I. G. Gurtubay, A. Eiguren and F. Giustino, *Unified Approach to Polarons and Phonon-Induced Band Structure Renormalization*, Phys. Rev. Lett. **129**, 076402 (2022).

[334] S. Falletta and A. Pasquarello, *Polarons free from many-body self-interaction in density functional theory*, Phys. Rev. B **106**, 125119 (2022).

[335] J.-J. Zhou and M. Bernardi, *Predicting charge transport in the presence of polarons: The beyond-quasiparticle regime in $SrTiO_3$*, Phys. Rev. Research **1**, 033138 (2019).

[336] N.-E. Lee, H.-Y. Chen, J.-J. Zhou and M. Bernardi, *Facile ab initio approach for self-localized polarons from canonical transformations*, Phys. Rev. Materials **5**, 063805 (2021).

[337] W. H. Sio and F. Giustino, *Polarons in two-dimensional atomic crystals*, Nat. Phys. **19**, 629 (2023).

[338] H.-Y. Chen, D. Sangalli and M. Bernardi, *Exciton-Phonon Interaction and Relaxation Times from First Principles*, Phys. Rev. Lett. **125**, 107401 (2020).

[339] F. Paleari and A. Marini, *Exciton-phonon interaction calls for a revision of the "exciton" concept*, Phys. Rev. B **106**, 125403 (2022).

[340] G. Antonius and S. G. Louie, *Theory of exciton-phonon coupling*, Phys. Rev. B **105**, 085111 (2022).

[341] Z. Dai, C. Lian, J. Lafuente-Bartolome and F. Giustino, *Excitonic Polarons and Self-Trapped Excitons from First-Principles Exciton-Phonon Couplings*, Phys. Rev. Lett. **132**, 036902 (2024).

[342] Z. Dai, C. Lian, J. Lafuente-Bartolome and F. Giustino, *Theory of excitonic polarons: From models to first-principles calculations*, Phys. Rev. B **109**, 045202 (2024).

[343] G. Stefanucci, R. van Leeuwen and E. Perfetto, *In and Out-of-Equilibrium Ab Initio Theory of Electrons and Phonons*, Phys. Rev. X **13**, 031026 (2023).

[344] S. Baroni, P. Giannozzi and A. Testa, *Green's-function approach to linear response in solids*, Phys. Rev. Lett. **58**, 1861 (1987).

[345] S. Y. Savrasov, *Linear response calculations of lattice dynamics using muffin-tin basis sets*, Phys. Rev. Lett. **69**, 2819 (1992).

[346] X. Gonze, *First-principles responses of solids to atomic displacements and homogeneous electric fields: Implementation of a conjugate-gradient algorithm*, Phys. Rev. B **55**, 10337 (1997).

[347] Z. Li, G. Antonius, M. Wu, F. H. da Jornada and S. G. Louie, *Electron-Phonon Coupling from Ab Initio Linear-Response Theory within the GW Method: Correlation-Enhanced Interactions and Superconductivity in* $Ba_{1-x}K_xBiO_3$, Phys. Rev. Lett. **122**, 186402 (2019).

[348] Z. Li, G. Antonius, Y.-H. Chan and S. G. Louie, *Electron-phonon coupling from GW perturbation theory: Practical workflow combining BerkeleyGW, ABINIT, and EPW*, Computer Physics Communications **295**, 109003 (2024).

[349] A. Eiguren and C. Ambrosch-Draxl, *Wannier interpolation scheme for phonon-induced potentials: Application to bulk* MgB_2*, W, and the* 1×1 *H-covered W(110) surface*, Phys. Rev. B **78**, 045124 (2008).

[350] F. Giustino, J. R. Yates, I. Souza, M. L. Cohen and S. G. Louie, *Electron-Phonon Interaction via Electronic and Lattice Wannier Functions: Superconductivity in Boron-Doped Diamond Reexamined*, Phys. Rev. Lett. **98**, 047005 (2007).

[351] F. Giustino, M. L. Cohen and S. G. Louie, *Electron-phonon interaction using Wannier functions*, Phys. Rev. B **76**, 165108 (2007).

[352] L. A. Agapito and M. Bernardi, *Ab initio electron-phonon interactions using atomic orbital wave functions*, Phys. Rev. B **97**, 235146 (2018).

[353] P. B. Allen, *Fermi-surface harmonics: A general method for nonspherical problems. Application to Boltzmann and Eliashberg equations*, Phys. Rev. B **13**, 1416 (1976).

[354] A. Eiguren and I. G. Gurtubay, *Helmholtz Fermi surface harmonics: an efficient approach for treating anisotropic problems involving Fermi surface integrals*, New J. Phys. **16**, 063014 (2014).

[355] J. Lafuente-Bartolome, I. G. Gurtubay and A. Eiguren, *Symmetric Helmholtz Fermi-surface harmonics for an optimal representation of anisotropic quantities on the Fermi surface: Application to the electron-phonon problem*, Phys. Rev. B **102**, 165113 (2020).

[356] J. Noffsinger, F. Giustino, B. D. Malone, C.-H. Park, S. G. Louie and M. L. Cohen, *EPW: A program for calculating the electron-phonon coupling using maximally localized Wannier functions*, Comput. Phys. Commun. **181**, 2140 (2010).

[357] S. Poncé, E. R. Margine, C. Verdi and F. Giustino, *EPW: Electron-phonon coupling, transport and superconducting properties using maximally localized Wannier functions*, Comput. Phys. Commun. **209**, 116 (2016).

[358] J.-J. Zhou, J. Park, I.-T. Lu, I. Maliyov, X. Tong and M. Bernardi, *PERTURBO: A software package for ab initio electron–phonon interactions, charge transport and ultrafast dynamics*, Comput. Phys. Commun. **264**, 107970 (2021).

[359] A. Cepellotti, J. Coulter, A. Johansson, N. S. Fedorova and B. Kozinsky, *Phoebe: a high-performance framework for solving phonon and electron Boltzmann transport equations*, J. Phys. Mater. **5**, 035003 (2022).

[360] G. Marini, G. Marchese, G. Profeta, J. Sjakste, F. Macheda, N. Vast, F. Mauri and M. Calandra, *EPIq: an open-source software for the calculation of electron-phonon interaction related properties*, Comput. Phys. Commun. p. 108950 (2023).

[361] F. Aryasetiawan, M. Imada, A. Georges, G. Kotliar, S. Biermann and A. I. Lichtenstein, *Frequency-dependent local interactions and low-energy effective models from electronic structure calculations*, Phys. Rev. B **70**, 195104 (2004).

[362] Y. Nomura, S. Sakai, M. Capone and R. Arita, *Unified understanding of superconductivity and Mott transition in alkali-doped fullerides from first principles*, Science Advances **1**, e1500568 (2015).

[363] J. Berges, N. Girotto, T. Wehling, N. Marzari and S. Poncé, *Phonon Self-Energy Corrections: To Screen, or Not to Screen*, Phys. Rev. X **13**, 041009 (2023).

[364] G. Giovannetti, M. Casula, P. Werner, F. Mauri and M. Capone, *Downfolding electron-phonon Hamiltonians from ab initio calculations: Application to* K_3 *picene*, Phys. Rev. B **90**, 115435 (2014).

[365] L. Chaput, A. Togo and I. Tanaka, *Finite-displacement computation of the electron-phonon interaction within the projector augmented-wave method*, Phys. Rev. B **100**, 174304 (2019).

[366] M. Engel, M. Marsman, C. Franchini and G. Kresse, *Electron-phonon interactions using the projector augmented-wave method and Wannier functions*, Phys. Rev. B **101**, 184302 (2020).

[367] M. Engel, H. Miranda, L. Chaput, A. Togo, C. Verdi, M. Marsman and G. Kresse, *Zero-point renormalization of the band gap of semiconductors and insulators using the projector augmented wave method*, Phys. Rev. B **106**, 094316 (2022).

[368] S. Poncé, Y. Gillet, J. Laflamme Janssen, A. Marini, M. Verstraete and X. Gonze, *Temperature dependence of the electronic structure of semiconductors and insulators*, J. Chem. Phys. **143**, 102813 (2015).

[369] A. L. Fetter and J. D. Walecka, *Quantum theory of many-particle systems*, Dover Publications, New York (2003).

[370] R. M. Pick, M. H. Cohen and R. M. Martin, *Microscopic Theory of Force Constants in the Adiabatic Approximation*, Phys. Rev. B **1**, 910 (1970).

[371] P. Vogl, *Microscopic theory of electron-phonon interaction in insulators or semiconductors*, Phys. Rev. B **13**, 694 (1976).

[372] Y. Luo, D. Desai, B. K. Chang, J. Park and M. Bernardi, *Data-Driven Compression of Electron-Phonon Interactions*, Phys. Rev. X **14**, 021023 (2024).

[373] C. Verdi and F. Giustino, *Fröhlich Electron-Phonon Vertex from First Principles*, Phys. Rev. Lett. **115**, 176401 (2015).

[374] J. Sjakste, N. Vast, M. Calandra and F. Mauri, *Wannier interpolation of the electron-phonon matrix elements in polar semiconductors: Polar-optical coupling in GaAs*, Phys. Rev. B **92**, 054307 (2015).

[375] V. A. Jhalani, J.-J. Zhou, J. Park, C. E. Dreyer and M. Bernardi, *Piezoelectric Electron-Phonon Interaction from Ab Initio Dynamical Quadrupoles: Impact on Charge Transport in Wurtzite GaN*, Phys. Rev. Lett. **125**, 136602 (2020).

[376] S. Poncé, M. Royo, M. Stengel, N. Marzari and M. Gibertini, *Long-range electrostatic contribution to electron-phonon couplings and mobilities of two-dimensional and bulk materials*, Phys. Rev. B **107**, 155424 (2023).

[377] M. Royo and M. Stengel, *First-Principles Theory of Spatial Dispersion: Dynamical Quadrupoles and Flexoelectricity*, Phys. Rev. X **9**, 021050 (2019).

[378] T. Sohier, M. Calandra and F. Mauri, *Two-dimensional Fröhlich interaction in transition-metal dichalcogenide monolayers: Theoretical modeling and first-principles calculations*, Phys. Rev. B **94**, 085415 (2016).

[379] T. Deng, G. Wu, W. Shi, Z. M. Wong, J.-S. Wang and S.-W. Yang, *Ab initio dipolar electron-phonon interactions in two-dimensional materials*, Phys. Rev. B **103**, 075410 (2021).

[380] C. Zhang and Y. Liu, *Phonon-limited transport of two-dimensional semiconductors: Quadrupole scattering and free carrier screening*, Phys. Rev. B **106**, 115423 (2022).

[381] W. H. Sio and F. Giustino, *Unified ab initio description of Fröhlich electron-phonon interactions in two-dimensional and three-dimensional materials*, Phys. Rev. B **105**, 115414 (2022).

[382] M. Royo and M. Stengel, *Exact Long-Range Dielectric Screening and Interatomic Force Constants in Quasi-Two-Dimensional Crystals*, Phys. Rev. X **11**, 041027 (2021).

[383] EPW, *The EPW code*, https://epw-code.org/ (2023).

[384] Quantum ESPRESSO, *The Quantum ESPRESSO suite of codes*, https://www.quantum-espresso.org (2023).

[385] PERTURBO, *The PERTURBO code*, https://perturbo-code.github.io/ (2023).

[386] Phoebe, *Phoebe, A high-performance framework for solving Phonon and Electron Boltzmann transport Equations*, https://mir-group.github.io/phoebe/ (2023).

[387] N. H. Protik, C. Li, M. Pruneda, D. Broido and P. Ordejón, *The elphbolt ab initio solver for the coupled electron-phonon Boltzmann transport equations*, npj Comput. Mater. **8**, 28 (2022).

[388] Elphbolt, *The elphbolt code*, https://github.com/nakib/elphbolt (2023).

[389] EPIq, *The EPIq code*, https://the-epiq-team.gitlab.io/epiq-site/ (2023).

[390] M. Zacharias and F. Giustino, *One-shot calculation of temperature-dependent optical spectra and phonon-induced band-gap renormalization*, Phys. Rev. B **94**, 075125 (2016).

[391] M. Zacharias and F. Giustino, *Theory of the special displacement method for electronic structure calculations at finite temperature*, Phys. Rev. Res. **2**, 013357 (2020).

[392] M. Zacharias, G. Volonakis, F. Giustino and J. Even, *Anharmonic lattice dynamics via the special displacement method*, Phys. Rev. B **108**, 035155 (2023).

[393] M. Zacharias, G. Volonakis, F. Giustino and J. Even, *Anharmonic lattice dynamics via the special displacement method*, npj Comput. Mater. **9**, 153 (2023).

[394] TDEP, *The TDEP code*, https://tdep-developers.github.io/tdep/ (2023).

[395] SSCHA, *The SSCHA code*, https://sscha.eu/ (2023).

[396] I. Errea, M. Calandra and F. Mauri, *First-Principles Theory of Anharmonicity and the Inverse Isotope Effect in Superconducting Palladium-Hydride Compounds*, Phys. Rev. Lett. **111**, 177002 (2013).

[397] I. Errea, M. Calandra and F. Mauri, *Anharmonic free energies and phonon dispersions from the stochastic self-consistent harmonic approximation: Application to platinum and palladium hydrides*, Phys. Rev. B **89**, 064302 (2014).

[398] L. Monacelli, R. Bianco, M. Cherubini, M. Calandra, I. Errea and F. Mauri, *The stochastic self-consistent harmonic approximation: calculating vibrational properties of materials with full quantum and anharmonic effects*, J. Phys. Condens. Matter **33**, 363001 (2021).

[399] Y. Tokura, M. Kawasaki and N. Nagaosa, *Emergent functions of quantum materials*, Nat. Phys. **13**, 1056 (2017).

[400] F. Lechermann, A. Georges, A. Poteryaev, S. Biermann, M. Posternak, A. Yamasaki and O. K. Andersen, *Dynamical mean-field theory using Wannier functions: A flexible route to electronic structure calculations of strongly correlated materials*, Phys. Rev. B **74**, 125120 (2006).

[401] G. Kotliar, S. Y. Savrasov, K. Haule, V. S. Oudovenko, O. Parcollet and C. A. Marianetti, *Electronic structure calculations with dynamical mean-field theory*, Rev. Mod. Phys. **78**, 865 (2006).

[402] H. Chen, A. Hampel, J. Karp, F. Lechermann and A. J. Millis, *Dynamical Mean Field Studies of Infinite Layer Nickelates: Physics Results and Methodological Implications*, Front. Phys. **10** (2022).

[403] D. Zgid and E. Gull, *Finite temperature quantum embedding theories for correlated systems*, New Journal of Physics **19**, 023047 (2017).

[404] B. Eskridge, H. Krakauer and S. Zhang, *Local Embedding and Effective Downfolding in the Auxiliary-Field Quantum Monte Carlo Method*, Journal of Chemical Theory and Computation **15**, 3949 (2019).

[405] N. Sheng, C. Vorwerk, M. Govoni and G. Galli, *Green's Function Formulation of Quantum Defect Embedding Theory*, Journal of Chemical Theory and Computation **18**, 3512 (2022).

[406] L. Muechler, D. I. Badrtdinov, A. Hampel, J. Cano, M. Rösner and C. E. Dreyer, *Quantum embedding methods for correlated excited states of point defects: Case studies and challenges*, Phys. Rev. B **105**, 235104 (2022).

[407] K. Held, *Electronic structure calculations using dynamical mean field theory*, Advances in Physics **56**, 829 (2007).

[408] E. Pavarini, E. Koch, A. Lichtenstein and D. Vollhardt (Editors), *The LDA+DMFT approach to strongly correlated materials*, *Schriften des Forschungszentrums Jülich. Reihe modeling and simulation*, vol. 1, Forschungszenrum Jülich GmbH Zentralbibliothek, Verlag, Jülich (2011), record converted from VDB: 12.11.2012.

[409] A. Paul and T. Birol, *Applications of DFT + DMFT in Materials Science*, Annual Review of Materials Research **49**, 31 (2019).

[410] E. Pavarini, S. Biermann, A. Poteryaev, A. I. Lichtenstein, A. Georges and O. K. Andersen, *Mott Transition and Suppression of Orbital Fluctuations in Orthorhombic* $3d^1$ *Perovskites*, Phys. Rev. Lett. **92**, 176403 (2004).

[411] V. I. Anisimov, D. E. Kondakov, A. V. Kozhevnikov, I. A. Nekrasov, Z. V. Pchelkina, J. W. Allen, S.-K. Mo, H.-D. Kim, P. Metcalf, S. Suga, A. Sekiyama, G. Keller, I. Leonov, X. Ren and D. Vollhardt, *Full orbital calculation scheme for materials with strongly correlated electrons*, Phys. Rev. B **71**, 125119 (2005).

[412] I. A. Nekrasov, K. Held, G. Keller, D. E. Kondakov, T. Pruschke, M. Kollar, O. K. Andersen, V. I. Anisimov and D. Vollhardt, *Momentum-resolved spectral functions of* $SrVO_3$ *calculated by LDA+DMFT*, Phys. Rev. B **73**, 155112 (2006).

[413] K. Haule, V. Oudovenko, S. Y. Savrasov and G. Kotliar, *The* $\alpha \rightarrow \gamma$ *Transition in Ce: A Theoretical View from Optical Spectroscopy*, Phys. Rev. Lett. **94**, 036401 (2005).

[414] P. Wissgott, J. Kuneš, A. Toschi and K. Held, *Dipole matrix element approach versus Peierls approximation for optical conductivity*, Phys. Rev. B **85**, 205133 (2012).

[415] V. S. Oudovenko, G. Pálsson, K. Haule, G. Kotliar and S. Y. Savrasov, *Electronic structure calculations of strongly correlated electron systems by the dynamical mean-field method*, Phys. Rev. B **73**, 035120 (2006).

[416] M. Zingl, J. Mravlje, M. Aichhorn, O. Parcollet and A. Georges, *Hall coefficient signals orbital differentiation in the Hund's metal Sr_2RuO_4*, npj Quantum Materials **4**, 35 (2019).

[417] R. Arita, K. Kuroki, K. Held, A. V. Lukoyanov, S. Skornyakov and V. I. Anisimov, *Origin of large thermopower in $LiRh_2O_4$: Calculation of the Seebeck coefficient by the combination of local density approximation and dynamical mean-field theory*, Phys. Rev. B **78**, 115121 (2008).

[418] P. Wissgott, A. Toschi, H. Usui, K. Kuroki and K. Held, *Enhancement of the Na_xCoO_2 thermopower due to electronic correlations*, Phys. Rev. B **82**, 201106 (2010).

[419] J. M. Tomczak, K. Haule and G. Kotliar, *Signatures of electronic correlations in iron silicide*, Proc. Natl. Acad. Sci. U.S.A. **109**, 3243 (2012).

[420] G. Blesio, S. Beck, O. Gingras, A. Georges and J. Mravlje, *Signatures of Hund metal and finite-frequency nesting in Sr_2RuO_4 revealed by electronic Raman scattering*, Phys. Rev. Res. **6**, 023124 (2024).

[421] J. Kuneš, *Efficient treatment of two-particle vertices in dynamical mean-field theory*, Phys. Rev. B **83**, 085102 (2011).

[422] L. Boehnke, H. Hafermann, M. Ferrero, F. Lechermann and O. Parcollet, *Orthogonal polynomial representation of imaginary-time Green's functions*, Phys. Rev. B **84**, 075145 (2011).

[423] H. Park, K. Haule and G. Kotliar, *Magnetic Excitation Spectra in $BaFe_2As_2$: A Two-Particle Approach within a Combination of the Density Functional Theory and the Dynamical Mean-Field Theory Method*, Phys. Rev. Lett. **107**, 137007 (2011).

[424] M. W. Haverkort, M. Zwierzycki and O. K. Andersen, *Multiplet ligand-field theory using Wannier orbitals*, Phys. Rev. B **85**, 165113 (2012).

[425] J. Lüder, J. Schött, B. Brena, M. W. Haverkort, P. Thunström, O. Eriksson, B. Sanyal, I. Di Marco and Y. O. Kvashnin, *Theory of L-edge spectroscopy of strongly correlated systems*, Phys. Rev. B **96**, 245131 (2017).

[426] A. Hariki, T. Uozumi and J. Kuneš, *LDA+DMFT approach to core-level spectroscopy: Application to 3d transition metal compounds*, Phys. Rev. B **96**, 045111 (2017).

[427] A. Hariki, M. Winder and J. Kuneš, *Continuum Charge Excitations in High-Valence Transition-Metal Oxides Revealed by Resonant Inelastic X-Ray Scattering*, Phys. Rev. Lett. **121**, 126403 (2018).

[428] I. Leonov, V. I. Anisimov and D. Vollhardt, *First-Principles Calculation of Atomic Forces and Structural Distortions in Strongly Correlated Materials*, Phys. Rev. Lett. **112**, 146401 (2014).

[429] K. Haule and G. L. Pascut, *Forces for structural optimizations in correlated materials within a DFT+embedded DMFT functional approach*, Phys. Rev. B **94**, 195146 (2016).

[430] E. Plekhanov, N. Bonini and C. Weber, *Calculating dynamical mean-field theory forces in ab initio ultrasoft pseudopotential formalism*, Phys. Rev. B **104**, 235131 (2021).

[431] C. P. Koçer, K. Haule, G. L. Pascut and B. Monserrat, *Efficient lattice dynamics calculations for correlated materials with* DFT + DMFT, Phys. Rev. B **102**, 245104 (2020).

[432] M. Karolak, G. Ulm, T. Wehling, V. Mazurenko, A. Poteryaev and A. Lichtenstein, *Double counting in LDA+DMFT—The example of NiO*, Journal of Electron Spectroscopy and Related Phenomena **181**, 11 (2010), proceedings of International Workshop on Strong Correlations and Angle-Resolved Photoemission Spectroscopy 2009.

[433] A. Georges, G. Kotliar, W. Krauth and M. J. Rozenberg, *Dynamical mean-field theory of strongly correlated fermion systems and the limit of infinite dimensions*, Rev. Mod. Phys. **68**, 13 (1996).

[434] V. I. Anisimov, F. Aryasetiawan and A. I. Lichtenstein, *First-principles calculations of the electronic structure and spectra of strongly correlated systems: the LDA+U method*, J. Phys. Condens. Matter **9**, 767 (1997).

[435] W. Metzner and D. Vollhardt, *Correlated Lattice Fermions in* $d = \infty$ *Dimensions*, Phys. Rev. Lett. **62**, 324 (1989).

[436] A. Georges and G. Kotliar, *Hubbard model in infinite dimensions*, Phys. Rev. B **45**, 6479 (1992).

[437] J. Karp, A. Hampel and A. J. Millis, *Dependence of* DFT + DMFT *results on the construction of the correlated orbitals*, Phys. Rev. B **103**, 195101 (2021).

[438] S. Beck, A. Hampel, O. Parcollet, C. Ederer and A. Georges, *Charge self-consistent electronic structure calculations with dynamical mean-field theory using Quantum ESPRESSO, Wannier 90 and TRIQS*, J. Phys.: Condens. Matter **34**, 235601 (2022).

[439] G. Rohringer, H. Hafermann, A. Toschi, A. A. Katanin, A. E. Antipov, M. I. Katsnelson, A. I. Lichtenstein, A. N. Rubtsov and K. Held, *Diagrammatic routes to nonlocal correlations beyond dynamical mean field theory*, Rev. Mod. Phys. **90**, 025003 (2018).

[440] H. Aoki, N. Tsuji, M. Eckstein, M. Kollar, T. Oka and P. Werner, *Nonequilibrium dynamical mean-field theory and its applications*, Rev. Mod. Phys. **86**, 779 (2014).

[441] S. Biermann, *Dynamical screening effects in correlated electron materials—a progress report on combined many-body perturbation and dynamical mean field theory: "GW + DMFT"*, J. Phys.: Condens. Matter **26**, 173202 (2014).

[442] E. Plekhanov, P. Hasnip, V. Sacksteder, M. Probert, S. J. Clark, K. Refson and C. Weber, *Many-body renormalization of forces in f-electron materials*, Phys. Rev. B **98**, 075129 (2018).

[443] A. H. Romero, D. C. Allan, B. Amadon, G. Antonius, T. Applencourt, L. Baguet, J. Bieder, F. Bottin, J. Bouchet, E. Bousquet, F. Bruneval, G. Brunin, D. Caliste, M. Côté, J. Denier, C. Dreyer, P. Ghosez, M. Giantomassi, Y. Gillet, O. Gingras, D. R. Hamann, G. Hautier, F. Jollet, G. Jomard, A. Martin, H. P. C. Miranda, F. Naccarato, G. Petretto, N. A. Pike, V. Planes, S. Prokhorenko, T. Rangel, F. Ricci, G.-M. Rignanese, M. Royo, M. Stengel, M. Torrent, M. J. van Setten, B. Van Troeye, M. J. Verstraete, J. Wiktor, J. W. Zwanziger and X. Gonze, *ABINIT: Overview and focus on selected capabilities*, The Journal of Chemical Physics **152**, 124102 (2020).

[444] A. Grechnev, I. Di Marco, M. I. Katsnelson, A. I. Lichtenstein, J. Wills and O. Eriksson, *Theory of bulk and surface quasiparticle spectra for Fe, Co, and Ni*, Phys. Rev. B **76**, 035107 (2007).

[445] I. Di Marco, J. Minár, S. Chadov, M. I. Katsnelson, H. Ebert and A. I. Lichtenstein, *Correlation effects in the total energy, the bulk modulus, and the lattice constant of a transition metal: Combined local-density approximation and dynamical mean-field theory applied to Ni and Mn*, Phys. Rev. B **79**, 115111 (2009).

[446] P. Thunström, I. Di Marco, A. Grechnev, S. Lebègue, M. I. Katsnelson, A. Svane and O. Eriksson, *Multiplet effects in the electronic structure of intermediate-valence compounds*, Phys. Rev. B **79**, 165104 (2009).

[447] AMULET, *The AMULET code*, `http://amulet-code.org` (2023), accessed on 2023-12-17.

[448] K. Haule, C.-H. Yee and K. Kim, *Dynamical mean-field theory within the full-potential methods: Electronic structure of $CeIrIn_5$, $CeCoIn_5$, and $CeRhIn_5$*, Phys. Rev. B **81**, 195107 (2010).

[449] S. Choi, P. Semon, B. Kang, A. Kutepov and G. Kotliar, *ComDMFT: A massively parallel computer package for the electronic structure of correlated-electron systems*, Comput. Phys. Commun. **244**, 277 (2019).

[450] M. Wallerberger, A. Hausoel, P. Gunacker, A. Kowalski, N. Parragh, F. Goth, K. Held and G. Sangiovanni, *w2dynamics: Local one- and two-particle quantities from dynamical mean field theory*, Comput. Phys. Commun. **235**, 388 (2019).

[451] H. Shinaoka, J. Otsuki, M. Kawamura, N. Takemori and K. Yoshimi, *DCore: Integrated DMFT software for correlated electrons*, SciPost Phys. **10**, 117 (2021).

[452] A. Amaricci, L. Crippa, A. Scazzola, F. Petocchi, G. Mazza, L. de Medici and M. Capone, *EDIpack: A parallel exact diagonalization package for quantum impurity problems*, Comput. Phys. Commun. **273**, 108261 (2022).

[453] V. Singh, U. Herath, B. Wah, X. Liao, A. H. Romero and H. Park, *DMFTwDFT: An open-source code combining Dynamical Mean Field Theory with various density functional theory packages*, Comput. Phys. Commun. **261**, 107778 (2021).

[454] O. Parcollet, M. Ferrero, T. Ayral, H. Hafermann, I. Krivenko, L. Messio and P. Seth, *TRIQS: A toolbox for research on interacting quantum systems*, Comput. Phys. Commun. **196**, 398 (2015).

[455] M. Aichhorn, L. Pourovskii, P. Seth, V. Vildosola, M. Zingl, O. Peil, X. Deng, J. Mravlje, G. Kraberger, C. Martins, M. Ferrero and O. Parcollet, *TRIQS/DFTTools: A TRIQS application for ab initio calculations of correlated materials*, Comput. Phys. Commun. **204**, 200 (2016).

[456] M. E. Merkel, A. Carta, S. Beck and A. Hampel, *solid_dmft: gray-boxing DFT+ DMFT materials simulations with TRIQS*, J. Open Source Software **7**, 4623 (2022).

[457] M. Schüler, O. E. Peil, G. J. Kraberger, R. Pordzik, M. Marsman, G. Kresse, T. O. Wehling and M. Aichhorn, *Charge self-consistent many-body corrections using optimized projected localized orbitals*, J. Phys. Condens. Matter **30**, 475901 (2018).

[458] A. D. N. James, E. I. Harris-Lee, A. Hampel, M. Aichhorn and S. B. Dugdale, *Wave functions, electronic localization, and bonding properties for correlated materials beyond the Kohn-Sham formalism*, Phys. Rev. B **103**, 035106 (2021).

[459] B. Amadon, T. Applencourt and F. Bruneval, *Screened Coulomb interaction calculations: cRPA implementation and applications to dynamical screening and self-consistency in uranium dioxide and cerium*, Phys. Rev. B **89**, 125110 (2014).

[460] C. Friedrich, S. Blügel and A. Schindlmayr, *Efficient implementation of the GW approximation within the all-electron FLAPW method*, Phys. Rev. B **81**, 125102 (2010).

[461] K. Kurita, T. Misawa, K. Yoshimi, K. Ido and T. Koretsune, *Interface tool from Wannier90 to RESPACK: wan2respack*, Computer Physics Communications **292**, 108854 (2023).

[462] M. Rösner, E. Şaşıoğlu, C. Friedrich, S. Blügel and T. O. Wehling, *Wannier function approach to realistic Coulomb interactions in layered materials and heterostructures*, Phys. Rev. B **92**, 085102 (2015).

[463] P. Werner and M. Casula, *Dynamical screening in correlated electron systems—from lattice models to realistic materials*, Journal of Physics: Condensed Matter **28**, 383001 (2016).

[464] J. E. Gubernatis, M. Jarrell, R. N. Silver and D. S. Sivia, *Quantum Monte Carlo simulations and maximum entropy: Dynamics from imaginary-time data*, Phys. Rev. B **44**, 6011 (1991).

[465] X. Wang, E. Gull, L. de' Medici, M. Capone and A. J. Millis, *Antiferromagnetism and the gap of a Mott insulator: Results from analytic continuation of the self-energy*, Phys. Rev. B **80**, 045101 (2009).

[466] R. Kubo, *Statistical-Mechanical Theory of Irreversible Processes. I. General Theory and Simple Applications to Magnetic and Conduction Problems*, J. Phys. Soc. Jpn. **12**, 570 (1957).

[467] M. Pickem, E. Maggio and J. M. Tomczak, *LinReTraCe: The linear response transport centre*, SciPost Phys. Codebases p. 16 (2023).

[468] M. W. Haverkort, *Quanty for core level spectroscopy - excitons, resonances and band excitations in time and frequency domain*, Journal of Physics: Conference Series **712**, 012001 (2016).

[469] Y. Wang, G. Fabbris, M. Dean and G. Kotliar, *EDRIXS: An open source toolkit for simulating spectra of resonant inelastic x-ray scattering*, Comput. Phys. Commun. **243**, 151 (2019).

[470] V. I. Anisimov and A. V. Kozhevnikov, *Transition state method and Wannier functions*, Phys. Rev. B **72**, 075125 (2005).

[471] V. I. Anisimov, A. V. Kozhevnikov, M. A. Korotin, A. V. Lukoyanov and D. A. Khafizullin, *Orbital density functional as a means to restore the discontinuities in the total-energy derivative and the exchange-correlation potential*, J. Phys.: Condens. Matter **19**, 106206 (2007).

[472] E. Kraisler and L. Kronik, *Piecewise Linearity of Approximate Density Functionals Revisited: Implications for Frontier Orbital Energies*, Phys. Rev. Lett. **110**, 126403 (2013).

[473] J. H. Skone, M. Govoni and G. Galli, *Self-consistent hybrid functional for condensed systems*, Phys. Rev. B **89**, 195112 (2014).

[474] C. Li, X. Zheng, A. J. Cohen, P. Mori-Sánchez and W. Yang, *Local Scaling Correction for Reducing Delocalization Error in Density Functional Approximations*, Phys. Rev. Lett. **114**, 053001 (2015).

[475] C. Li, X. Zheng, N. Q. Su and W. Yang, *Localized orbital scaling correction for systematic elimination of delocalization error in density functional approximations*, Natl. Sci. Rev. **5**, 203 (2017).

[476] D. Wing, G. Ohad, J. B. Haber, M. R. Filip, S. E. Gant, J. B. Neaton and L. Kronik, *Band gaps of crystalline solids from Wannier-localization-based optimal tuning of a screened range-separated hybrid functional*, Proc. Natl. Acad. Sci. U.S.A. **118**, e2104556118 (2021).

[477] J. Ma and L.-W. Wang, *Using Wannier functions to improve solid band gap predictions in density functional theory*, Sci. Rep. **6**, 24924 (2016).

[478] G. Pizzi, A. Cepellotti, R. Sabatini, N. Marzari and B. Kozinsky, *AiiDA: automated interactive infrastructure and database for computational science*, Comput. Mater. Sci. **111**, 218 (2016).

[479] S. P. Huber, S. Zoupanos, M. Uhrin, L. Talirz, L. Kahle, R. Häuselmann, D. Gresch, T. Müller, A. V. Yakutovich, C. W. Andersen, F. F. Ramirez, C. S. Adorf, F. Gargiulo, S. Kumbhar, E. Passaro, C. Johnston, A. Merkys, A. Cep ellotti, N. Mounet, N. Marzari, B. Kozinsky and G. Pizzi, *AiiDA 1.0, a scalable computational infrastructure for automated reproducible workflows and data provenance*, Sci. Data **7**, 300 (2020).

[480] M. Uhrin, S. P. Huber, J. Yu, N. Marzari and G. Pizzi, *Workflows in AiiDA: Engineering a high-throughput, event-based engine for robust and modular computational workflows*, Comput. Mater. Sci. **187**, 110086 (2021).

[481] J. D. Hunter, *Matplotlib: A 2D graphics environment*, Comput. Sci. Eng. **9**, 90 (2007).

[482] J. Qiao, G. Pizzi and N. Marzari, *WannierIO.jl: A Julia package for reading/writing wannier90 file formats*, `https://github.com/qiaojunfeng/WannierIO.jl` (2023), accessed on 2023-12-11.

[483] M. F. Herbst, A. Levitt and E. Cancès, *DFTK: The Density-functional toolkit* (2023), `https://dftk.org`.

[484] M. Bonacci, J. Qiao, N. Spallanzani, A. Marrazzo, G. Pizzi, E. Molinari, D. Varsano, A. Ferretti and D. Prezzi, *Towards high-throughput many-body perturbation theory: efficient algorithms and automated workflows*, npj Comput. Mater. **9**, 74 (2023).

[485] S. P. Ong, W. D. Richards, A. Jain, G. Hautier, M. Kocher, S. Cholia, D. Gunter, V. L. Chevrier, K. A. Persson and G. Ceder, *Python Materials Genomics (pymatgen): A robust, open-source python library for materials analysis*, Comput. Mater. Sci. **68**, 314 (2013).

[486] A. Jain, S. P. Ong, W. Chen, B. Medasani, X. Qu, M. Kocher, M. Brafman, G. Petretto, G.-M. Rignanese, G. Hautier, D. Gunter and K. A. Persson, *FireWorks: a dynamic workflow system designed for high-throughput applications*, Concurrency Computat.: Pract. Exper. **27**, 5037 (2015).

[487] A. R. Supka, T. E. Lyons, L. Liyanage, P. D'Amico, R. Al Rahal Al Orabi, S. Mahatara, P. Gopal, C. Toher, D. Ceresoli, A. Calzolari, S. Curtarolo, M. Buongiorno Nardelli and M. Fornari, *AFLOWπ: A minimalist approach to high-throughput ab initio calculations including the generation of tight-binding hamiltonians*, Comput. Mater. Sci. **136**, 76 (2017).

[488] D. Schwalbe-Koda, *mkite: A distributed computing platform for high-throughput materials simulations*, Computational Materials Science **230**, 112439 (2023).

[489] M. Gjerding, T. Skovhus, A. Rasmussen, F. Bertoldo, A. H. Larsen, J. J. Mortensen and K. S. Thygesen, *Atomic Simulation Recipes: A Python framework and library for automated workflows*, Comput. Mater. Sci. **199**, 110731 (2021).

[490] A. Sakai, S. Minami, T. Koretsune, T. Chen, T. Higo, Y. Wang, T. Nomoto, M. Hirayama, S. Miwa, D. Nishio-Hamane, F. Ishii, R. Arita and S. Nakatsuji, *Iron-based binary ferromagnets for transverse thermoelectric conversion*, Nature **581**, 53 (2020).

[491] K. F. Garrity and K. Choudhary, *Database of Wannier tight-binding Hamiltonians using high-throughput density functional theory*, Sci. Data **8**, 106 (2021).

[492] L. Talirz, S. Kumbhar, E. Passaro, A. V. Yakutovich, V. Granata, F. Gargiulo, M. Borelli, M. Uhrin, S. e. P. Huber, S. Zoupanos, C. S. Adorf, C. W. Andersen, O. Schütt, C. A. Pignedoli, D. Passerone, J. VandeVondele, T. C. . Schulthess, B. Smit, G. Pizzi and N. Marzari, *Materials Cloud, a platform for open computational science*, Sci. Data **7**, 299 (2020).

[493] M. J. T. Oliveira, N. Papior, Y. Pouillon, V. Blum, E. Artacho, D. Caliste, F. Corsetti, S. de Gironcoli, A. M. Elena, A. García, V. M. García-Suárez, L. Genovese, W. P. Huhn, G. Huhs, S. Kokott, E. Küçükbenli, A. H. Larsen, A. Lazzaro, I. V. Lebedeva, Y. Li, D. López-Durán, P. López-Tarifa, M. Lüders, M. A. L. Marques, J. Minar, S. Mohr, A. A. Mostofi, A. O'Cais, M. C. Payne, T. Ruh, D. G. A. Smith, J. M. Soler, D. A. Strubbe, N. Tancogne-Dejean, D. Tildesley, M. Torrent and V. W.-z. Yu, *The CECAM electronic structure library and the modular software development paradigm*, J. Chem. Phys. **153**, 024117 (2020).

[494] T. Nomoto, T. Koretsune and R. Arita, *Local force method for the ab initio tight-binding model: Effect of spin-dependent hopping on exchange interactions*, Phys. Rev. B **102**, 014444 (2020).

[495] H. Yoon, T. J. Kim, J.-H. Sim and M. J. Han, *Jx: An open-source software for calculating magnetic interactions based on magnetic force theory*, Computer Physics Communications **247**, 106927 (2020).

[496] X. He, N. Helbig, M. J. Verstraete and E. Bousquet, *TB2J: A python package for computing magnetic interaction parameters*, Computer Physics Communications **264**, 107938 (2021).

[497] L. Ponet (2023), the DFWannier.jl code package is available at `https://github.com/louisponet/DFWannier.jl`.